**UNIVERSITY OF CALIFORNIA,
IRVINE**

Modeling, Design, and Analysis of Monolithic Charged-particle Image Sensors

DISSERTATION

submitted in partial satisfaction of the requirements
for the degree of

Doctor of Philosophy

in Electrical and Computer Engineering

by

Shengdong Li

Dissertation Committee:
Professor Stuart Kleinfelder, Chair
Professor Guann-Pyng G.P. Li
Professor Nguyen H. Xuong

2007

The dissertation of Shengdong Li

is approved and is acceptable in quality and form for

publication on microfilm and in digital formats:

Committee Chair

University of California, Irvine

2007

DEDICATION

To my family

TABLE OF CONTENTS

LIST OF FIGURES

LIST OF TABLES

ACKNOWLEDGEMENTS

I would like to thank my advisor Professor Stuart Kleinfelder for his financial support, technical insight, and tremendous patience in guiding through the course of this thesis research. I thank my committee members, Professors Stuart Kleinfelder, Nguyen H. Xuong, and Guann-Pyng G.P. Li for their time and effort in reviewing my dissertation and their valuable suggestions and comments. I thank Dr. Howard Matis for his time and patience in helping me understand ionization generation and measurement.

I thank my colleagues for their many contributions including Yandong Chen, Fred Duttweiler, Liang Jin, Vipul Kumar, Philippe Leblanc, Anna-Clare Milazzo. Yandong Chen designed EM2 and Vipul Kumar designed the testing board for EM5. Liang Jin helped me understand many important issues in electron microscopy testing and he also patiently showed me how to operate transmission electron microscope. Images of biological samples presented in this dissertation were all taken by my colleagues at UCSD. I also would like to thank researchers at Lawrence Berkeley National Laboratory: Dr. Howard Matis, Dr. Howard Wieman, Fred Bieser, and Jake King. Dr. Howard Matis and Jake King measured the X-ray data presented in my dissertation. Dr. Howard Matis measured the epitaxial layer thickness.

I would like to thank my friends and supporters including: Lin Hua, Mona Ahooie, Lifeng Zheng, Yang Zhang, Lin Wang, and Professor Zhihong Lin. Lin Wang helped me

make the Fortran code work in my computer. Professor Zhihong Lin from the Physics Department at UCI helped me understand the theory of the Monte Carlo modeling.

I thank my family and Sunan Liu for their unconditional support, especially during many difficult and stressful times.

CURRICULUM VITAE

Shengdong Li

EDUCATION

- Ph.D., Electrical and Computer Engineering, University of California at Irvine, September 2007.
  Dissertation: Modeling, Design, and Analysis of Monolithic Charged-particle Image Sensors.

- M.S., Electrical Engineering and Computer Science, University of California at Irvine, June 2004.
  Thesis: High Frequency Carbon Nanotube Devices

- B.S., Materials Science & Engineering, University of Science and Technology of China, July, 2001.

RESEARCH EXPERIENCE

- Numerical modeling by Monte Carlo and finite difference methods.
- Charged-particle detection and imaging in high energy physics and electron microscopy.
- CMOS integrated circuit design and testing.
- High frequency nano-electronics and bio-nanotechnology
- Semiconductor fabrication.

SELECTED PEER-REVIEWED JOURNAL PUBLICATIONS

1. **Shengdong Li**, S. Kleinfelder, "Modeling, Design, and Analysis of Monolithic Charged-particle Image Sensors", in preparation.
2. **Shengdong Li**, S. Kleinfelder, "Charged Particle Imaging Sensors", Nuclear Instruments and Methods A, in press.
3. Stuart Kleinfelder, **Shengdong Li**, Yandong Chen, Optimization of Monolithic Charged-Particle Sensor Arrays, Nuclear Instruments and Methods A, in press.
4. P. J. Burke, **Shengdong Li**, and Z. Yu, "Quantitative Theory of Nanowire and Nanotube Antenna Performance," IEEE Transactions on Nanotechnology, vol. 5, 314-334, 2006.

5. **Shengdong Li**, Z. Yu, S. Yeng, W.C. Tang, P. J. Burke, "Carbon Nanotube Transistor Operation at 2.6 GHz", Nano Letters, 4(4), 753-756, 2004.
6. **Shengdong Li**, Z. Yu, P. J. Burke, "Silicon Nitride Gate Dielectric for Top-Gated Carbon Nanotube Field Effect Transistors", Journal of Vacuum Science and Technology B: Microelectronics and Nanometer Structures, 22(6), 3112-3114, 2004.
7. **Shengdong Li**, Z. Yu, C. Rutherglen, P. J. Burke, "Electrical Properties of 0.4 cm Long Single-walled Carbon Nanotubes", Nano Letters, 4(10), 2003-2007, 2004.
8. Zhen Yu, **Shengdong Li**, Peter J. Burke, "Synthesis of Aligned Arrays of Millimeter Long, Straight Single-Walled Carbon Nanotubes", Chemistry of Materials, 16(18), 3414-3416, 2004.
9. Lifeng Zheng, **Shengdong Li**, J. P. Brody, P. J. Burke, "Manipulating Nanoparticles in Solution With Electrically Contacted Nanotubes Using Dielectrophoresis", Langmuir, 20(20), 8612-8619, 2004.

TEACHING EXPERIENCE

- EECS 275A, EECS 275B, EECS 170B (integrated circuit design, verification, and testing).

SELECTED AWARDS AND RECOGNITIONS

- National Science Foundation Summer Fellowship, 2007
- Tech Coast Angels Seed Financing Invitational Award in UCI Stradling Yocca Carlson & Rauth Business Plan Competition, 2006.
- 2005 Chinese Government Award for Outstanding Students Abroad, presented by the Ministry of Education, China.
- 1st place prize of IEEE Student Innovation Contest, presented during the 3rd International System-on-Chip (SoC) Conference, 2005.
- CESASC Scholarship, Chinese-American Engineers and Scientists Association of Southern California, 2005.
- Dr. Denny Ko Future Entrepreneur Scholarship, 2005.
- EECS Best Paper Award, UC Irvine, 2005.

PROFESSIONAL MEMBERSHIP

- Institute of Electrical & Electronic Engineers (IEEE), since 2003.

ABSTRACT OF THE DISSERTATION

Modeling, Design, and Analysis of Monolithic Charged-particle Image Sensors

By

Shengdong Li

Doctor of Philosophy in Electrical and Computer Engineering

University of California, Irvine, 2007

Professor Stuart Kleinfelder, Chair

Active pixel sensors for charged-particle imaging applications such as electron microscopy and high energy radiation have been developed. Systematic optimization of this technology has been developed via Monte Carlo simulation and experimental device design. The Monte Carlo model is constructed following Einstein's formulism of Brownian motion and is implemented in C++ and Matlab. Ionization generation due to X-ray photons and high energy electrons are modeled as exponential random numbers and Bichsel random numbers, respectively. Several experimental devices and full-scale prototypes are presented, including a pixel pitch test chip, a diode area test chip, a 550 by 512 pixel analog read-out chip, a 1k by 1k pixel analog read-out chip, and a 560 by 460 pixel digital read-out chip with per-column analog-to-digital conversion and noise cancellation.

Diffusion is the dominating charge transport mechanism and ionization electrons collected distribute in a collection matrix/profile consisting of an array of pixels centered

on the struck pixel. First, the substrate contribution is found to be equivalent to ~ 3.7 μm epitaxial silicon for 5 μm pitch pixel array built on 8 μm epitaxial silicon. Second, both simulation and measurement show that the spatial resolution characterized by sigma and FWHM scales linearly with the pixel pitch. Third, an 8 μm epitaxial silicon allows 2.5 times improvement in signal strength than where pixels are directly built on bulk substrate. Thicker epitaxial silicon leads to increased signal strength and signal-to-noise ratio, however, the collection profile becomes broader due to increased lateral diffusion of electrons generated in the thicker silicon. Fourth, the dependence of signal-to-noise on diode area is evaluated. The diode area that maximizes signal-to-noise ratio is found to be ~ $1\mu m^2$ for 5μm pitch pixels. Fifth, the simulation shows that a lower electron acceleration voltage (> 200 keV) leads to larger signal-to-noise ratio but the lateral spreading on electron energy is negligible. Finally, high resolution images of biological samples such as neuron's myelin sheath, catalase protein crystal, and mouse cardiac cells, taken with the prototype sensors, are presented and a nine-fold improvement in spatial resolution as compared to charge coupled device has been measured.

CHAPTER 1: INTRODUCTION

1.1 Motivation

Recent advances in structural biology has been urgently demanding an imaging technology that can circumvent the difficulties experienced by conventional methods such as X-ray crystallography and Nuclear Magnetic Resonance (NMR) in determining the three-dimensional (3D) structure of proteins and viruses at atomic scale efficiently [1-3]. For X-ray crstallography, structural information is retrieved from analyzing the scattering pattern of X-ray photons through a specimen in crystal form. The first solved protein crystal structure was of Sperm Whale myoglobin, as determined by Max Perutz and John Cowdery Kendrew in 1958, for which they were awarded the Nobel Prize in 1962. Althoug currently the dominating method for protein structural analysis, X-ray crystallography, as its name suggests, requires the object under study to be crystallized. Unfortunately, obtaining protein crystal is usually a difficult and often times impossible task and the applicability of this technology is thus severely limited. For NMR, structural information can be retrieved by analyzing the response of magnetic nuclei to a combination of a very powerful aligning magnetic field and a perturbing electromagnetic field. The use of NMR spectroscopy for protein structural analysis was awarded the Nobel Prize in 2002. NMR method does not mandate protein crystal, however, it is currently limited to relatively small proteins due to rapid relaxation of magnetization for larger structures. To date, Protein Data Bank[4], a freely available protein structural data resource hub reports that X-ray crystallography accounts for ~36000 and NMR spectroscopy has contributed almost 6000 in a total of ~42000 protein structures that

have been solved. Since 2005, ~ 4000 protein structures have been solved by X-ray crystallography and ~700 by NMR annually. The structures solved so far mainly lies in the low complexity end or because the crystallization is less demanding. Continued progress in this field will have to face those more challenging protein structures that are large and difficult or even impossible to be crystallized such as membrane-bound proteins [5]. The development of innovative methodologies and technologies that can overcome these difficulties is needed.

Electron microscopy has long been a powerful method in biological imaging as it can provide images from celluar scale to molecular and atomic scale[6, 7]. However, its application to protein structural analysis is limited because the resolution that can be achieved so far is rather low. For a virus, the best structure from electron microscopy is now 4.5 Å[8], and for a large protein complex like the ribosome, the best resolution is 7.4 Å[9]. Protein Data Bank shows merely over 140 protein structures solved by electron microscopy method as of June 2007. The limitation to the resolution of the structures obtained with electron microscopy is the difficulties associated with the collection and processing of very large data sets (estimated to be up to one million images for 3 Å resolution) required for statistical analysis using conventional imaging technologies such as film or Charge-coupled devices (CCDs) [10].

Film uses an electron sensitive chemical emulsion to directly record incident electrons transmitted through the samples under test. While film provides excellent modulation transfer functions (MTF) compared to commercial CCD cameras, it requires several post-

acquisition steps such as development and digitization that are cumbersome, time-consuming, resolution degrading, and impossible to make real-time adjustment and retake images if needed. Moreover, film lacks the linear response afforded by CCD camera systems. The scale of the needed data sets severely compromises the practicality of using film to record electron images.

As an alternative to analog film camera, CCDs have been commonly used in electron microscopy for direct digital readout. However, CCDs can not be directly exposed to high energy electrons due to radiation vulnerability and a phosphorescent scintillation screen is needed to convert the electron image to a photonic image within a spectral range where the detector quantum efficiency is maximized. Unfortunately, with each electron event, the footprint created by electrons within the scintillation screen is usually greater than the pixel pitch of CCD. For example, the full width at half maximum (FWHM) of the footprint of 300 keV electrons is around 30 μm, and the full width at 1% is ~ 200 μm. Such electron-photon conversion substantially compromises the spatial resolution. To mitigate this problem, tapered fiber optics and/or demagnification lens optics can be used to de-magnify the scintillator image to match the CCD device thereby restoring the MTF. However, both optical relay scenarios introduce problems of their own. With tapered fiber optics, large spatial distortions and non-uniformities are introduced that are difficult to correct. With demagnification lens-optics, the poor efficiency of the coupling dramatically reduces the number of photons reaching the CCD, which in turn reduces the signal-to-noise ratio of the system.

Clearly an ideal imaging system for electron microscopy should be able to directly detect high energy electrons and provide output in digital form simultaneously. This is where epitaxial silicon active pixel sensor (APS) technology, which has been developed to detect charged-particles in high energy Physics, comes into play [11].

1.2 Epitaxial Silicon Active Pixel Sensor Overview

APS arrays for charged-particle detection are originally developed for optical imaging. Figure 1.1(a) shows the schematic view of an APS pixel built on top of an epitaxial silicon layer, typically a lightly doped in p-type. Figure 1.1 (b) shows the scanning electron microscopy image of the cross-sectional view of an epitaxial silicon active pixel sensor in 0.25 μm CMOS technology where the epitaxial layer is about 8 μm in thickness. In each pixel, there are three transistors for reset, buffering, and multiplexing and an n-diode for charge collection. All three transistors are of NMOS type built in p-well without any unwanted pn junction in the pixel array area and the diode is typically an n-well over the p-type epitaxial layer (p-epi). The source follower transistor converts charge signal into voltage level before passing it to read-line, thus gaining the name "active pixel". By contrast, passive pixels pass charge signal directly the column line and are prone to noise corruption.

Normal APS operation consists of three phase: reset, integration, and read-out. During the reset phase, the n-well/p-epi diode is reversely biased using the reset transistor and a depletion region is formed at the boundaries. The depletion width can be calculated using commercial device simulation package such as ISE-TCAD provided Synopsis Inc. ISE-

TCAD solves Poisson's equation coupled with continuity conditions assuming drift-diffusion model by finite element analysis method [12]. While finite element analysis provides rather accurate results contingent on knowing the process parameters such as doping profile and dopant density precisely, a more straightforward and physically meaningful approach is to use step-junction approximation[13, 14]. Both ISE-TCAD and step-junction approximation give similar results when device dimensions are adequately large. Step-junction approximation is used in the following discussion because it provides straightforward physical insights.

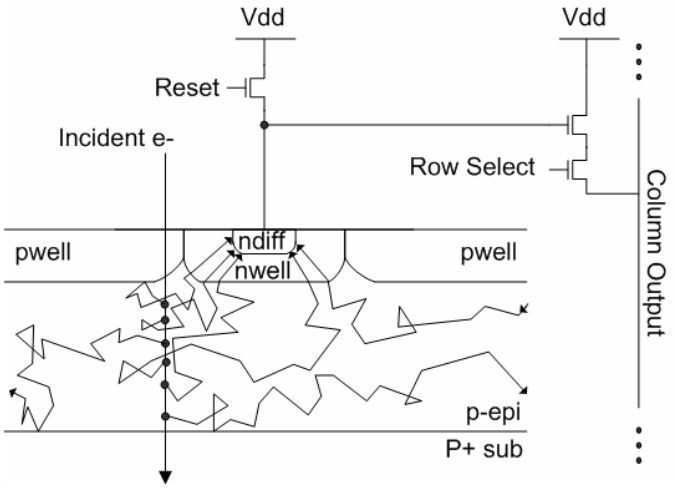

(a)

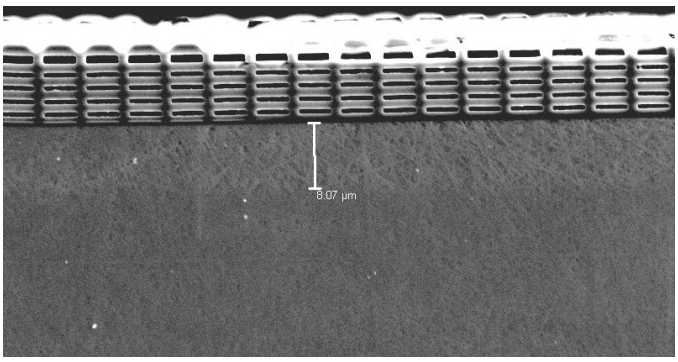

(b)

Figure 1.1: (a) Cross-sectional view of collection diode, and APS readout scheme; (b) Scanning electron microscopy image of the cross-section of an epitaxial silicon APS chip (0.25-µm one ploy and five metal CMOS technology), provided by Dr. Howard Matis.

The depletion width and built-in voltage across a pn junction are given as

$$x_p = \left[\frac{2K_s \cdot \varepsilon_0}{q} \left(\frac{N_D}{N_A(N_A + N_D)} \right) (V_{bi} + V_{reset}) \right]^{1/2} \tag{1.1}$$

$$x_n = \left[\frac{2K_s \cdot \varepsilon_0}{q} \left(\frac{N_A}{N_D(N_A + N_D)} \right) (V_{bi} + V_{reset}) \right]^{1/2} \tag{1.2}$$

and

$$V_{bi} = \frac{kT}{q} \log_e \left(\frac{N_A N_D}{n_i^2} \right) \tag{1.3}$$

where Ks is the relative dielectric constant of silicon, n_i is the density of electrons in intrinsic silicon at room temperature. N_D is the doping density of n-well, N_A is the doping density of p-epi, p-well, and p-substrate. As n-well is much more heavily doped than the p-epi region, x_p is usually much larger than x_n and the depletion region is primarily located in the more lightly doped p-epi region, yielding

$$x_p = \left[\frac{2K_s \cdot \varepsilon_0}{q} \frac{N_D}{N_A} (V_{bi} + V_{reset}) \right]^{1/2} \tag{1.4}$$

and

$$x_n = \left[\frac{2K_s \cdot \varepsilon_0}{q} \left(\frac{N_A}{(N_D)^2} \right) (V_{bi} + V_{reset}) \right]^{1/2} \sim 0 \tag{1.5}$$

Thus the total depletion width is given by

$$W = x_p + x_n \approx x_p = \left[\frac{2K_s \cdot \varepsilon_0}{q} \frac{N_D}{N_A} (V_{bi} + V_{reset}) \right]^{1/2} \tag{1.6}$$

From Equation 1.4 and 1.6, the depletion width is about 2 μm under normal reset condition. Therefore, the epitaxial layer can not be fully depleted and the bulk epitaxial

region is essential free of electric field. This value is consistent with results calculated using more accurate finite element method in ISE-TCAD when the diode is adequately large. When the dimension of the diode becomes very small, the accuracy of the step-junction approximation method decrease and ISE-TCAD yields more accurate results. In order to fully deplete the 8μm epitaxial layer, the required reset voltage can be calculated from the following equation

$$V_{reset} = \frac{2K_s \cdot \varepsilon_0}{q} \frac{N_D}{N_A} x_p^2 \tag{1.7}$$

Assuming x_p = 8 μm, the reset voltage can be worked out as ~50 V. This value is far greater the maximum voltage allowed in a typical CMOS technology. With limited reset voltage, the bulk of the p-epi region is free of electric field and the minority carriers diffuse rather than drift in this region. Similar conclusion can be drawn for more heavily doped p-type bulk substrate (p-sub). Monte Carlo modeling presented in this manuscript will focus on diffusion.

1.3 Overview of Ionization Generation and Charge Transport and Collection Modeling

In optical imaging, the impinging photon beam has high area density but lower energy (300 nm ~ 800 nm). Electron-hole pairs can only be generated in the valence band and conduction band (Eg = 1.12 eV) through photo-electric effect. Because of low energy, no more than one electron-hole pair can be generated per incident photon. By contrast, electron-hole generation for high energy particle is a much more complicated process that depends on the nature of the incident particle. More tightly bonded electrons can be

excited and a large number of electron-hole pairs can be generated by photo-electric ionization, Bremstrahlung, Compton Effect, and pair generation[15], resulting in an average electron-hole excitation energy of ~ 3.6 eV. The particle-silicon interaction is generally a stochastic process that is best characterized by probability distribution functions. For example, 5.9 keV ^{55}Fe X-ray is absorbed by silicon following an exponential distribution [16] and electrons interact with silicon follows the Landau distribution [17]. These differences are visualized in Figure 1.2.

Because the number of ionization electrons generated by incident high energy electrons depends on the thickness of the sensitive region through which they penetrate, a thicker p-epi layer extends the sensitive region. With metal layers transparent to high energy particles such as X-ray and electron beam, the continuous p-epi layer makes possible a 100% effective fill factor[18] and a far larger signal per incident charged particle than a conventional CMOS photodiode built on bulk substrate can provide.

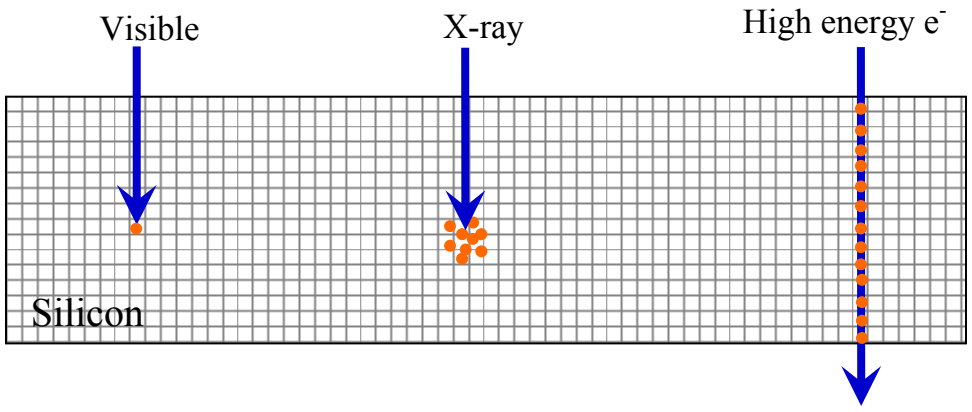

Figure 1.2: Conceptual view of minority carrier generation in silicon for three types of incident particles: visible light photon, xray photon, and high energy electron.

Charge carriers generated by high energy particles create a local in-equilibrium in the silicon and its relaxation has very important implication on sensor performance in terms of spatial resolution and signal-to-noise ratio. It has been the subject of intense research by experiment and simulation in the optical image sensor and charged-particle detector community for a long time. Close form analytical solutions using Fourier series[19-21] method, the image method [22], and Green's function method [23] have been reported to study rather ideal boundary conditions. Numerical methods are typically used to deal with more complex real-life boundary conditions. Numerical methods such as finite element analysis[24, 25] or finite difference analysis[26] have been reported. Another class of numerical methods is based on Monte Carlo method that tracks the movement of individual particles[27-29]. Monte Carlo approach is advantageous in that the ionization generation and diffusion – the dominating transport mechanism are both probabilistic. In addition, Monte Carlo method allows maximum flexibility in dealing with complicated boundary conditions. Third, Monte Carlo approach allows direct comparison with collection matrices measured by experiment. This thesis will develop a complete Monte Carlo that allows us to track the generation, movement, collection, and/or recombination of each ionization electrons.

1.4 Organization of This Thesis

This dissertation is organized in seven chapters.

Chapter 2 presents the construction of a Monte Carlo framework from first principles following Einstein's formulism of Brownian motion. Ionization generation of X-ray

photons and high energy electrons are modeled directly using random numbers following exponential distribution and Bichsel distribution, respectively. Transport equation with recombination term and ionization generation as initial condition is solved analytically by Fourier's transform method, thus establishing the relationship between time step and random-walk step size and recombination rate, key to the Monte Carlo algorithm.

Chapter 3 presents the design of three generations of prototype chips aiming to test the effects of important design parameters in determining the sensor performance such pixel pitch, diode area, and epitaxial silicon thickness. Testing set-up using X-ray photons and high energy electrons is also briefly discussed.

Chapter 4 discusses the simulation and measurement of sensor array in response to ^{55}Fe 5.9 keV X-ray photons. Important contribution from X-ray events generated in the bulk substrate has been identified due to finite substrate recombination rate. Charge carrier diffusion in epitaxial silicon layer and the bulk substrate leads to significant lateral diffusion and recombination loss becomes appreciable when pixel pitch becomes greater than 10 μm. The spatial resolution scales linearly with the pixel pitch despite that diffusion is the dominating transport mechanism.

Chapter 5 discusses the simulation and measurement of sensor array in response to incident electrons with energy ranging from 200 keV to 1000 keV. Similar to the response to X-ray photons, bulk substrate contributes significantly to the signal strength but slightly reduces the spatial resolution. The substrate contribution is quantified by

fitting the simulated histogram of ionization electrons collected with theoretical Bichsel histogram. Other key factors including pixel pitch, diode area, epitaxial silicon thickness, and the energy of incident electrons are systematically studied in sequence. Initial success based on the third generation prototype chip is also presented.

Chapter 6 presents the design and testing of two more advanced prototype chips: a one-mega pixel analog read-out chip and a 560 by 460 digital read-out chip with per-column analog-to-digital conversion. Directly compared to CCD counterpart, the one-mega pixel chip allows at least 9 times improvement in spatial resolution.

Lastly, Chapter 7 concludes the dissertation with a brief discussion on future direction in charged-particle image sensor modeling and design.

CHAPTER 2: MONTE CARLO FRAMEWORK

This chapter serves as the foundation for the Monte Carlo model developed in this thesis research. First, the history, definition, and application of Monte Carlo method are briefly presented, focusing on the applicability of Monte Carlo method in dealing with processes that are directly or indirectly stochastic. This method is then discussed in detail in the context of understanding diffusion and Brownian motion. Key concepts in statistics such as the Law of Large Numbers, Central Limit Theorem, confidence interval is overviewed in a way pertinent to the Monte Carlo framework. Next, essential components of the Monte Carlo framework: the generation of random numbers, boundary condition, initial condition is studied in detail. After that, a Monte Carlo alogrith and flow chart is presented.

2.1 Monte Carlo Method Overview

The first known application of Monte Carlo method is likely that of Buffon's Needles, a simple geometrical probability problem published in 1777. Suppose needles are thrown randomly onto a plane marked with parallel lines of uniform distance equal to the length of the needles, the probability of finding needles crossing a line is equal to $2/\pi$. Throwing needles for many times gives rise to a very good estimation of π. Essentially, Monte Carlo method is a random sampling technique by which the behavior of a complex system as a whole can be deduced from the study of comparatively few. Monte Carlo method typically features a repetition algorithm with a large number of random numbers, as exemplified by Buffon's Needle problem. The name -- Monte Carlo – is derived from

a Monaco city with many casinos and gambling. Monte Carlo method has been extensively applied to directly simulate stochastic processes and to quantify complex systems that are difficult or even impossible to solve using deterministic methods[30-32]. Many great minds in human history such as Enrico Fermi and John von Neumann practiced this method. Fermi used Monte Carlo method to calculate the properties of the newly-discovered neutron and it was central to the simulation needed by the Manhattan Project. The application of Monte Carlo method to charged particles was first reported by Hebbard and Wilson in 1955[33]. Monte Carlo method has been used in everything from electronics to traffic control to nuclear physics and finance. The following few paragraphs will discuss the nuts and bolts of Monte Carlo method in the context of studying diffusion and Brownian motion.

2.2 Monte Carlo Treatment of Brownian Motion and Diffusion

2.2.1 Brownian Motion and Diffusion

Brownian motion, a term coined in honor of an English botanist Robert Brown who noticed that pollen particles suspended in water jiggled randomly under the lens of a microscope in 1827. It was Einstein who first discovered in 1906 that Brownian motion is essentially the microscopic representation of diffusion. The diffusion equation expressed in terms of volumetric concentration is given as

$$\frac{\partial n}{\partial t} = D_n \frac{d^2 n}{dx^2} \tag{2.1}$$

where D_n is the diffusion coefficient and n is volumetric concentration. In Einstein's formulism, an equivalent equation from the microscopic perspective can be obtained by

replacing the volumetric concentration with the probability density function P with respect to the position of the particle. That is

$$\frac{\partial P}{\partial t} = D_n \frac{d^2 P}{dx^2} \tag{2.2}$$

Equation 2.1 and 2.2 are the same as long as the total number of particles remains constant. In the following discussion, P and n will be not be differentiated unless otherwise noted explicitly.

The diffusion equation given in 2.2 is a well-studied partial differential equation (PDE). Solving PDE requires knowing initial and boundary conditions. The discussion here is not intended to provide a general solution for PDE and we will focus on initial and boundary conditions relevant to charged-particle detection and imaging. Assuming ionization generation is a pulse at x = 0 and t = 0, that is,

$$P(0, t = 0) = \delta(x) = \begin{cases} \infty, x = 0 \\ 0, x \neq 0 \end{cases} \tag{2.3}$$

where δ(x) is the well-know delta function, then ionization electrons will undergo diffusion or equivalently, Brownian motion following Equation 2.1 or 2.2. For the sake of simplicity, an infinite body of silicon is assumed and thereby the boundary condition is given as

$P(x) = 0$, for $x \rightarrow \infty$ (2.4)

With Equation 2.3 and 2.4, Equation 2.2 can be solved by Fourier transform method. The Fourier transform pair of P(x,t) is given by

$$F(k,t) = \int_{-\infty}^{+\infty} P(x,t) e^{-ikx} dx \tag{2.5}$$

and

$$P(x,t) = \frac{1}{2\pi}\int_{-\infty}^{+\infty} F(k,t)e^{ikx}dk \tag{2.6}$$

Equation 2.2 can then be transformed into a first-order differential equation by plugging in Equation 2.6:

$$-k^2 F(k,t) = D\frac{\partial F(k,t)}{\partial t} \tag{2.7}$$

The solution of Equation 2.7 is straightforward

$$F(k,t) = \Phi(k)e^{-Dtk^2} \tag{2.8}$$

where Φ(k) is determined by the initial condition

$$\Phi(k) = F(k,0) = \int_{-\infty}^{+\infty} P(x,0)e^{-ikx}dx \tag{2.9}$$

Thus

$$F(k,t) = \int_{-\infty}^{+\infty} P(x,0)e^{-ikx}dx \cdot e^{-Dtk^2} \tag{2.10}$$

Then the solution can be obtained by taking the inverse Fourier transform

$$P(x,t) = \frac{1}{2\pi}\int_{-\infty}^{+\infty} e^{ikt}dk \int_{-\infty}^{+\infty} P(x,0)e^{-ikx}dx' \cdot e^{-Dtk^2} \tag{2.11}$$

Switch the sequence of k integral and x' integral

$$P(x,t) = \int_{-\infty}^{+\infty} P(x',0)dx' \frac{1}{2\pi}\int_{-\infty}^{+\infty} e^{ikx}e^{-ikx'}e^{-Dtk^2}dk \tag{2.12}$$

Evaluating the k integral first gives

$$P(x,t) = \int_{-\infty}^{+\infty} P(x',0)dx' \sqrt{\frac{1}{4\pi Dt}}\exp(-\frac{(x-x')^2}{4Dt}) \tag{2.13}$$

Equation 2.13 is essentially the Green's function representation of P(x, t), which is given by

$$\mathrm{G(x,t;x')} = \sqrt{\frac{1}{4\pi Dt}}\exp(-\frac{(x-x')^2}{4Dt}) \tag{2.14}$$

Green's functions have been widely used to solve PDEs with inhomogeneous boundary condition[34]. Substitute Equation 2.3 into 2.13,

$$P(x,t) = \int_{-\infty}^{+\infty}\delta(x')dx'\sqrt{\frac{1}{4\pi Dt}}\exp(-\frac{(x-x')^2}{4Dt}) \tag{2.15}$$

Considering the fundamental property of δ function

$$f(x) = \int_{-\infty}^{+\infty} f(x')\delta(x'-x)dx' \tag{2.16}$$

The solution is derived as

$$P(x,t) = \sqrt{\frac{1}{4\pi Dt}}\exp(-\frac{x^2}{4Dt}) = G(x,t;0) \tag{2.17}$$

It is convenient to rewrite Equation 2.17 in terms of Einstein relationship

$$\sigma = \sqrt{2Dt} \tag{2.18}$$

where D is the diffusion coefficient and σ is the mean displacement in time t. Then the solution can be converted into an easily recognized form

$$P(x,t) = \frac{1}{\sqrt{2\pi}\sigma}\exp(-\frac{x^2}{2\sigma^2}) \tag{2.19}$$

which is the Gaussian distribution with mean zero and variance σ^2. Intuitively, if there are N_0 electrons in the pulse at t = 0, then the distribution of electrons in time and x is

$$N(x,t) = \frac{N_0}{\sqrt{2\pi}\sigma}\exp(-\frac{x^2}{2\sigma^2}) \tag{2.20}$$

The calculation above demonstrates that Brownian motion and diffusion can be modeled using Gaussian random numbers in a Monte Carlo approach. The following section will present the Monte Carlo modeling of the Brownian motion of electrons in silicon.

2.2.2 Monte Carlo Simulation of Electron Diffusion or Brownian Motion

To facilitate the explanation, two random numbers are introduced:

1) randu: a uniformly distributed random number between 0 and 1
2) randn: a random number following a Gaussian distribution with a mean of zero and a variance of σ^2.

We postpone the generation of random numbers to the next section. The Brownian motion of an electron is first simulated in two-dimension. The displacement (r) per step is modeled as $\sigma \cdot$ randn it could be in any direction with equal probability, that is, $\theta = pi \cdot$ randu. The new x-y coordinates is then $x_{i+1} - x_i = r \cdot \cos(\theta)$ and $y_{i+1} - y_i = r \cdot \sin(\theta)$. The same procedure is then repeated over and over again and the coordinates (x, y) at each step are recorded. Many simulation runs have been performed for different particles with different step sizes. The movement of individual particles and the collective behavior will be discussed in detail in the following few paragraphs.

Figure 2.1 (a), (b), (c), and (d) depict the random movement of an electron after 50, 500, 1000, and 10,000 random-walk steps, respectively. The σ used is 80 nm. The particle set off at (x, y) = (0, 0), after the 50^{th} step, it reached (x, y) = (-0.3, 0.6). After 1000 random-walk steps, the particle reached (x, y) = (-3.91, -1.35), which is around 4 μm away from the origin. Then it turns back to the origin in random-walk afterwards and after 10,000

steps, it reaches (x, y) = (-5.28, -8.61), around 10 μm away from the origin. The movement of the electron only depended on its most immediate prior location and had no memory about its histry. The displacement (σi) between two consecutive time instance t+s and s is a random variable following normal distribution. Given enough time, it is likely that this particle will traverse the entire plane.

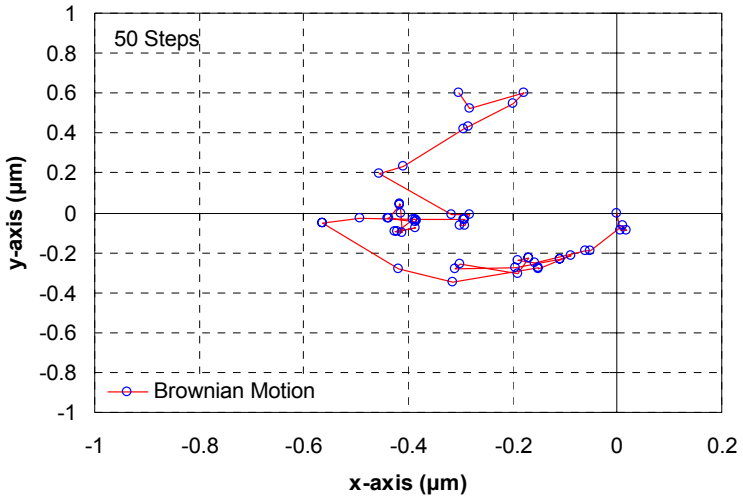

(a) Random-walk in 50 steps.

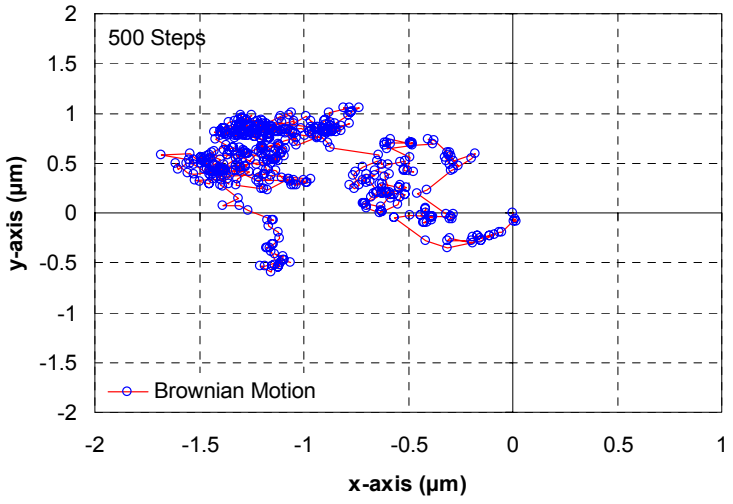

(b) Random-walk in 500 steps.

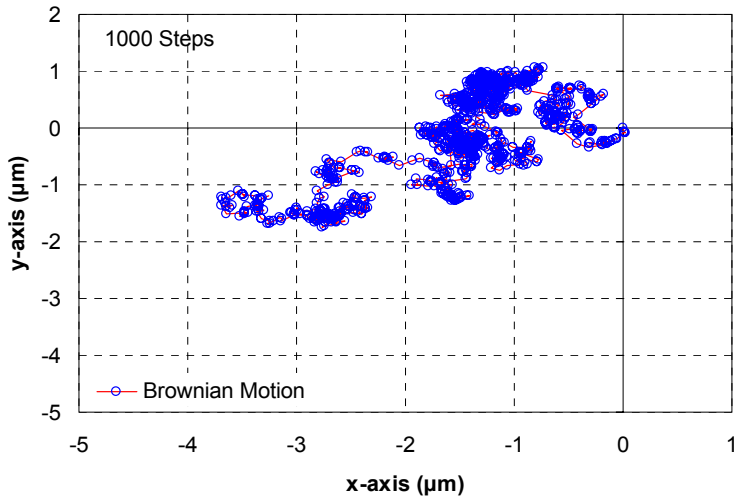

(c) Random-walk in 1000 steps.

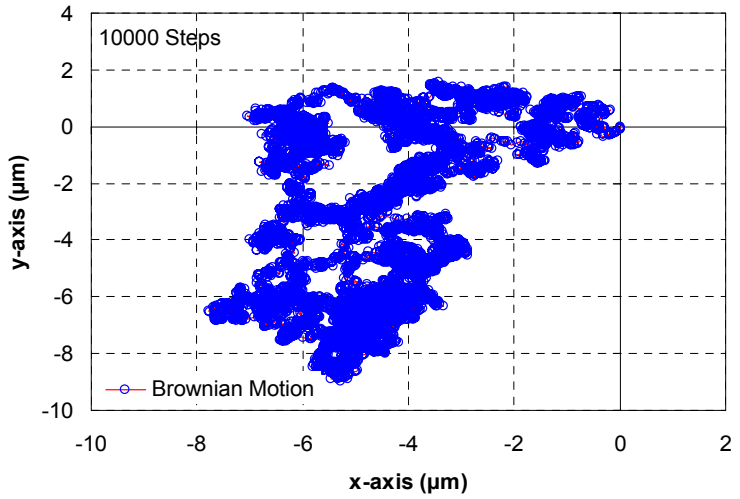

(d) Random-walk in 10,000 steps.

Figure 2.1: Monte Carlo simulation of the Brownian motion of an electron in a two-dimensional space.

Figure 2.1 demonstrates that an electron with very small step size in Brownian motion can reach a location far away from its origin, a phenomenon quite contrary to what we usually observe for a droplet of red ink in clear water. It is much more meaningful to look at the collective behavior of an ensemble of electrons. That said, we plot the histogram of 500 and 10,000 individual Brownian particles in Figure 2.2 (a) and (b), respectively. The

simulation setup is exactly the same as the particle discussed in Figure 2.1 and the number of steps simulated is 1000. The histogram is normalized to the total number of particles simulated and the size of the bin and thus reflects the probability density. Both figures show that most of the electrons are still in the vicinity of the origin after 1000 steps, although a small portion of them moved far away. The simulated histogram overlaps well with the Gaussian distribution we derived in Equation 2.19 and 2.20. The nice agreement between the simulation and the theory indicates once again indicates that Monte Carlo method is suitable for treating random particles.

Another important indication of Figure 2.2 is the accuracy of Monte Carlo simulation. For the simulated mean and standard deviation, those calculated from 10,000 particles are much closer to the theoretical values than those calculated from only 500 particles. The accuracy or convergence related issues for estimating unknown variables have been thoroughly studied in statistics and the following section will present a quick overview.

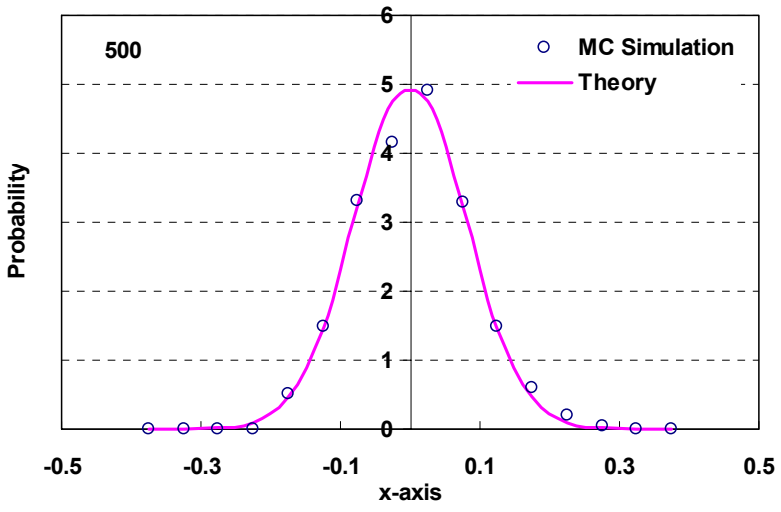

(a) Mean = 0.0012, σ = 0.0822

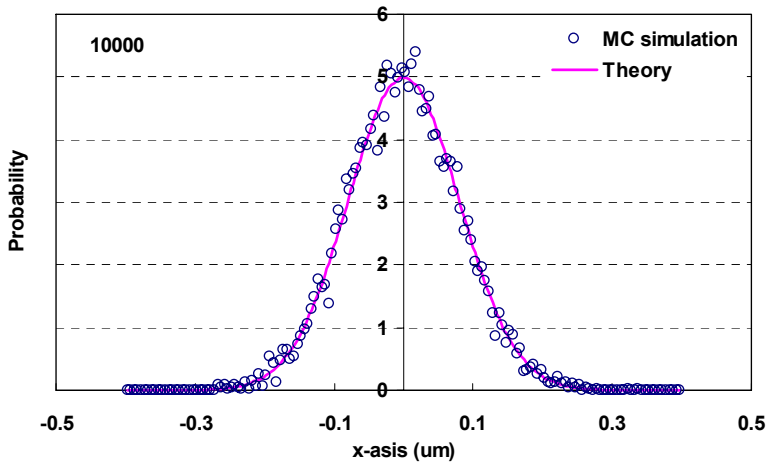

(b) Mean = 0.0004, σ = 0.0798

Figure 2.2: Histogram of random particles undergoing Brownian motion simulated by Monte Carlo method. (a) Histogram of 500 particles, (b) Histogram of 10,000 particles. The solid curves in (a) and (b) are the theoretical Gaussian distribution in Equation 2.19 and 2.20.

2.2.3 The Law of Large Numbers, Central Limit Theory and Confidence Interval*

Many real-life problems necessitate an estimation of unknown variables in a quantitative manner. The Law of Large Numbers says the sample mean of any random variable with large enough sample size approaches the true expected value of the random variable. In mathematics, it takes two forms. The weak form is given by

$$\lim_{n\to\infty} P\left[\left|M_n - \mu\right| < \varepsilon\right] = 1 \tag{2.21}$$

and the strong form is given by

$$P\left[\lim_{n\to\infty}\left[M_n = \mu\right]\right] = 1 \tag{2.22}$$

where the sample mean is

$$M_n = \frac{1}{n}\sum_{j=1}^{n} X_i \tag{2.23}$$

* This subsection is mainly adopted from A. Leon-Garcia, *Probability and Random Processes for Electrical Engineering*, 2nd ed: Prentice Hall, 1993.

and μ is the true mean of an bounded unknown variable (X) and ε is an infinitely small positive number[35]. The weak form states that the sample mean will be close to the true mean with high probability. The strong form states that with probability one, every sequence of sample mean calculation will eventually approach and stays close to the true mean. The Law of Large Numbers has been the most widely used theory in statistics. The Law of Larger Numbers indicates that the sample means of experimental measurement or Monte Carlo simulation results converges to the expected values contingent that the sample size is large enough.

A second important theory in statistics that is relevant to our research is the Central Limit Theorem, which says that the sum of many independent, identically distributed random variables is approximately normally distributed as long as they have a finite mean and finite variance[35]. Let the sum of n random variable to be

$$S_n = \sum_{i=1}^{n} X_i \tag{2.24}$$

and normalize S_n to a random variable with zero-mean and unit variance

$$Z_n = \frac{S_n - n\mu}{\sigma\sqrt{n}} \tag{2.25}$$

then

$$\lim_{n\to\infty} P[Z_n \le z] = \frac{1}{\sqrt{2\pi}} \int_{-\infty}^{z} e^{-x^2/2} dx \tag{2.26}$$

Many phenomena in physical world result from the addition of numerous independent random processes and the averages in experimental measurement and simulation runs also consist of the sum of independent random variables. These can all be approximated

using normal distribution according to the Central Limit Theorem. As an example, we show in Figure 2.3 that the sum of 1000 independent Gaussian variables and show that it indeed follows Gaussian distribution.

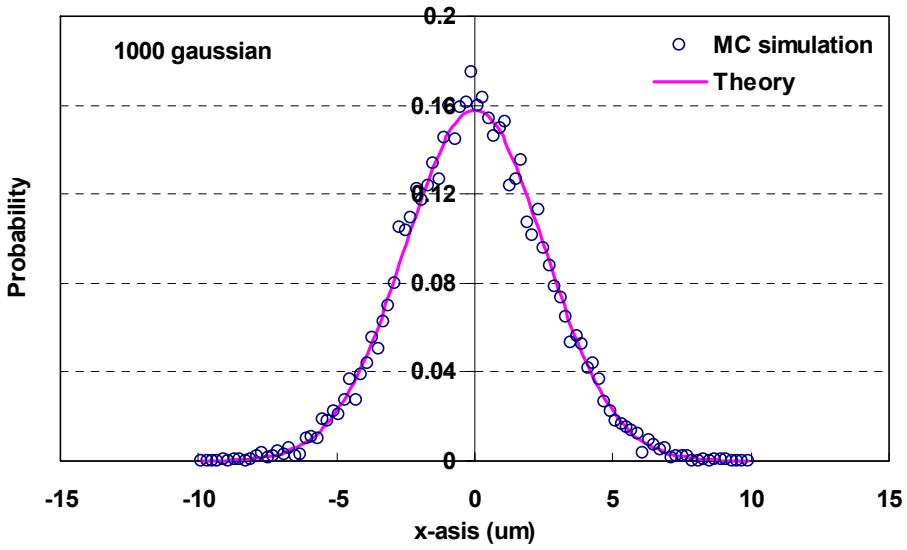

Figure 2.3: 1000 independent Gaussian random variables simulated using Monte Carlo method still follows Gaussian distribution.

The sample mean provides us with a single numerical value for the estimate of the true mean μ. But with a finite sample size in practice, the sample mean converges to but is not exactly the true mean of the unknown quantity. In order to characterize the convergence of our estimate, a sample variance given as follows should be calculated

$$V_n^2 = \frac{1}{n-1}\sum_{j=1}^{n}(X_j - M_n)^2 \qquad (2.27)$$

If V_n^2 is small, then the observations are tightly clustered about M_n, and we can be confident that M_n is close to the μ. Otherwise, if V_n^2 is large, then the samples are widely dispersed about Mn and we can not be confident that Mn is close to μ. A general treatment of the convergence of sample mean to the true mean is through the concept of

confidence intervals. In statistics, the introduction of confidence intervals is through a special probability distribution called Student's t-distribution with n-1 degrees of freedom[35]:

$$f_{n-1}(y) = \frac{\Gamma(n/2)}{\Gamma((n-1)/2\sqrt{\pi(n-1)}}(1+\frac{y^2}{n-1})^{-n/2} \tag{2.28}$$

Then the confidence interval with confidence level 1- α is given by

$$(M_n - z_{\alpha/2,n-1}V_n/\sqrt{n}, M_n + z_{\alpha/2,n-1}V_n/\sqrt{n}) \tag{2.29}$$

where $z_{\alpha/2,n-1}$ can be obtained from a special Student's t-distribution look-up table. The confidence interval given in (2.29) can be used to the study sample mean convergence problem for any random variables besides Gaussian random variable through the method of batch means[35].

2.2.4 Monte Carlo Method vs. Deterministic Method

Numerical methods are indispensable in dealing with real-life partial differential equations with complicated boundary and initial conditions. Among them, finite element analysis and finite difference analysis are deterministic methods and Monte Carlo falls into the category of non-deterministic or stochastic methods. We briefly examine the comparison of these methods in terms of accuracy, speed, and applicability from a practitioner's perspective[36].

Accuracy: Monte Carlo method is built upon first principles and always converges to the true solution. Finite element analysis and finite difference analysis are also accurate with adequate mesh or difference at low dimensions.

Speed: Deterministic methods are usually faster than Monte Carlo method and require less computation resource. Monte Carlo method is relatively slow compared with finite element method and finite difference method at low dimension.

Applicability: Monte Carlo method is very robust and is typically advantageous in dealing with problems with multiple dimensions and complicated boundary and initial conditions. The application of deterministic methods to multi-dimensional problems is usually rather limited. The convergence of finite element method and finite difference method is not trivial in dealing with non-linear euqations and problems with exotic boundary conditions.

With the continued reduction in computation cost and easier access to high performance computation resource, Monte Carlo method will likely continue to gain increased acceptance in a wide range of applications.

2.3 Modeling X-ray and High Energy Electron Ionization Generation

2.3.1 X-ray photon and silicon interaction: exponential distribution

^{55}Fe 5.9 keV X-ray have been a standard radiation source for characterizing the charge-to-voltage conversion gain and charge transfer efficiency in image sensors including CCDs and CMOS imager sensor [16]. Carrying no charge, ^{55}Fe 5.9 keV X-ray photons interact with silicon by photo-electric effect and the transmission of x-ray photon in silicon follow Lambert-Beer's law,

$$\frac{I}{I_0} = e^{-z/\lambda_x} \tag{2.30}$$

where I is the intensity of transmitted photon beam, I_0 is that of the incident photon beam, and λ_x is the absorption length. For ^{55}Fe 5.9 keV X-rays, λ_x is ~ 27 μm[†][37]. Then the cumulative density function (CDF) of absorption at depth z in silicon is given by

$$F_x(z) = 1 - \frac{I}{I_0} = 1 - e^{-z/\lambda_x} \tag{2.31}$$

and the corresponding probability density function is

$$f_x(z) = \frac{1}{\lambda_x} e^{-z/\lambda_x} \tag{2.32}$$

A random number representing the random depth of x-ray photon absorption can be found by inverse transform method. Assuming an x-ray photon is absorbed at z, which is a random variable following Equation 2.31 and 2.32, then the CDF up to point z, $F_x(z)$ is itself a random variable which will occur with uniform probability density within [0, 1]

[†] A simple equation to estimate is $\lambda_x = 1/(\rho\sigma)$, where ρ is the density of silicon, σ is the cross-section. ~ 29 μm can be estimated this way [Janesick 2001].

$$randu = F_x(z) = 1 - e^{-z/\lambda_x} \tag{2.33}$$

By inverse transform, Equation 2.33 can be re-written as

$$z = -\lambda_x \log_e(1 - randu) \tag{2.34}$$

As *randu* is a uniformly distributed random number between 0 and 1, *1-randu* is also a random number of the same distribution in the same range and so can be replaced by yet another random number *randu* and thus

$$z = -\lambda_x \log_e(randu) \tag{2.35}$$

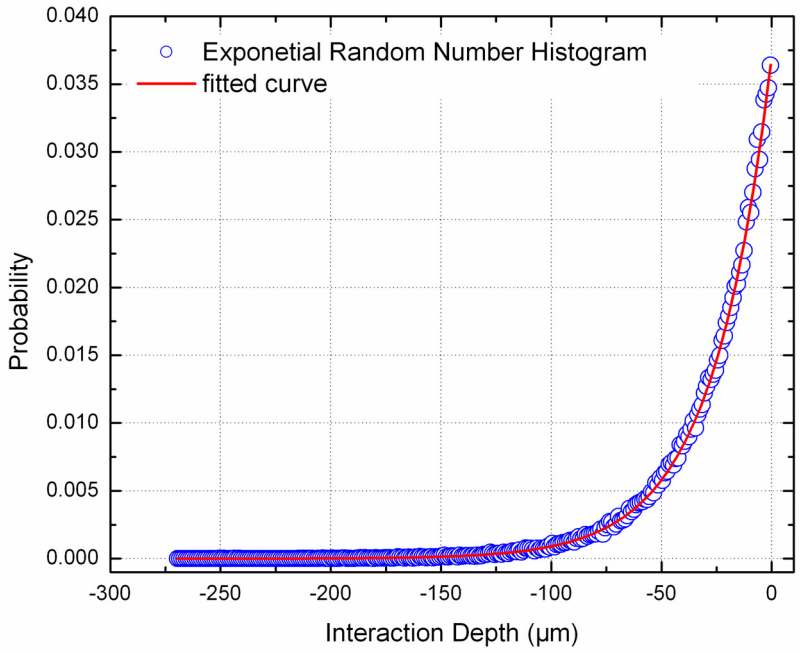

Figure 2.4: Histogram of the interaction depth fitted to exponential distribution (z value is mirrored with respect to z = 0).

Figure 2.4 plots the normalized histogram of 10,000 exponential random numbers generated following Equation 2.35. The solid line is the curve fit using the probability density function shown in Equation 2.32. The normalized histogram fits the theoretical curve very well. From Equation 2.32, the mean absorption depth is

$$E(z) = \int_0^\infty f_x(z) \cdot z \cdot dz = \int_0^\infty \frac{1}{\lambda_x} e^{-z/\lambda_x} \cdot z \cdot dz = \lambda_x \int_0^\infty e^{-t} \cdot t \cdot dt = \lambda_x \tag{2.36}$$

and the variance

$$Var(z) = E((z - E(z))^2 = E(z^2 - 2zE(z) + E^2(z)) = E(z^2) - E^2(z) \tag{2.37}$$

and

$$E(z) = \int_0^\infty f_x(z) \cdot z^2 \cdot dz = \int_0^\infty \frac{1}{\lambda_x} e^{-z/\lambda_x} \cdot z^2 \cdot dz = \lambda_x^2 \int_0^\infty e^{-t} \cdot t^2 \cdot dt = 2\lambda_x^2 \tag{2.38}$$

Thus

$$Var(z) = \lambda_x^2 \tag{2.39}$$

The comparison between the simulated mean and variance for 10,000 random numbers and the theoretical values calculated from Equation 2.36 and 2.39 is listed in Table 2.1. Again the simulated results with only 100, 1000 samples are also shown for comparison. The increase in sample size drastically improves the convergence of the simulation.

Table 2.1: Comparison between Monte Carlo simulation and analytical solution for exponential distribution.

	Mean	Variance	Mean Error	Variance Error
Analytical Solution	26.95	726.3	/	/
MC 100 runs	25.82	1035.5	-0.04193	0.425719
MC 1,000 runs	26.78	732.6	-0.00631	0.008674
MC 10,000 runs	26.95	728.6	0	0.003167

* MC = Monte Carlo

The mean and variance listed in Table 2.1demontrate that x-ray photon absorption and thus ionization generate can occur very deep inside the silicon. From the simulation, the percentage of photons absorbed in up to 10 μm of silicon is only 31%. A silicon thickness

equal to the average absorption depth (~27 μm) accounts for only 63% of the total number of x-ray photons absorbed. This is in sharp contrast to visible light absorption: for blue light, nearly all absorption occurs in a very thin silicon layer, while for red light, it can penetrate deeper, ~10 μm into silicon [16]. More specifically, a typical sensor array in 0.25 μm process we have been using has ~8 μm epitaxial silicon layer. Following the same calculation, the epitaxial layer will account merely ~26% of the total number of x-ray photons absorbed. Most of the X-rays are absorbed in the bulk substrate below the epitaxial layer, and need to be accounted for.

2.3.2 High Energy Electron and Silicon Interaction: Bichsel Distribution

The interaction of high energy electrons with silicon is different from that of X-ray photons in that electrons are charged particles and Coulomb interaction is the dominant mechanism. The detailed process of interaction is energy dependent. Low energy electrons (< 50 keV) have been used in scanning electron microscopy. In this range, electron-hole pairs are generated in silicon by inelastic scattering of impinging electrons or secondary electrons. Imaging applications in this energy range have been discussed by Deptuch et al. [38]. When the energy of incident electrons is high (above a few tens of MeV), electromagnetic radiation (bremsstrahlung) starts to dominate [15]. The energy range we are interested in for imaging applications in electron microscopy is from 80 keV to 1000 keV, such as those typically used in transmission electron microscopy. In this region, the structural information of object under test can be retrieved from electrons through elastic scattering and ionization is the dominating mechanism for electron-hole pair generation[15].

Energy deposition of high energy electrons in solid state materials have been intensely studied in high energy physics. Different from the photo-electric interaction between x-ray photon and silicon, electrons interact with silicon via a Coulomb force. In 1944, Landau [39]developed a statistical theory to characterize energy deposition by high energy particles.

$$\phi(x) = \frac{1}{2\pi \cdot i}\int_{c-i\infty}^{c+i\infty} e^{u\cdot\log_e(u)+x\cdot u}du, c \geq 0 \tag{2.40}$$

This theory is later refined by Bichsel et al.[17, 40] to accommodate substantial individual collisions in thin silicon detectors and the energy loss straggling functions, but neglects electromagnetic radiation (Bremsstrahlung) at high energy in thin silicon detectors. Bichsel's theory has been confirmed by experimental measurements[41]. Additionally, Bichsel's algorithm has been implemented as a Fortran program[‡] to generate ionization histograms, which can then be integrated with our Monte Carlo model.

There is no simple analytic equation to describe Bichsel's model of ionization generation in silicon due to high energy electrons. For Monte Carlo analysis, however, a random number generator needs to be developed. The basic idea is to map Bichsel's distribution to a uniform distribution. A higher chunk in the Bichsel distribution is mapped to a wider chunk in the uniform distribution. This one-to-one mapping between Bichsel distribution and uniform distribution is depicted in Figure 2.5.

[‡] Dr. Howard Matis kindly provided me with the Fortran source code that was written by Dr. Hans Bichsel.

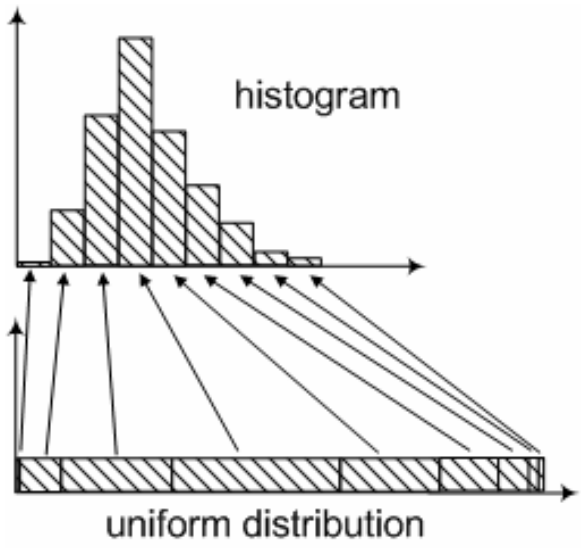

Figure 2.5: Mapping Landau distribution to a uniform distribution. A higher chunk in the Bichsel distribution is mapped to a wider chunk in the uniform distribution.

Then the histogram random number generator for Bichsel distribution follows a two-step process:

Step 1: Create a two-column lookup table of the cumulative distribution based on the histogram given. Column I (xr_i, i = 1, 2, ⋯, n) is the individual values on the abscissa axis of the histogram. The elements in Column I are listed in a sequential manner. Column II (yc_i, i = 1, 2, ⋯, n) is the cumulative probability corresponding to each value in column I. The last element in Column II is the value of the total cumulative probability.

Step 2: Generate random numbers by interpolation based on the lookup table. In order to generate a random number following the histogram distribution, a random number from a uniform distribution (*randu*) between zero and the total cumulative probability has to be generated first. Next, we implement a simple algorithm to find the next greater value

(yc_{i+1}) for the uniform random number in column II of the lookup table. Then the random number following the original Bichsel distribution (*randb*) is given by:

$$randb = xr_i + \frac{randu - yc_i}{yc_{i+1} - yc_i}(xr_{i+1} - xr_i) \tag{2.41}$$

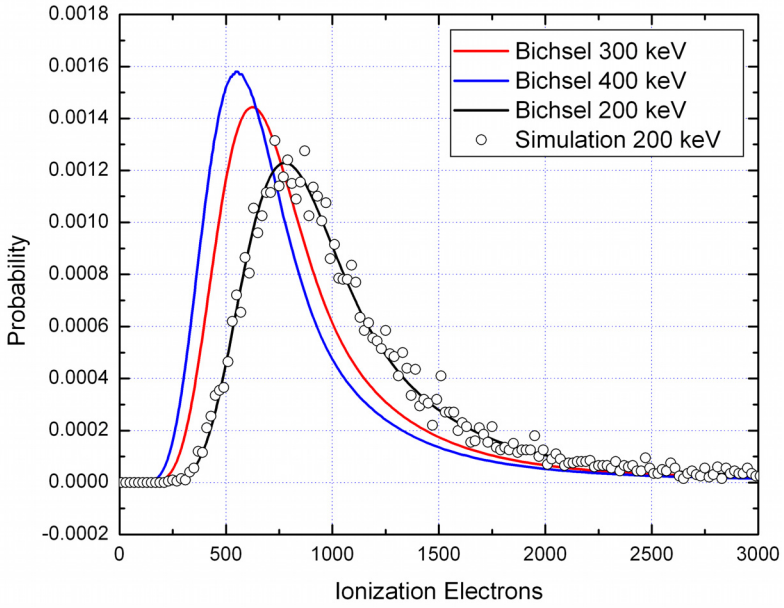

(a)

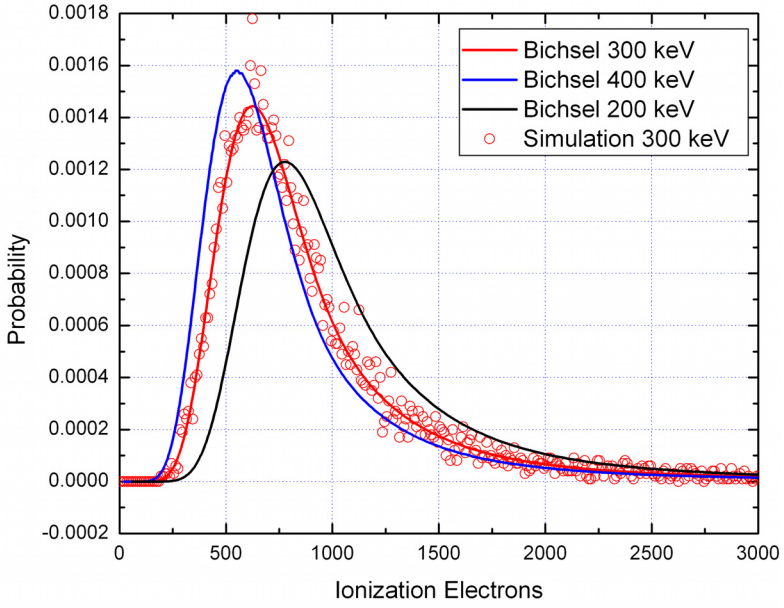

(b)

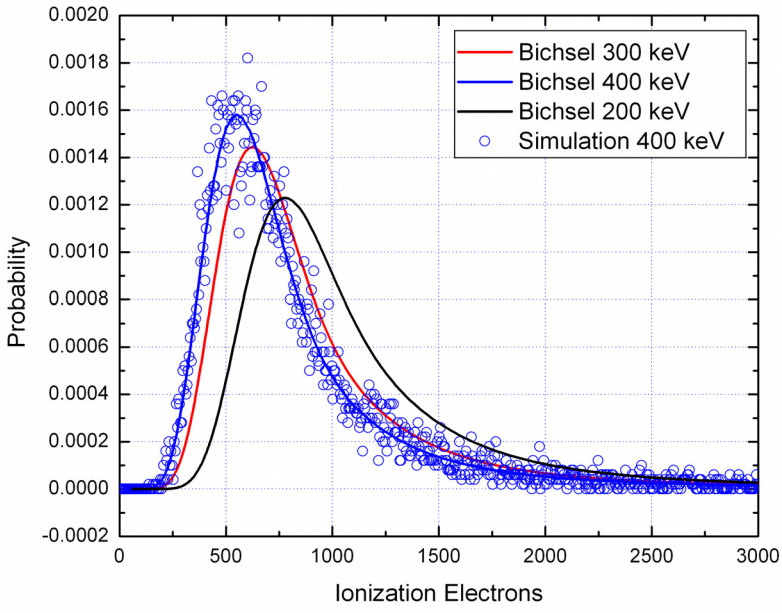

(c)

Figure 2.6: Normalized histogram of ionization electrons generated using the histogram random number generator at different energies. (a) 200 keV, (b) 300 keV, (c) 400 keV electrons. Silicon thickness: 9 μm.

Two most important factors that need to be deliberately considered in our research are the energy of incident electrons and the silicon thickness.

In Figure 2.6, we plotted the generation of ionization electrons in about 9-μm silicon at three different energy values. The x-axis is the number of ionization electrons generated and the y-axis is its probability. Tens of thousands of Bichsel-distributed random numbers were produced following the histogram random number generation algorithm. The histogram is then normalized such that the total area underneath was equal to one so that it can be compared with the probability density function of Bichsel distribution. The solid curves correspond to the data points obtained from Bichsel's Fortran program. The calculated histograms agree well with Dr. Bichsel's theory. From Figure 2.6, Bichsel distribution features a most probable value at lower end and a long tail goes to very large

positive values. The most probable value has been widely used to characterize ionization under different conditions. It is clear that the higher the energy of incident electrons, the smaller the most probable value in Bichsel distribution and this trend is well maintained in the energy range from 100 keV to 1000 keV in simulation. Higher energy electrons are less likely to interact with silicon lattice and the energy transferred during each interaction is also lower than that at lower energy. However, Electrons with lower energy are prone to be stopped completely inside silicon and deposit all of it as kinetic energy, which often leads to back-scattering of the incident electrons, an effect that is detrimental to image quality in solid-state sensors but not yet considered in the current model.

In Figure 2.7, we plotted the histograms of Bichsel distribution for different silicon thickness. The three solid curves correspond to the Bichsel histograms at: 4 μm, 8 μm, and 20 μm, respectively. The energy of incident electrons is 300 keV. For given silicon thickness, it is more likely for an incident electron to deposit more energy in thicker silicon than in thinner one. Bichsel random numbers representing the number of ionization electrons generated in given silicon thickness are also plotted in each figure in Figure 2.7. The simulated histograms agree with the theory remarkably well.

Ionization generation modeled using Bichsel random numbers will be plugged into the Monte Carlo framework to simulate the collection matrices of individual impinging high energy electrons. The influence of incident electron energy and silicon thickness (epitaxial silicon and bulk substrate silicon) on sensor performance will be systematically studied.

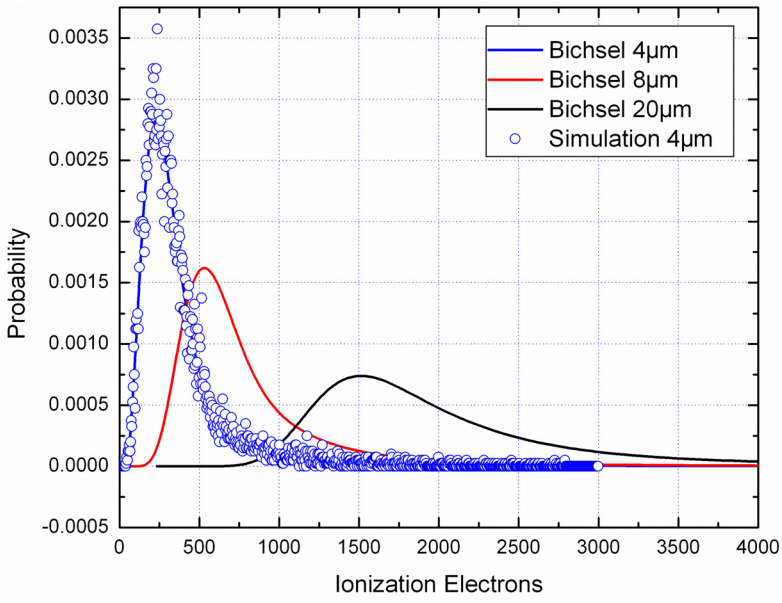
Bichsel 4μm
Bichsel 8μm
Bichsel 20μm
Simulation 4μm
Probability
Ionization Electrons
0.0035
0.0030
0.0025
0.0020
0.0015
0.0010
0.0005
0.0000
-0.0005
0
500
1000
1500
2000
2500
3000
3500
4000

(a)

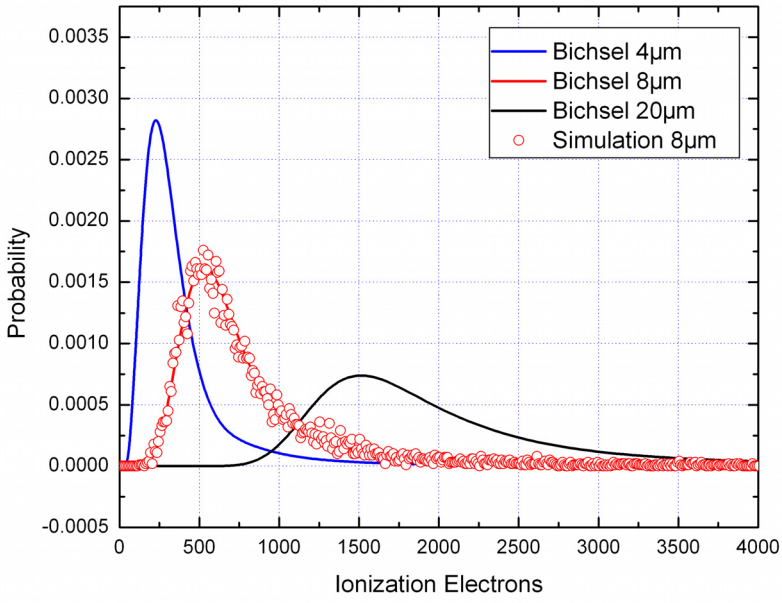
Bichsel 4μm
Bichsel 8μm
Bichsel 20μm
Simulation 8μm
Probability
Ionization Electrons
0.0035
0.0030
0.0025
0.0020
0.0015
0.0010
0.0005
0.0000
-0.0005
0
500
1000
1500
2000
2500
3000
3500
4000

(b)

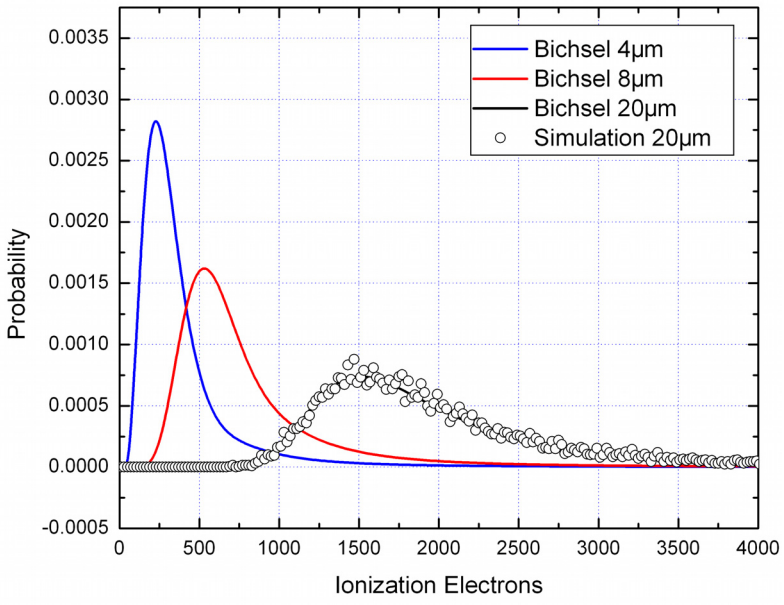

(c)

Figure 2.7: Normalized histogram of ionization electrons generated using the histogram random number generator at different silicon thickness. (a) 4 μm, (b) 8 μm, (c) 20 μm. Energy of impinging electrons: 300 keV.

2.4 Charge Transport Equation and a General Solution

Ionization electrons generated in silicon leads to local charge in-equilibrium and the concomitant evolution toward equilibrium is governed by transport equation [14]

$$\frac{\partial n}{\partial t} = D_n \cdot \nabla^2 n - \frac{n}{\tau_n} + n \cdot \mu_n \nabla \varepsilon + \mu_n \cdot \varepsilon \cdot \nabla n + G(x, y, z) \tag{2.42}$$

where D_n, μ_n and τ_n are diffusion coefficient, mobility and carrier lifetime, respectively. The source term $G(t, x, y, z)$ is determined by the ionization process. Approximating $G(t, x, y, z)$ as a delta function at time zero and low-level injection in p-type silicon free of electric field, Equation 2.42 can be simplified into

$$\frac{\partial n}{\partial t} = D_n \cdot \nabla^2 n - \frac{n}{\tau_n} \tag{2.43}$$

with initial conditions given by $G(t=0,x,y,z)$. Considering only one dimension, the only difference between Equation 2.43 and Equation 2.2 is the recombination term in the former. Re-write n(t,x) as the product of an exponential decay term and p(t,x), that is,

$$n(t,x) = \exp(-t/\tau)\, p(x) \tag{2.44}$$

Then Equation 2.43 is exactly the same as Equation 2.2. Therefore, the general solution for Equation 2.43 is given by

$$n(t,x) = \exp(-t/\tau)\frac{1}{(4\pi Dt)^{1/2}}\exp(-x^2/4Dt) \tag{2.45}$$

Applying Einstein relationship $\sigma = \sqrt{2Dt}$,

$$n(t,x) = \exp(-t/\tau)\frac{1}{\sqrt{2\pi}\sigma}\exp(-x^2/2\sigma^2) \tag{2.46}$$

Equation 2.46 suggests that if at time zero we inject a pulse of electrons, the distribution of these electrons follows a Gaussian distribution and the total number of electrons decay exponentially. From microscopic point of view, ionization electrons undergo Brownian motion in time. For a given time step Δt, the corresponding the step size in displacement is determined by Einstein relationship and can be re-written as

$$\sigma = \sqrt{2D\Delta t} \tag{2.47}$$

and corresponding recombination rate is

$$rr = 1 - e^{-\Delta t/\tau} \tag{2.48}$$

Equation 2.47 and 2.48 give two most important parameters in constructing the Monte Carlo model. The time step has to be properly selected to allow meaningful simulation in

an acceptable time frame and similar derivation of Equation 2.47 and 2.48 can be found in reference [22, 28, 42].

2.5 Device Parameters and Boundary Conditions

As demonstrated in the cross-sectional view in Figure 1.1, an APS pixel can be divided into four regions: p-substrate, p-epi, p-well, and n-well. The differences of these four regions in terms of dopant type, doping density, defect density, and electric field leads to drastically different response to ionization electrons.

2.5.1 n-well and n-well/p-epi and n-well/p-well depletion region -- active collection region

In the integration-phase of APS operation, there is a depletion region at the n-well/p-well boundary and n-well/p-epi boundary. The depletion region in addition to the physical n-well region serves as the active collection region. Electrons generated or migrating into these regions are swept to the sensing node of the APS pixel and collected as signal electrons. The depletion width can be calculated using ISE-TCAD or step-junction approximation.

2.5.2 Bulk epitaxial silicon region

With an effective reset voltage is ~ 2 V (Vdd-$V_{th,reset}$), most of the epitaxial silicon is not depleted except the region very close to the n-well. The bulk p-epi region is defined as the epitaxial silicon free of electric field. Electrons diffuse rather than drift in the bulk p-epi region and the relaxation of locally generated ionization electrons follows Equation 2.46. In addition, p-epi is lightly doped and is of high quality. The minority carrier

lifetime is on the order of 10^{-6} to 10^{-5} second[37, 43]. Electron diffusion in bulk p-epi experience five different means of interaction:

1) reach the interface between p-bulk and active collection region and be collected.

When p-epi electrons hit the n-well/p-epi depletion region, they will be swept into the sensing node by the electric field and be collected. The electrical potential φ_B can be calculated from Equation 1.3 to be 0.658 V, which can be translated into a reflection coefficient using Boltzmann's formalism of thermal dynamics[44]

$$r_{reflection} = e^{-q\cdot\varphi_B / kT} \tag{2.49}$$

where φ_B is the potential barrier in volts, q is the charge of an electron, k is Boltzmann constant and T is the temperature in Kelvin. Plugging in all the numbers, the reflection coefficient is found to be ~ 10^{-11}. That is, electrons hit the boundary between p-epi and the depletion region has very little chance to be reflected but pass through. Consequently, the n-well/p-epi interface can be recognized as a boundary with total absorption.

2) hit p-epi/p-well interface and be reflected.

In contrast to p-epi/depletion interface, because p-well is much more heavily doped than epitaxial silicon, p-well/epi interface is reflective for electrons in the epitaxial silicon and the potential barrier is given by

$$V_{b,p-well} = \frac{kT}{q}\log_e\left(\frac{N_{A,p-well}}{N_{A,p-epi}}\right) \tag{2.50}$$

which is nearly 0.12 V. The reflection calculated following Boltzmann's formulism is very close to 1. Therefore, the p-well/p-epi interface can be recognized as a boundary with total reflection for electrons in the epitaxial silicon.

3) hit p-epi/p-substrate interface and be reflected.

Similar to p-well/epi interface, p-substrate/p-epi interface is also reflective for electrons in the epitaxial silicon and the potential barrier is given by

$$V_{b,p-sub} = \frac{kT}{q}\log_e\left(\frac{N_{A,p-sub}}{N_{A,p-epi}}\right) \tag{2.51}$$

which is nearly 0.24 V. The reflection calculated following Boltzmann's formulism is again very close to 1. Therefore, the p-substrate/p-epi interface is recognized as a boundary with total reflection for electrons in the epitaxial silicon.

4) recombine and disappear.

In theory, the recombination rate for an electron in time step Δt in epitaxial silicon can be determined from Equation 2.48 for given electron lifetime. However, it is not trivial to precisely determine electron lifetime, which usually depends on the specific process and technology. We used ~ 10 μs as the electron lifetime in the epitaxial silicon after going over a number of references [37, 43, 45, 46] . Plugging it into Equation 2.48, we obtain a recombination rate on the order of 10^{-7}. As the precise lifetime depends on material properties that is only available through experimental measurement, these estimated values serves only as the starting point for simulation and they need to be refined by comparing the simulation with the measurement. Another issue adds to the complexity of electron lifetime is radiation damage. With continuous illumination using high energy

particles such as X-ray and hundreds of keV electrons, electron lifetime is likely to degrade over time. Radiation damage to the APS array will be visited later. In the simulation, the recombination rate is determined from a combination of theory and experimental measurement using x-ray photons.

5) remain inside p-epi after the conclusion of an entire integration phase.

It is possible that electrons in the epi layer remains elusive even after a long period of integration time (10ms ~ 100 ms). However, both measurement and simulation show that these elusive electrons are negligible in this kind of timeframe.

2.5.3 Bulk p-substrate region and p-well region

Because p-substrate has much higher doping density than p-epi and the quality is also lower, the electron lifetime in p-substrate is much shorter. Similar to the method in dealing with the epitaxial silicon, a lifetime of ~10 ns is estimated for electrons in the bulk substrate and the corresponding recombination rate is on the order of ~ 10^{-4}. Previous literatures assume the p-substrate recombination rate to be 100% and thus reaching a conclusion that the bulk substrate contribution is completely neglected. In our simulation, a more realistic and non-unitary substrate recombination rate is proposed and tuned by comparing the simulation results with experimental measurement. Another important finding is that the p-substrate/p-epi boundary is transparent for electrons in the bulk substrate, as compared to completely reflective for electrons in the epitaxial silicon. The finite substrate recombination rate and a transparent p-substrate/p-epi interface for

electrons in the substrate lead to significant substrate contribution. This topic will be treated systematically in Chapter 4 and Chapter 5.

For electrons in the p-well region, the picture is different and more complicated. First, as three NMOS transistors are all built in p-well, additional pn junctions associated with these transistors work as high efficiency electron sink and p-well ionization electrons generated in the vicinity are directly absorbed and will not contribute to the final collection matrices. Additionally, p-well is usually very thin and the number of electron generated by electron beam small Furthermore, because of the high doping density, defects, and surface traps, the recombination rate of p-well is much larger than that of p-epi. Consequently, ionization electrons generated in the p-well will be neglected and do not enter the Monte Carlo simulation.

The time increment Δt used is on the order of 10^{-12} s, similar to those reported in references [22, 28, 42, 47], quite close to the average collision time in Drude model[48]. Using an electron diffusion coefficient (D_n) ~ 35 cm^2/s, the step size σ from Equation 2.47 is about 80 nm, once again close to the mean-free-path of electrons in silicon estimated by Drude model.

2.6 Monte Carlo Algorithm

High energy physics experiments have commonly used collection matrices that consist of an array of pixels centered on the struck pixel[11, 49] to characterize sensor response to individual incident particles. A pattern recognition algorithm is usually used to identify

collection matrices corresponding to individual impinging particles[11, 50]. Simply put, a collection matrix is identified by looking for a square pixel array centered on a pixel with highest signal level locally. The real-life implementation of this algorithm also addresses double hits, multiple hits, and noise. This pattern recognition algorithm results in a large number of collection matrices for individual incident particles. The collection matrices presented in this manuscript were measured by our collaborators at Lawrence Berkeley National Laboratory and UC San Diego. The goal of our Monte Carlo simulation is to calculate numerous collection matrices corresponding to individual impinging particles and compare them with the experimental measurement, thus providing insights on sensor design and optimization.

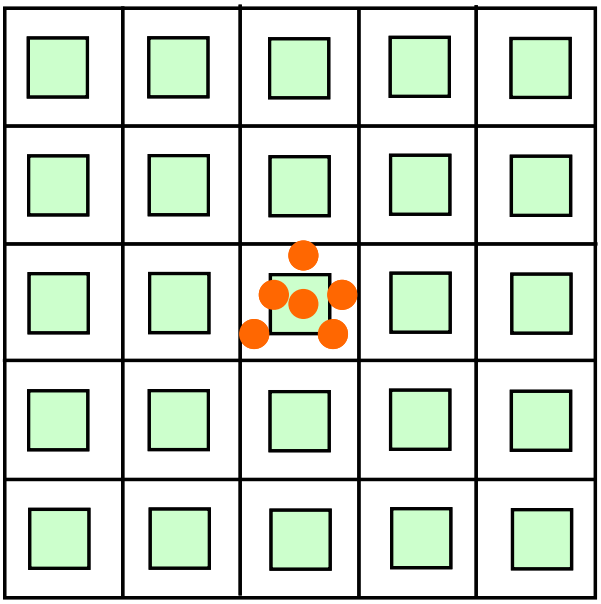

Figure 2.8: Conceptual view of random hits in the center of a 5 by 5 pixel array.

In order to generate collection matrices for individual incident particles in the Monte Carlo simulation, an incident particle is assumed to strike the center pixel of a pixel array consisting of 2n+1 by 2n+1 identical pixels each with a diode in the center. The top view

of the pixel array is depicted in Figure 2.8 and also shown is the uniformly distributed incidence points. The origin is defined at the center of the pixel array and the coordinates of the center pixel is thus (n+1, n+1). Obviously, the center of the pixel array overlaps the center of the center diode and pixel. n has to be large enough to accommodate all the electrons even after a large number of random-walk steps in the Monte Carlo simulation. x-y plane is defined as the top surface of the pixel array and the negative z-axis goes into the silicon body, as shown in Figure 2.9.

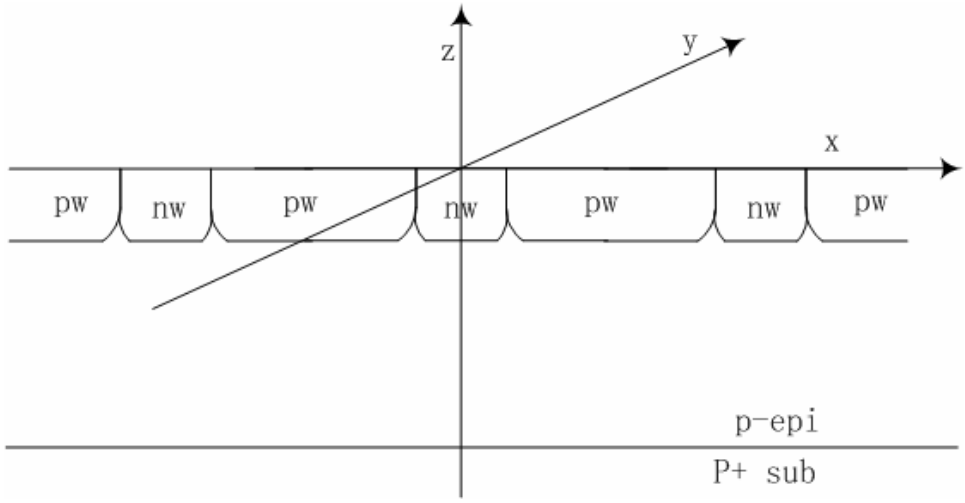

Figure 2.9: Conceptual view of the modeling system.

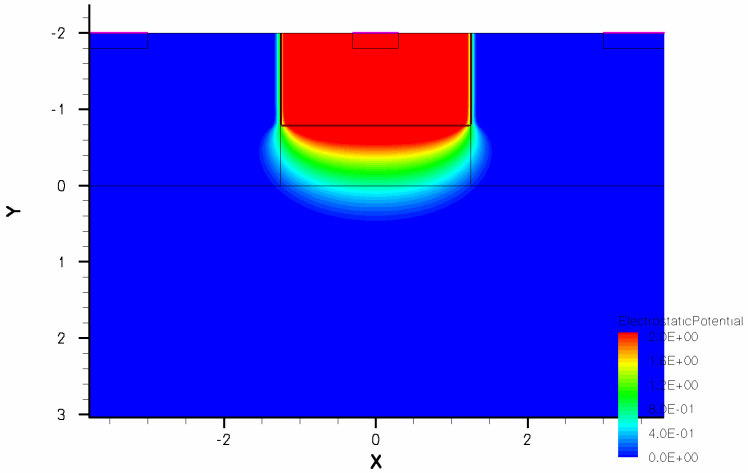

Figure 2.10: Finite element analysis of the distribution of the electric potential in a pixel.

Note that the electrical boundaries have to be properly added to the physical boundaries in the simulation. And an ISE-TCAD simulation of the cross-sectional view of the electric potential distribution in a pixel is shown in Figure 2.10. The detailed Monte Carlo algorithm implemented in matrix language is given as follows.

(1) Generate an array of ionization electrons characterized by initial coordinate matrix

$$\begin{pmatrix} X \\ Y \\ Z \end{pmatrix}_{k,0} = \begin{pmatrix} x_{1,0} & x_{2,0} & \cdots & x_{k,0} \\ y_{1,0} & y_{2,0} & \cdots & y_{k,0} \\ z_{1,0} & z_{2,0} & \cdots & z_{k,0} \end{pmatrix} \tag{2.52}$$

The number of ionization electrons (k) generated and the initial coordinates are determined by ionization generation.

(2) Examine the carrier position with respect to the collection region. If in, count the carrier as collected, take them off from the coordinate matrix and reshape

$$\begin{pmatrix} X \\ Y \\ Z \end{pmatrix}_{k,0} \xrightarrow{collection} \begin{pmatrix} X \\ Y \\ Z \end{pmatrix}_{k-nr_0,0} \tag{2.53}$$

and submit the new matrix for random-walk. In Equation 2.53, nr_0 stands for the number of ionization electrons that have been collected and are taken off from the carrier array that will undergo additional random-walk.

(3) Allow an increment in time and the corresponding displacement is calculated using Equation 2.47.

$$\begin{pmatrix} \Delta X \\ \Delta Y \\ \Delta Z \end{pmatrix}_{k-nr_0,0} = \begin{pmatrix} \Delta x_{1,0} & \Delta x_{2,0} & \cdots & \Delta x_{k-nr_0,0} \\ \Delta y_{1,0} & \Delta y_{2,0} & \cdots & \Delta y_{k-nr_0,0} \\ \Delta z_{1,0} & \Delta z_{2,0} & \cdots & \Delta z_{k-nr_0,0} \end{pmatrix} \tag{2.54}$$

and the new coordinates are then given by

$$\begin{pmatrix} X \\ Y \\ Z \end{pmatrix}_{k-nr_0,1} = \begin{pmatrix} X \\ Y \\ Z \end{pmatrix}_{k-nr_0,0} + \begin{pmatrix} \Delta X \\ \Delta Y \\ \Delta Z \end{pmatrix}_{k-nr_0,1} \tag{2.55}$$

(4) Examine electrons that have recombined and disappeared. As the probability for an electron to recombine in a given period of time is determined from Equation 2.48, an array of random numbers following uniform distribution within [0, 1] is used to map those recombined electrons. First, generate an array of uniform random numbers within [0,1]:

$$(RR)_{k-nr_0,1} = (rr_{1,1} \quad rr_{2,1} \quad \cdots \quad rr_{k-nr_0,1}) \tag{2.56}$$

The first subscript in $rr_{i,1}$ uniquely matched to the ith electron in the electron array. If $rr_{i,1}$ is no greater than the recombination probability, then the ith electron is considered to undergo recombination and is then taken off from the electron array. Only those electrons matched by $rr_{i,1}$ are kept for subsequent calculation. The number of electrons in the array decreases one more time,

$$\begin{pmatrix} X \\ Y \\ Z \end{pmatrix}_{k-nr_0,1} \xrightarrow{recombination} \begin{pmatrix} X \\ Y \\ Z \end{pmatrix}_{k-nr_0-mr_1,1} \tag{2.57}$$

where mr_1 stands for the number of electrons vanish due to recombination during the first random-walk.

(5) Examine electron position with respect to the active collection region. If in, count the carrier as collected, take them off from the coordinate matrix and reshape

$$\begin{pmatrix} X \\ Y \\ Z \end{pmatrix}_{k-nr_0-mr_1,1} \xrightarrow{collection} \begin{pmatrix} X \\ Y \\ Z \end{pmatrix}_{k-nr_0-mr_1-nr_1,1} \tag{2.58}$$

where nr_1 stands for the number of electrons collected after the first random-walk. And the new electron array is submitted for boundary conditions.

(6) Examine the carrier position with respect to the boundaries. If any of them has crossed the reflective boundaries, reflect the carrier position with respect to the boundary.

(7) Loop to step (3) until the coordinate matrix $\begin{pmatrix} X \\ Y \\ Z \end{pmatrix}$ shrinks to zero or until a certain number of random-walk steps (which translates into a certain integration time) has been reached.

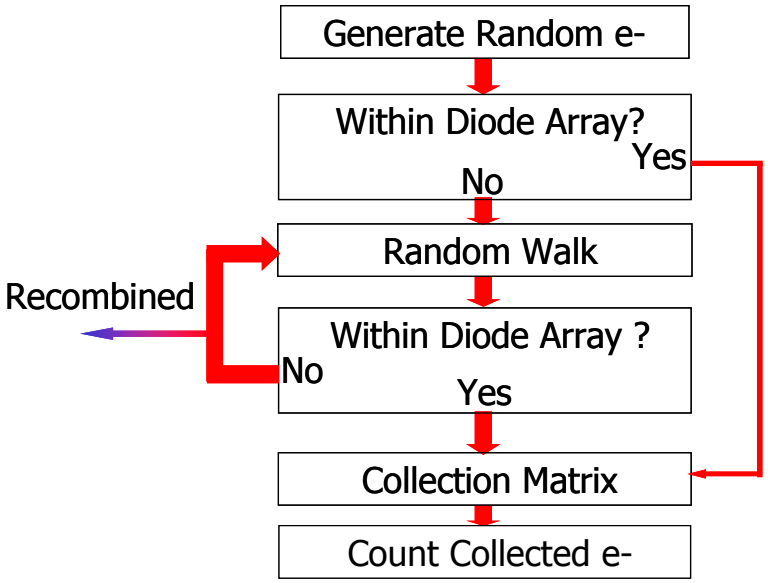

Figure 2.11: Monte Carlo model flow chart.

This process is shown as the Monte Carlo flow chart in Figure 2.11. The algorithm for electrons in p-substrate is similar to that of in p-epi. The only difference lies in the boundary conditions. First, the p-substrate/p-epi boundary is transparent for electrons in p-substrate. Electrons cross such a boundary are not reflected and they become p-epi electrons. Second, both experimental measurement and simulation indicate that electrons generated very deep in the silicon have negligible effect on the collection matrix due to recombination and lateral diffusion. A computationally convenient depth is usually selected as a total absorption boundary where electrons crossing it will not be counted anymore. This topic will be treated systematically in Chapter 4 and Chapter 5. This algorithm is first implemented in Matlab and then transformed into C++ programming language. Matrices accounting for the collection from tens of thousands of random incident particles need to be simulated.

2.7 Summary

A Monte Carlo model based on first principles has been developed following Einstein's formulism of Brownian motion. Charged-particle detection and imaging using APS is assumed to be a two-step process: 1) the generation of ionization electrons due to impinging particle and silicon interaction, 2) charge transport within silicon. Ionization generation due to ^{55}Fe 5.9 keV X-ray and high energy electrons are modeled directly using random numbers following exponential distribution and Bichsel distribution, respectively. Diffusion equation with recombination term is solved by Fourier's transform method. The general solution comprises of the product of an exponential decay term and a diffusion term and the recombination rate and random-walk step size are then

derived. After formalizing the boundary conditions in from the perspective of individual electron movement, a Monte Carlo algorithm with flow chart in matrix language is then presented.

CHAPTER 3: PROTOTYPE CHARGED-PARTICLE IMAGI SENSOR DESIGN AND TESTING SETUP

Experimental measurements on real devices are necessary to test and fine-tune the Monte Carlo model and provide clues on how to optimize sensor performance. This chapter presents the architecture and design of three generations of prototype chips and testing setup for charged-particle detection and imaging.

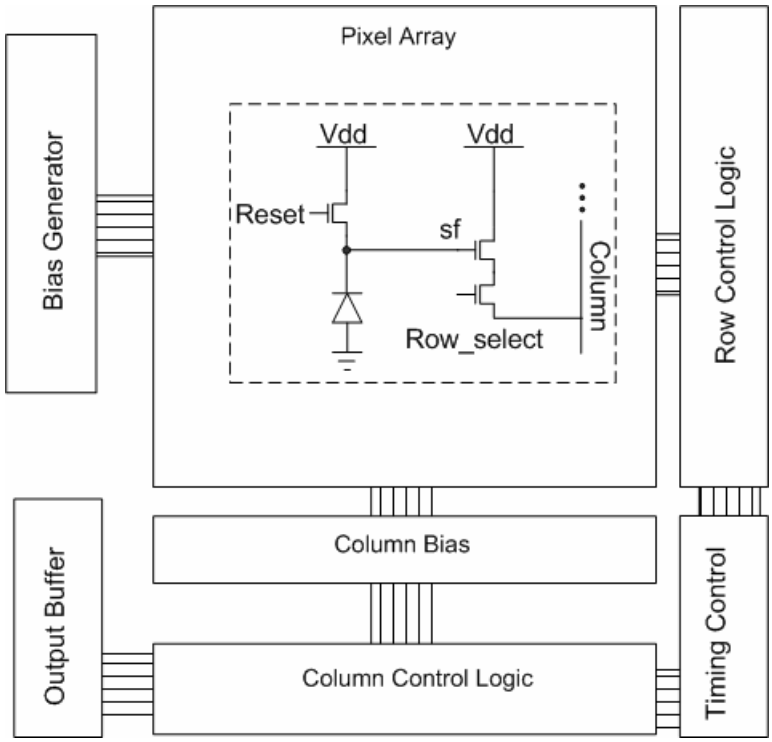

Figure 3.1: The basic architecture of a simple APS array for digital imaging.

The most important design parameters on the pixel level are diode size and pixel pitch. Both parameters should be fine-tuned to optimize signal-to-noise ratio and spatial

resolution. There are also other parameters usually beyond a designer's control such as the recombination rate, epitaxial silicon thickness, doping density, trap and defect density, etc. Experimental devices focusing on the diode size and pixel will lead to insightful understanding of the effects of these parameters that are less tangible. With that said, three generations of prototype chips with the simplest APS architecture are presented in this chapter. The design of more sophisticated circuitry will be presented in Chapter 6.

Figure 3.1 shows the basic architecture of an APS array for digital imaging. The core is a pixel array consisting of electron-sensitive elements (e.g. photodiode), a reset transistor and a source follower buffer for charge-to-voltage conversion, and a row select switch. The timing control block generates internal signals for the operation of the pixel sensor. The bias generator controls the bias current and distributes them to the pixel array and peripheral circuits. The output buffer provides an interface to probe the signals corresponding to each pixel. The prototypes discussed in this chapter all adopts this architecture and mainly differentiate in device dimensions at the pixel level.

3.1 EM1 – A Diode Area Test Chip

To explore the influence of diode size on signal-to-noise ratio, an experimental device containing sectors of pixels with different collection diode areas was designed and tested. The chip was fabricated using a 0.5 mm CMOS process that includes a ~ 10 μm epitaxial silicon layer. The block diagram is shown in Figure 3.2. The pixel arrays consist of five

sectors, with 50 × 50 pixels each with a 20 μm pixel pitch. The only difference between different sectors is the area of the diodes in the pixels, ranging from 13 to 54 μm^2.

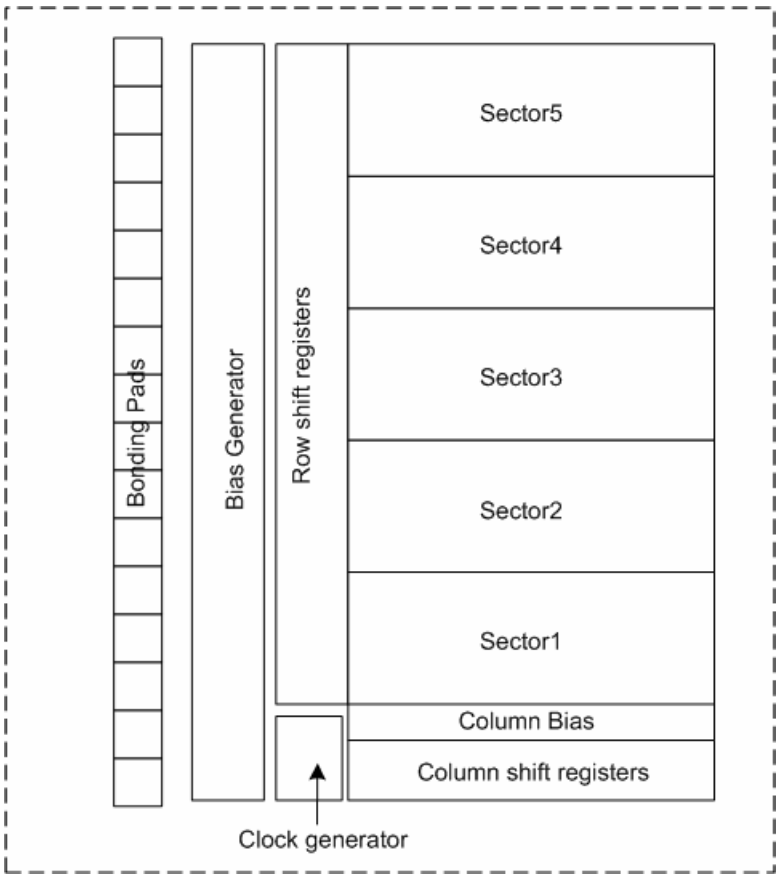

Figure 3.2: EM1 block diagram.

The signal path of EM1 is illustrated in Figure 3.3. Ionization electrons are generated by the interaction between impinging high energy particles and silicon. Many of them are collected by the reversely biased n-well/p-epi diodes. The electron signal is then converted into voltage signal by the source follower transistor and subsequently readout through the row select switch. Each column line is biased by a current mirrored through a

large transistor. The signal from each column is then multiplexed to the shared output buffer, which is a simple source follower in this case.

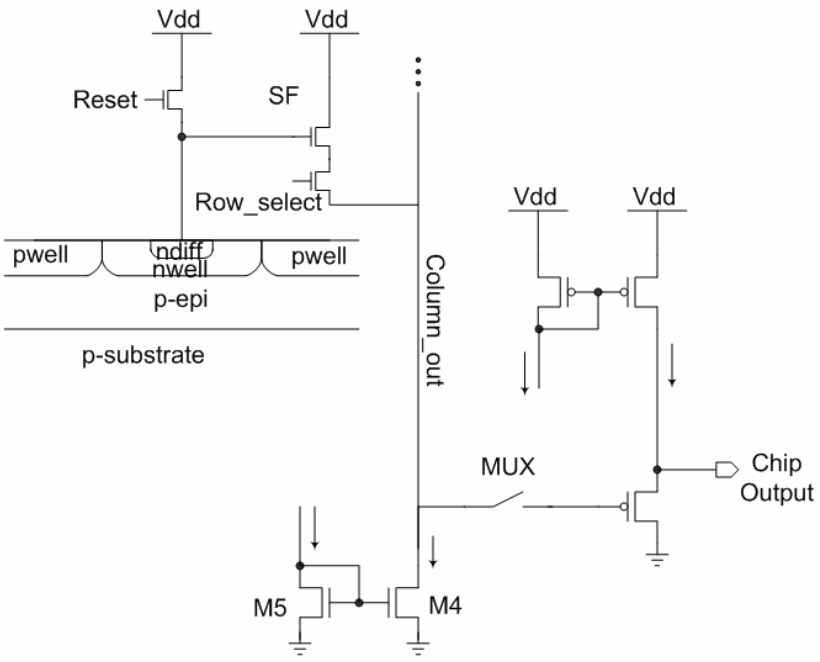

Figure 3.3: EM1 signal path.

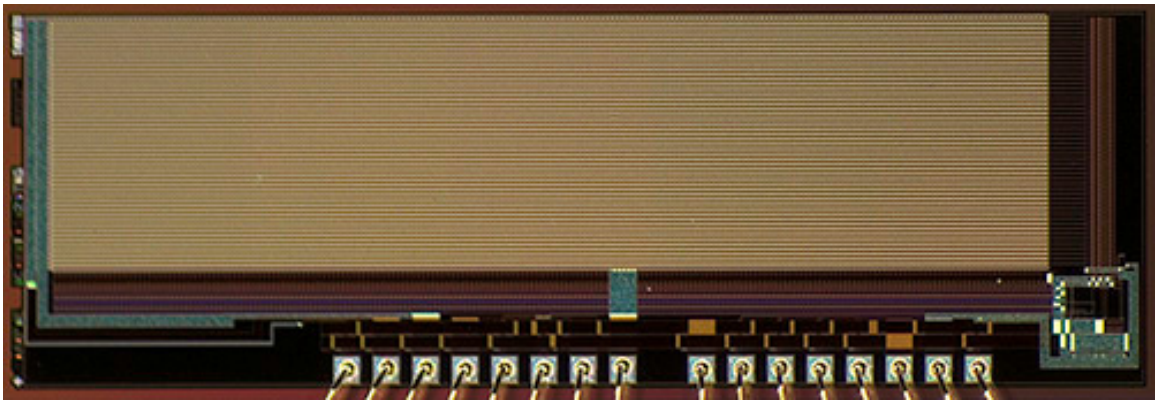

Figure 3.4: EM1 Die Micrograph.

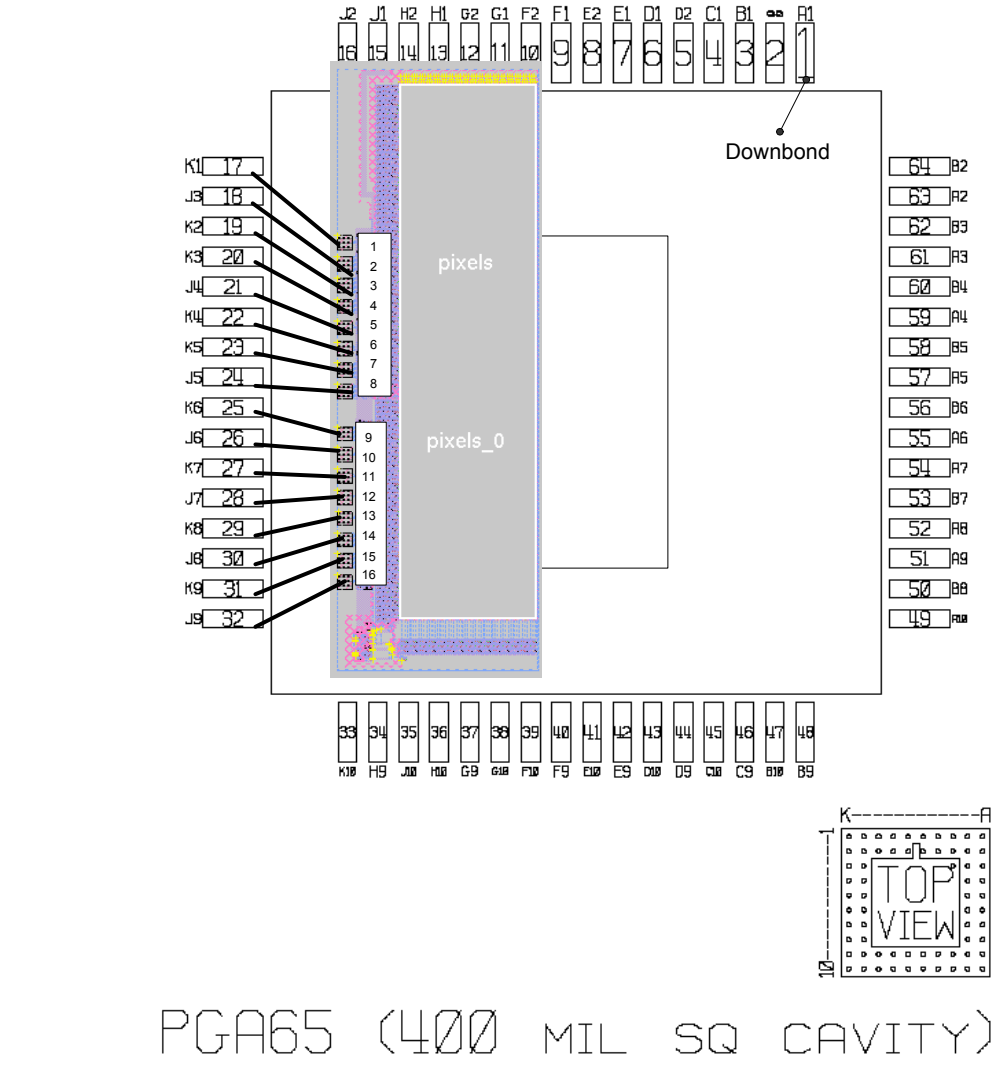

Figure 3.5: EM1Bonding Diagram.

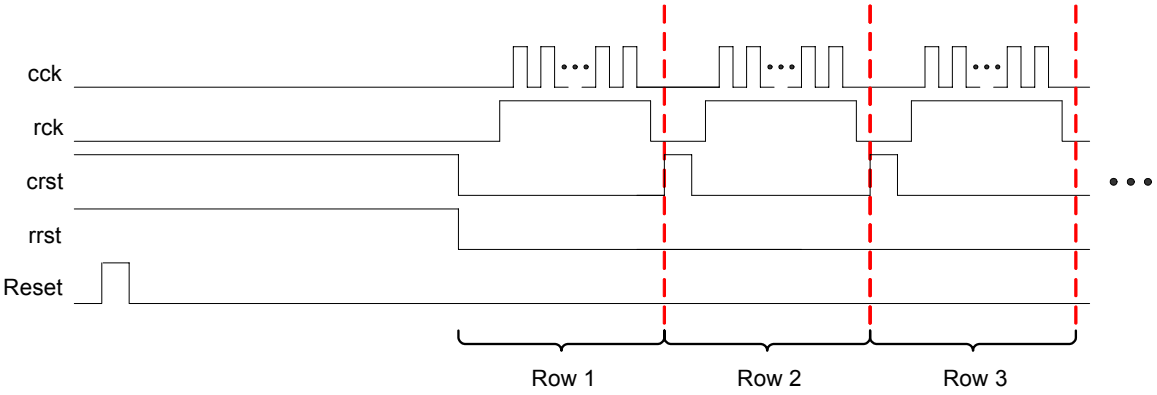

Figure 3.6: EM1 Timing Diagram.

Figure 3.4 shows the die photo of EM1. It was packaged using a standard PGA65 ceramic package, as shown in Figure 3.5. Because the number of pixels in this test chip is small, simple global reset and subsequent readout pixel by pixel is adequate. A typical timing diagram for this chip is shown in Figure 3.6. The simplicity of this chip allows us to measure the effect diode size on collection efficiency and signal-to-noise ratio.

3.2 EM2 – A Pixel Pitch Test Chip

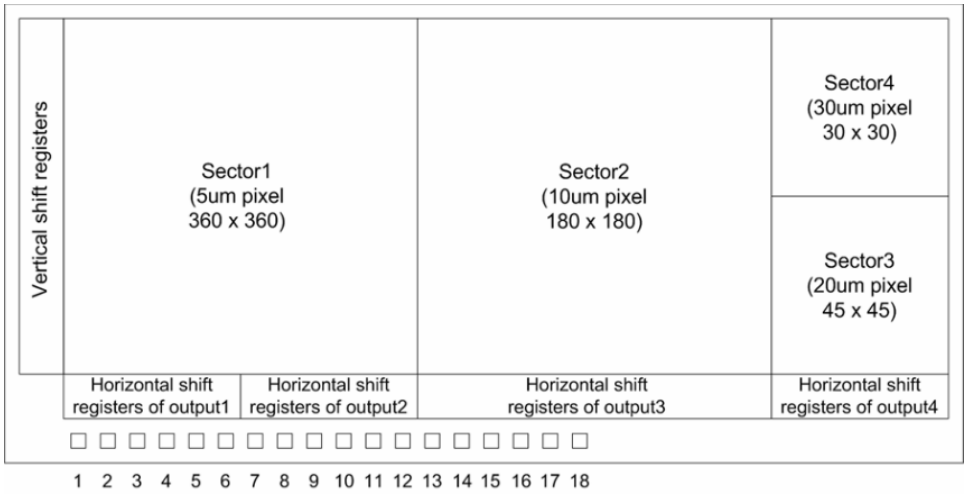

Figure 3.7: EM2 block diagram[§].

In order to systematically evaluate the effect of lateral diffusion, an experimental device (EM2) with different pixel pitch values but identical diode size were also designed. This chip was fabricated using a 0.25 μm CMOS process that includes a ~ 8 μm epitaxial silicon layer. Each pixel has an identical, minimum-sized, photodiodes of 1.8 μm by 1.8 μm as drawn, and identical readout circuit geometry as shown in Figure 3.7. Therefore the sensitivity, noise, capacitance and the charge to voltage conversion ratio of every

[§] Designed by Yandong Chen.

pixel is as identical as possible. The array is organized in 4 sectors with different pixel pitches. Sector 1 has 360 by 360 pixels with 5µm pitch – the highest density in this test. Sector 2 has 180 by 180 pixels with 10 µm pitch, Sector 3 has 45 by 45 20-µm pitch pixels, and Sector 4 has 30 by 30 pixels with 30 µm pitch. The die photo is shown in Figure 3.8 and this chip was also packaged using standard PGA65 ceramic package.

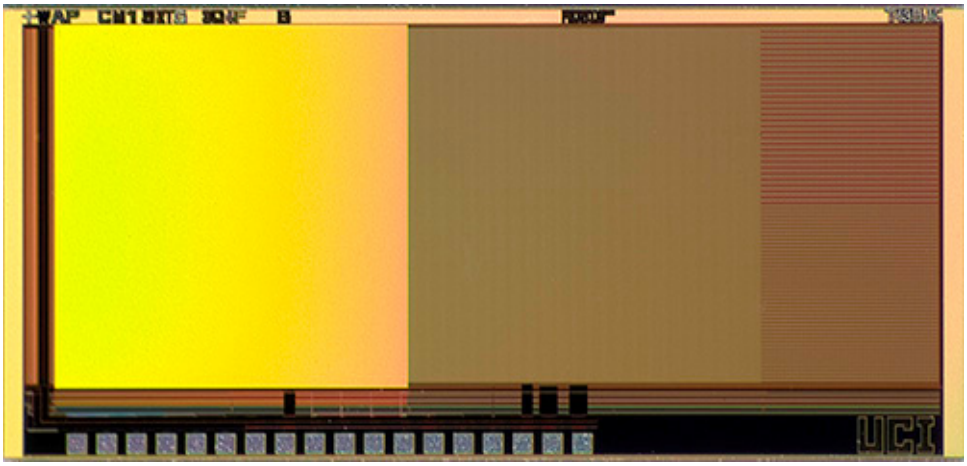

Figure 3.8: EM2 Die Micrograph.

3.3 EM3 – A 550 × 512 Pixel Test Chip

Initial testing on EM1 and EM2 using X-ray photons and electron beam was very successful and a prototype camera chip consisting of a 512 × 550 pixel array was then designed and fabricated. This is the first full-scale electron camera based on which high resolution images of biological samples were successfully obtained. The pixel pitch is 5 µm × 5 µm and the diode is 2.5 µm × 2.5 µm, built upon 8 µm epitaxial silicon. Read-out is fully independent of resets, thereby permitting multiple reads per reset and hence true correlated double sampling (CDS) is possible with the use of off-chip frame storage and subtraction.

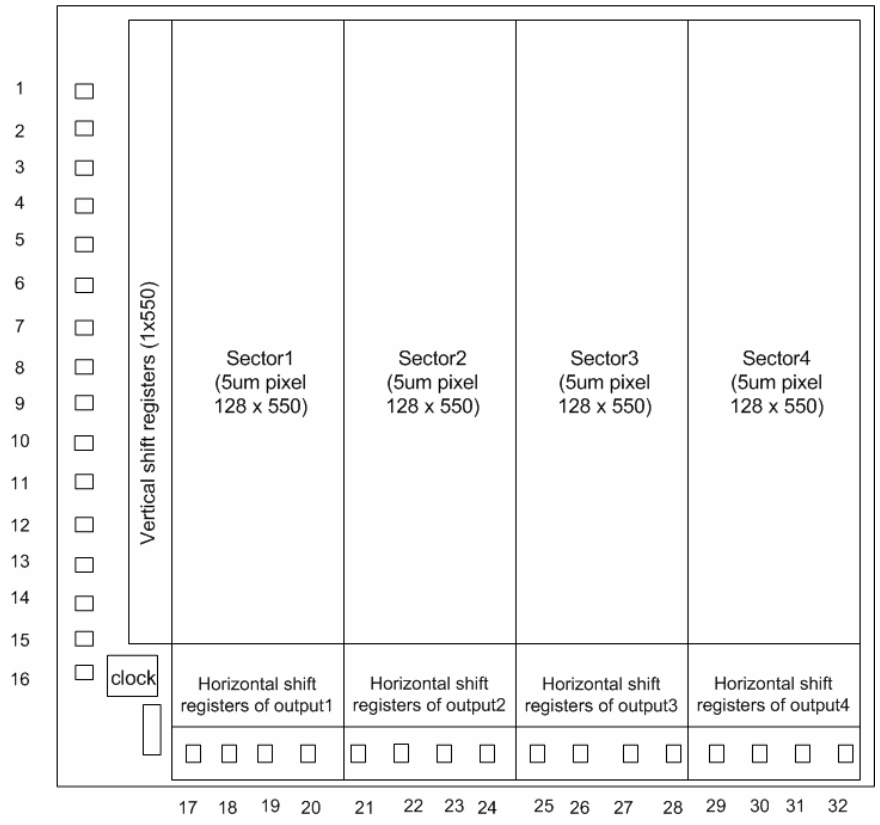

Figure 3.9: EM3 block diagram.

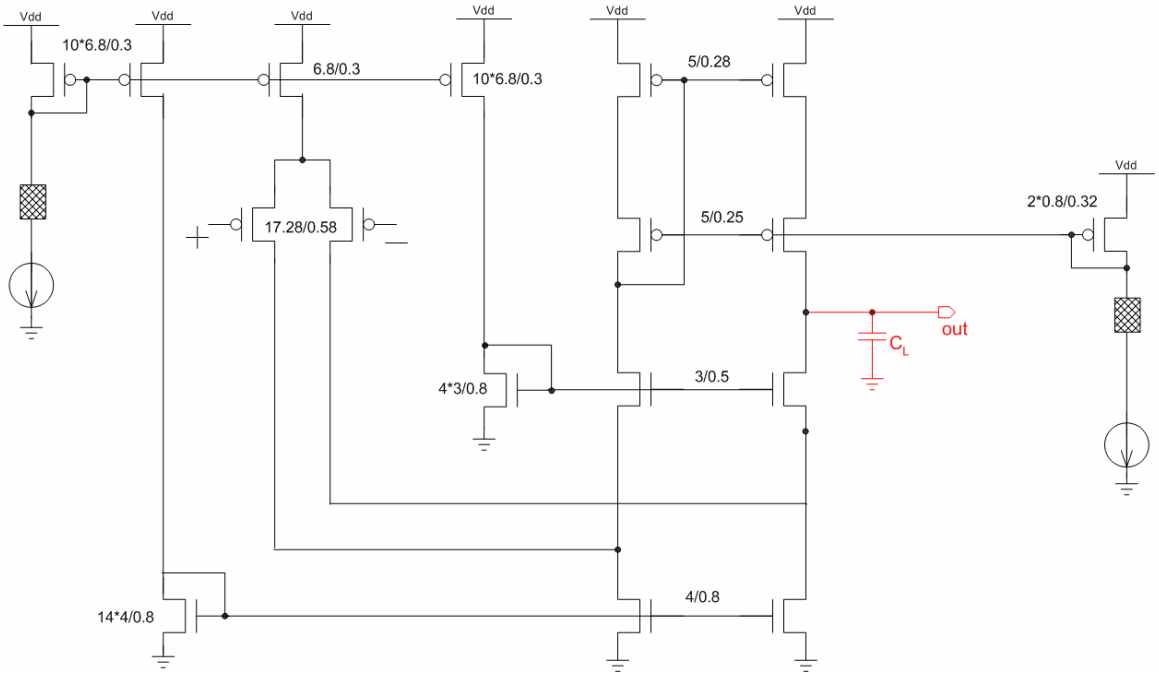

Figure 3.10: EM3 output buffer schematic.

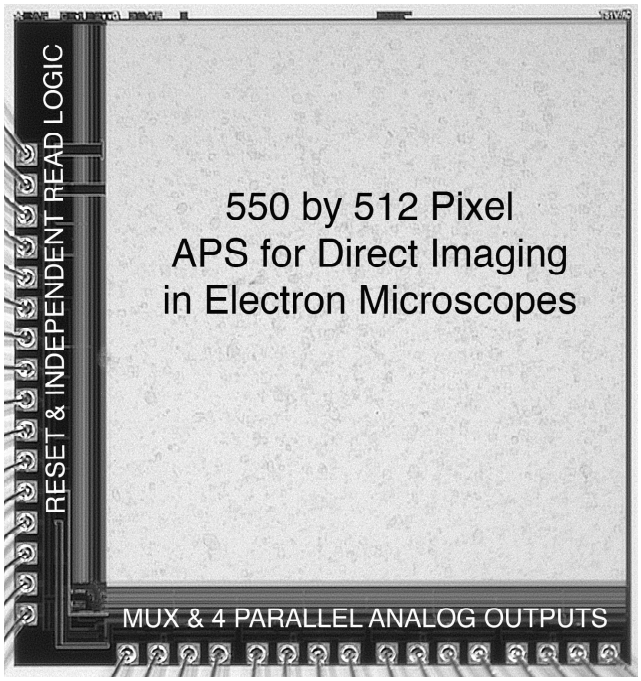

Figure 3.11: Die photo of EM3 -- the first direct electron camera.

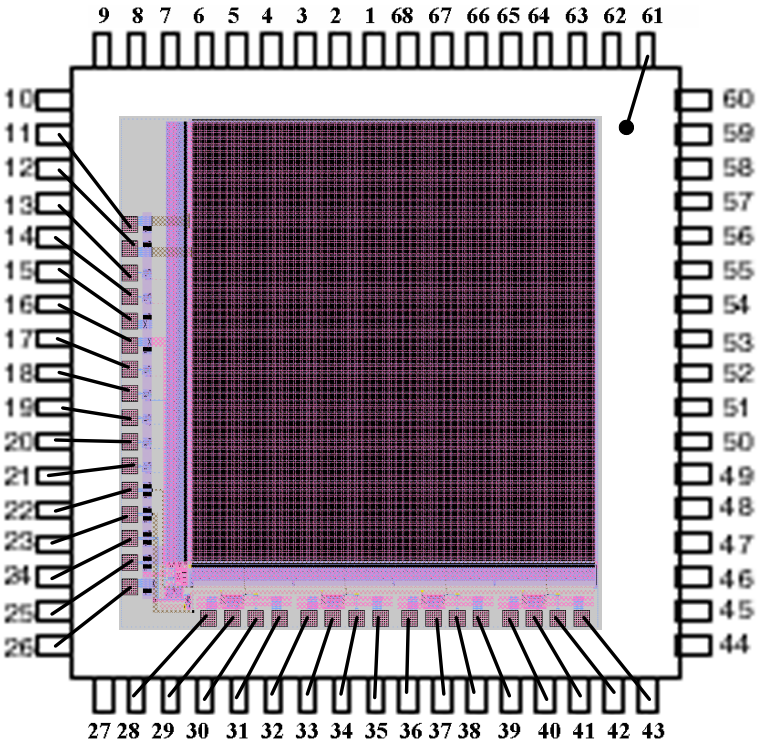

Figure 3.12: EM3 bonding diagram, in PLCC 68.

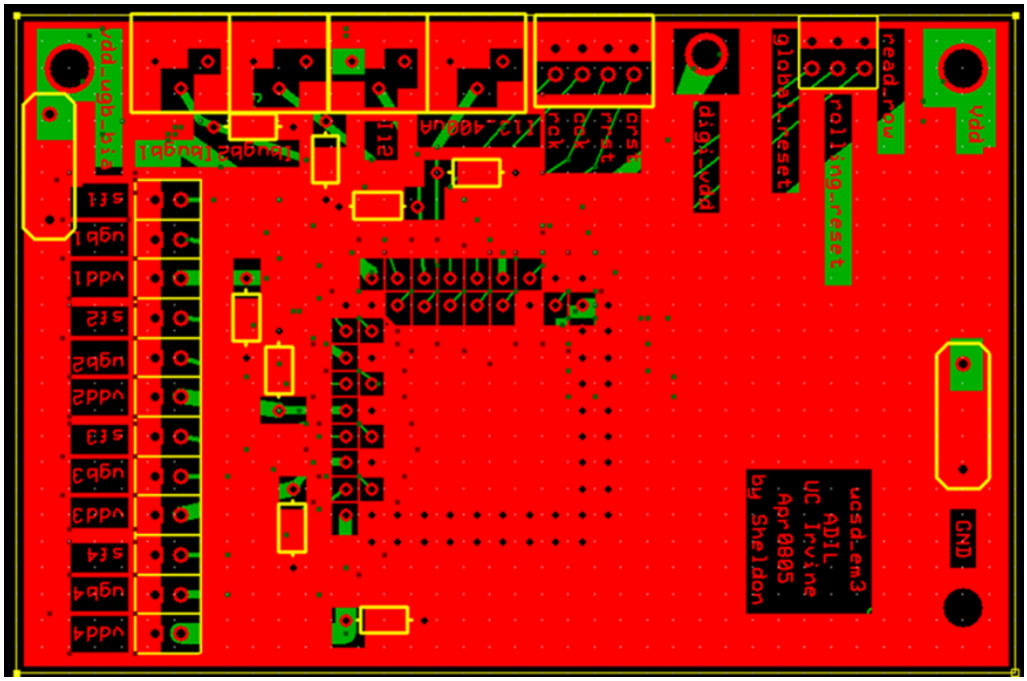

Figure 3.13: PCB board design for EM3 testing.

Four parallel analog outputs were designed to increase the data output rate. The analog output buffer adopts folded cascade op amp architecture, as depicted in Figure 3.10. The basic idea behind this architecture is to convert input voltage into a current and then apply the current to a common-gate stage with cascode load. The input PMOS transistors and the common-gate NMOS transistors are connected in cascode configuration as well. PMOS-NMOS cascode allows larger input range than a NMOS-NMOS cascode usually implemented a telescope amplifier. The small-signal current from the drain of the input PMOS is folded up into the source of the common-gate NMOS, yielding the name "folded cascode". The wide-swing cascode load for the common-gate is to increase the output resistance and achieve high gain. This architecture is advantageous to be implemented in CMOS technology and it has better input common-mode input range and power supply rejection than a typical two-stage op amp [51].

The die photo of EM3 is shown in Figure 3.11. It was mounted onto a standard PLCC 68-pin chip carrier. The bonding diagram is shown in Figure 3.12 and the design of the PCB board is depicted in Figure 3.13.

3.4 Testing Setup

The prototype chips designed for charged-particle imaging have to undergo two different types of tests. The first is the conventional electrical testing performed in our electronics lab at UC Irvine. The second is to the test the sensor response to high energy particles such as x-ray photons and high energy electrons. These tests involve radiation materials, electron microscope, and particle accelerator, which are not readily available and have to be performed in the National Center for Microscopy and Imaging Research (NCMIR) and Lawrence Berkeley National Laboratory.

3.4.1 Visible Light Testing

Bench test is simple and the test instruments used are listed in Appendix A.

3.4.2 X-ray Photon Testing

^{55}Fe x-ray testing has been a standard method for precise measurements of charge transfer efficiency for charge coupled devices. ^{55}Fe emits x-ray at three energies and the emission is caused by the inner electron of the ^{55}Fe isotope being captured by the nucleus, transforming it into Manganese. By far the most intense of these emissions is at 5.9 keV (the so called Mn K_α line), but there are weaker peaks at 6.49 keV (Mn K_β) and 4.12 keV

(K_α escape). Most of the charge that is generated is shared between several pixels; commonly called split events in CCD calibration. A very small percentage is collected by a single pixel occasionally. The single pixel events are the basis for calibrating the gain of various image sensors.

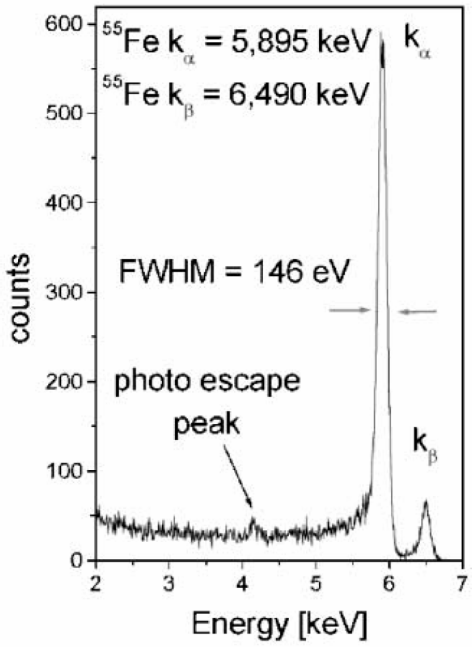

Figure 3.14: ^{55}Fe X-ray spectrum measured with a silicon device at room temperature [52].

3.4.3 Electron Microscopy Testing

Several electron microscopes at NCMIR were used for testing including a JEM-2000 FX II and JEM-4000 EX. The sensor chip was first mounted onto a customized PCB board and then placed into a modified JEOL TEM film cassette, which is a standard add-on for any electron microscope.

(a)

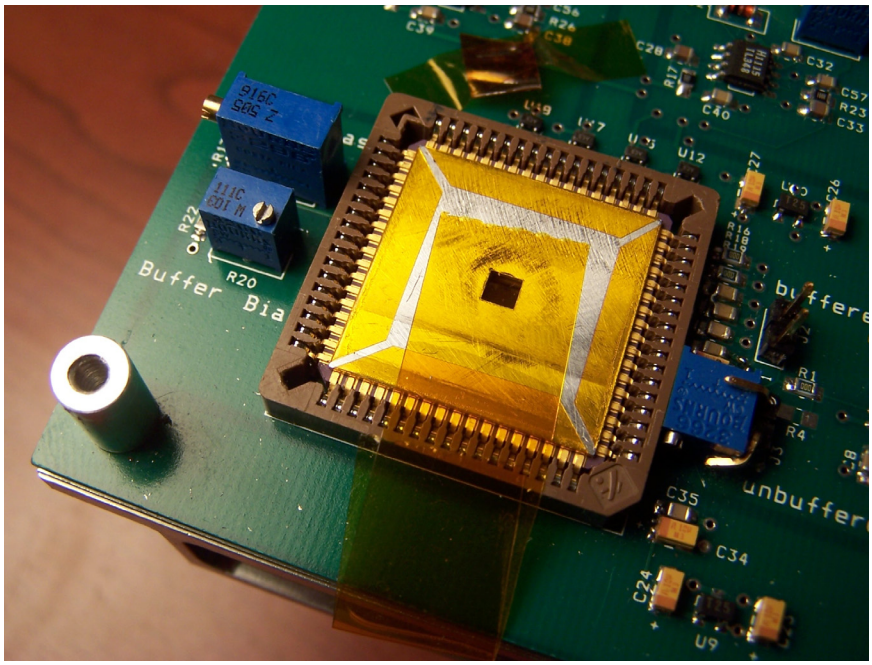

(b)

Figure 3.15: EM chip mounted onto a customized PCB board. (a) EM Chip and PCB board overview, (b) EM on board, zoom-in view.

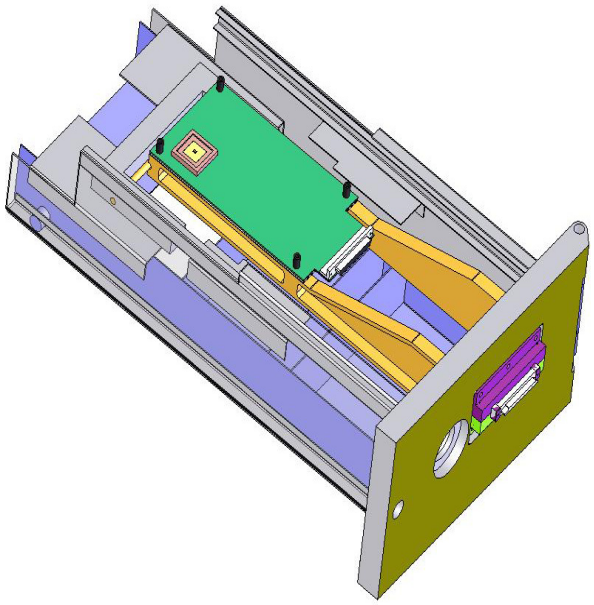

Figure 3.16: Conceptual view of a standard TEM film cassette with EM chip mounted.

An important issue for testing under electron microscope is the thermal management. The heat generated by the sensor array and the supporting PCB board has to be properly managed in the extremely high vacuum environment inside electron microscope. In addition, cooling the device to a lower temperature improve radiation tolerance. The heat sink used in the experiment is a Peltier thermo-electric cooler that works based on the he Peltier–Seebeck effect, or thermoelectric effect (the direct conversion of thermal differentials to electric voltage and vice versa). The testing under electron microscopy and using X-ray photons are in collaboration with Dr. Nguyen-huu Xuong's group at UCSD and Dr. Howard Matis at Lawrence Berkeley National Laboratory.

3.5 Summary

The basic architecture and design of three test chips have been presented. These prototype chips are tested using visible light, X-ray, and high energy electrons in electron microscopy. The testing setup is briefly presented.

CHAPTER 4: X-RAY PHOTON RESPONSE

4.1 Simulation Setup

X-ray photons are assumed to impinge on the center pixel (n+1, n+1) following a uniform random distribution in x-y plane and an exponential absorption along the depth of the silicon. With much higher energy, X-ray photons can excite tightly bounded electrons in silicon. At room temperature, the most probable energy required to generate one electron-hole pair is 3.6 eV [52], resulting in ~1639 ionization electrons per photon. In the simulation, the ionization energy is represented as a Gaussian random number with 3.6 eV as the mean and 0.04 eV as the standard deviation[53]. Therefore, the number of ionization electrons generated per incident photon is also random,

$$n_e = \frac{5.9keV}{(3.6 + 0.04 \cdot randn)eV/e} \tag{4.1}$$

where *randn* is a random number following normal distribution with zero mean and standard deviation equal to one. Ionization electrons generated by an x-ray photon tends to distribute in a sphere centered at the point of ionization and the standard deviation of the radius of the ionization sphere is given as [37, 54]:

$$R(\mu m) = 40.8 \times 10^{-3} \cdot E_e^{3/2} \tag{4.2}$$

where E_e is the energy of the impinging photon in keV and R is the radius of the spherical distribution of the ionization electrons. For ^{55}Fe 5.9 keV X-ray, R is ~0.58 μm. Consequently, ~61% of ionization electrons are initially distributed less than 0.5 μm away from the point of absorption, and more than 90% are distributed within 1 μm. A combination of the exponential distribution and Gaussian distribution yields the initial

coordinates of ionization electrons that can be subject to a random-walk in a Monte Carlo framework, that is,

$$\begin{pmatrix} x_{x,0} \\ y_{x,0} \\ z_{x,0} \end{pmatrix} = \begin{pmatrix} n \cdot pitch \\ n \cdot pitch \\ 0 \end{pmatrix} + \begin{pmatrix} randu \cdot pitch \\ randu \cdot pitch \\ \lambda_x \cdot \log_e(randu) \end{pmatrix} + r \cdot \begin{pmatrix} \sin(\theta)\cos(\varphi) \\ \sin(\theta)\sin(\varphi) \\ \cos(\theta) \end{pmatrix} \quad (4.3)$$

where (x_{x0}, y_{x0}, z_{x0}) is the starting point of an ionization electron and r, θ, and φ are given by

$$\begin{pmatrix} r \\ \theta \\ \varphi \end{pmatrix} = \begin{pmatrix} R \cdot randn \\ 180 \cdot randu \\ 360 \cdot randu \end{pmatrix} \quad (4.4)$$

Submitting all the ionization electrons generated every incident X-ray photon to the Monte Carlo procedure discussed in Chapter 2, matrices accounting for the collection from tens of thousands of random incident photons were simulated and analyzed.

4.2 Typical Response to Individual X-ray Photons

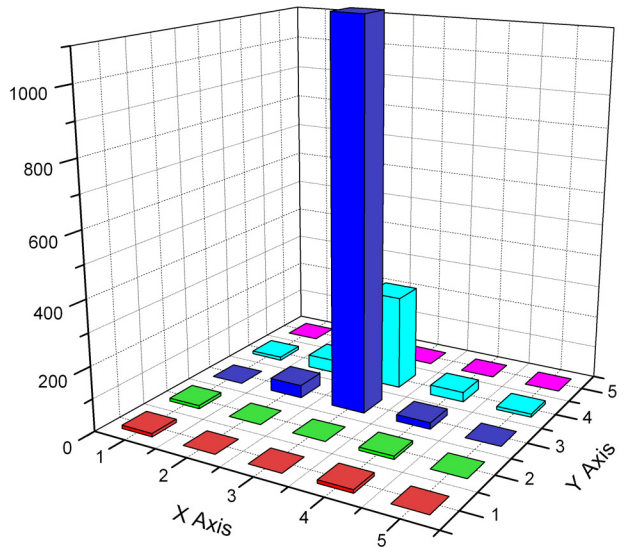

(a)

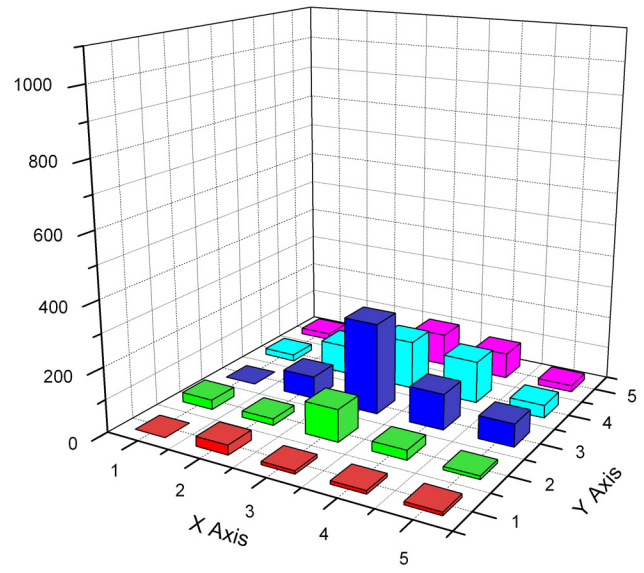

(b)

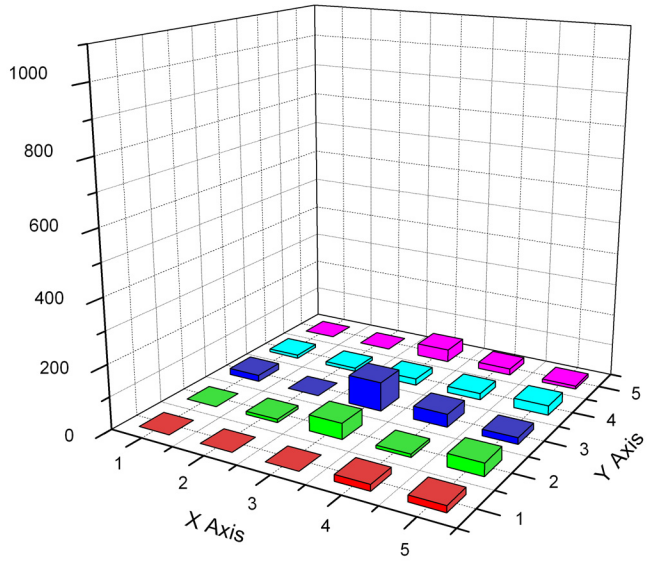

(c)

Figure 4.1: Typical collection profiles for individual x-ray photons under conditions in which: (a) The absorption occurs close to the top surface of epitaxial layer and in the vicinity of a collection diode, (b) The absorption occurs near the bottom surface of the epitaxial layer, and (c) The absorption occurs close to the top surface in the bulk silicon. Diode size: 1.8 μm, pixel pitch: 5 μm.

We first present typical collection matrices corresponding to individual x-ray events in Figure 4.1. Figure 4.1 (a) illustrates the collection matrix simulated for a single X-ray

absorbed near the top of the p-epi layer (randomly positioned horizontally within the pixel), very close to the depletion region of the collection diode in the center pixel. In this case, most of the ionization electrons (~1639 e^-) are collected by the center pixel. Ionization electrons collected outside a 3 by 3 pixel array is insignificant. The number of electrons that diffuse to neighboring pixels is very small and electron loss due to recombination is negligible. By contrast, the collection matrix corresponding to an x-ray photon absorbed near the bottom surface of the p-epi layer, as shown in Figure 4.1 (b), shows considerable lateral diffusion. While the center pixel collects most of the ionization electrons, more than 50% of them diffuse to neighboring pixels. Intuitively, ionization electrons generated deep in silicon have to travel a longer distance to reach a collection diode, and in the process many of them migrate to neighboring pixels, most significantly over a 5 by 5 pixel array. The simulation also indicates that some of these ionization electrons recombine before reaching a collection diode.

Lateral diffusion and recombination becomes worse for X-rays absorbed in the bulk silicon substrate. Figure 4.1 (c) depicts the collection matrix for such a substrate X-ray event. As the recombination rate in the more heavily doped p-substrate is much greater than that in the p-epi region. Nearly 70 % of the ionization electrons generated recombine before entering the epitaxial layer. By the time electrons do cross the p-substrate/p-epi boundary and enter into p-epi region, lateral diffusion is pronounced. Many X-ray absorption events that occur deep in the substrate do not produce significant collection of ionization electrons at all.

4.3 Lateral Diffusion and Recombination

The depth of ionization affects these collection profiles in both the total number of ionization electrons collected and the relative distribution of collected electrons. To address both issues, we show a scatter plot of collected ionization electrons vs. absorption depth in Figure 4.2. Two scatters are shown, one of the peak (center) pixel only and one of a 5 by 5 array of pixels. Those of the 5 by 5 pixel array are the sum of all 25 pixels centered on the peak pixel.

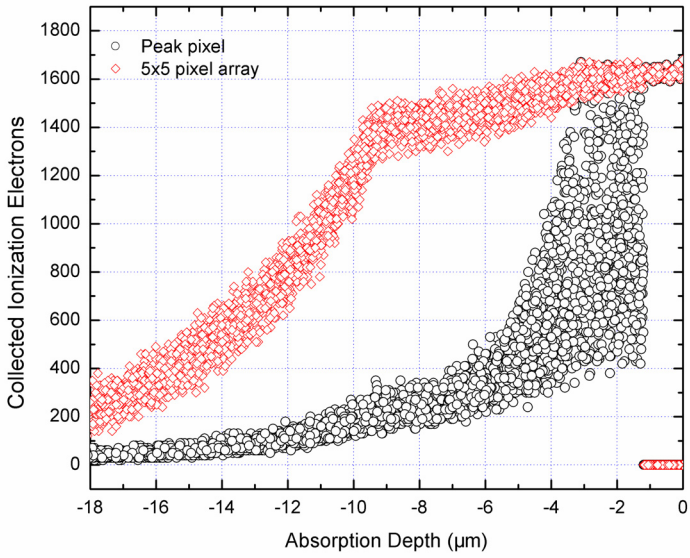

Figure 4.2: Scatter plot of electrons collected for the peak pixel and 5 by 5 array centered on the peak pixel (^{55}Fe 5.9 keV X-ray, substrate recombination rate in the substrate ("rr sub") = 0.0001, epitaxial layer thickness = 8 μm, pixel pitch = 5 μm). The top scatter is for the sum of a 5 by 5 array of pixels centered on the struck pixel. The bottom scatter is for the struck pixel only.

First we examine the case where X-ray photons are absorbed close to the top surface of the silicon chip (near 0 absorption depth, to the right in Fig. 4.2). When the absorption occurs inside the collection diode, virtually all of the ionization electrons are collected and only the central pixel has electrons in the collection matrix. This is represented as the

data points close to the right-top corner in Figure 4.2. However, when the absorption occurs in the p-well containing the readout transistors, all ionization electrons are likely to be absorbed by these low resistivity terminals and no significant value can be detected in the collection matrices. This is represented as the data points at the right-bottom corner in Figure 4.2.

Next, for X-rays absorbed in the general epitaxial silicon region (from 1 to 9 μm in Fig. 4.2), the collection of ionization electrons shows pronounced depth dependence because of lateral diffusion. Generally speaking, when the absorption occurs deeper in the epitaxial layer, the number of electrons collected by the center pixel decreases and that by the neighboring pixels increases. The electron recombination rate in the epitaxial layer is generally very small and its effect is not noticeable until the matrix summation goes up to 11 by 11 pixels (hence engendering substantial lateral diffusion) and incident photons are absorbed very close to the bottom surface of the epixtaxial layer (hence greater vertical diffusion).

Third, for X-ray events that occur in the bulk-silicon substrate, fewer ionization electrons are collected due to the greater recombination rate in the more heavily-doped substrate. As shown in Figure 4.2, for example, ionization that occurs 14 μm below the silicon surface (-14 on the vertical axis) yields few collected electrons at the center pixel. Most of the ionization electrons, if they can avoid recombination and diffuse into the epitaxial layer, are collected in neighboring pixels. This is why the data points for the 5 by 5 pixel sum are much higher than the peak pixel data points. Counting all the collected electrons

over a wider area, say up to 11 by 11 pixels, slightly raises the total number of electrons collected. But the total collected electrons remain much lower than ~1639, indicating substantial loss due to recombination.

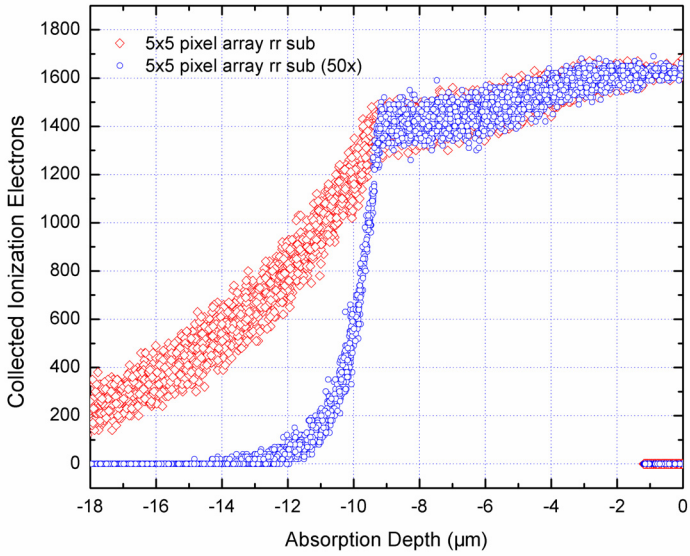

Figure 4.3: Scatter plot of electrons collected for 5 by 5 array centered on the peak pixel with different substrate recombination rate (rr sub) at 0.0001 and 0.005 for ^{55}Fe 5.9 keV X-ray photon (epitaxial layer thickness = 8 μm, pixel pitch = 5 μm). The top scatter shows a low substrate recombination rate, and the bottom scatter shows a high substrate recombination rate.

Obviously, the collection of electrons from substrate is recombination-rate dependent. A smaller bulk substrate recombination rate will make more substrate events detectable. To compare, we plotted the number of electrons collected in 5 by 5 pixel array for two different substrate recombination rates with respect to absorption depth in Figure 4.3. The circles are the data points with 50 times higher and all other conditions held identical. With a higher substrate recombination rate, the number of ionization electrons collected in the collection matrix diminishes rapidly with the increase in absorption depth.

The recombination rate of the epitaxial layer is very small, on the order of 10^{-7} according to our simulation. While increasing its value does lead to more recombination loss in the collection matrices, the effect is much less pronounced and is not shown here.

4.4 Comparison with Experimental Measurement

As the absorption depth of individual x-ray photons are difficult to measure and every collection matrix is not alike, experimental measurement often produce an average collection matrix of tens of thousands of individual collection matrices to represent the collective behavior of the collection of ionization electrons. The average collection matrices from both measurement and simulation are discussed in this section.

First, we compare the average collection matrices from both measurement and simulation for 5 μm pitch pixels in Figure 4.5 (a) and (b), respectively. On average, most of the ionization electrons are collected by the central pixel and the majority of collection occurs within a 5 by 5 pixel array. The simulation agrees very well with measurements, and the disagreement is less than 5%. Additional measurement and simulation on pixel arrays with different pitch values (10 μm, 20 μm, and 30 μm) yield similar behavior. Lateral diffusion exists for all of them.

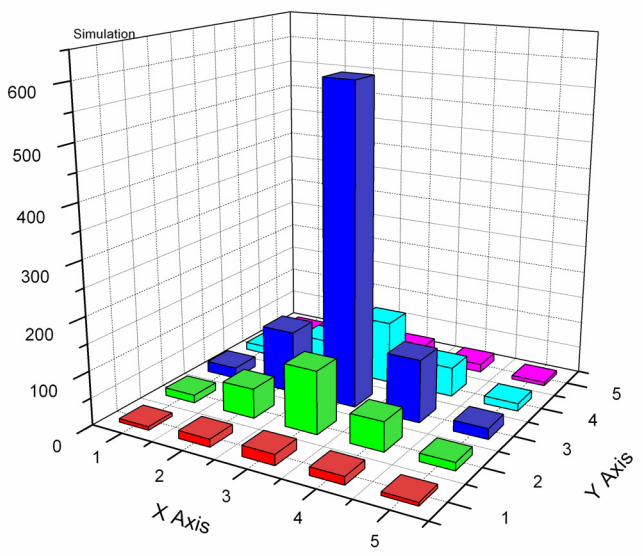

(a)

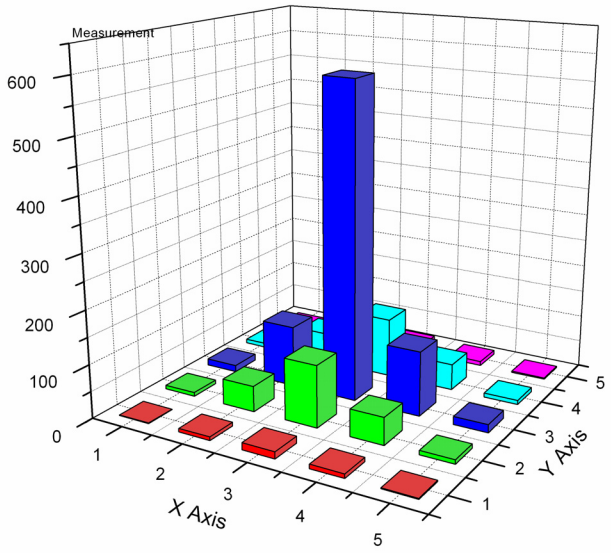

(b)

Figure 4.4: Average collection profile of ^{55}Fe 5.9 keV X-ray's: (a) Measurement, (b) Simulation. Epitaxial layer thickness = 8 µm, pixel pitch = 5 µm.

Next, we compare the collection efficiency vs. pixel cluster size the number of pixels summed) in Figure. 4.5. Data points from both measurement and simulation for all four different pixel pitch values: 5 µm, 10 µm, 20 µm, and 30 µm are shown in (a), (b), (c),

and (d), respectively. All four plots show that the total charge collected per interaction increases as the summation radius increases, indicating significant lateral diffusion. At a 5 µm pitch, the center pixel (or peak pixel) collects merely 35% of the total number of ionization electrons collected, over 90% of the 1639 electrons liberated per incident ^{55}Fe X-ray are collected within a 5×5 region of pixels, and nearly 100% is collected within a 11 by 11 region.

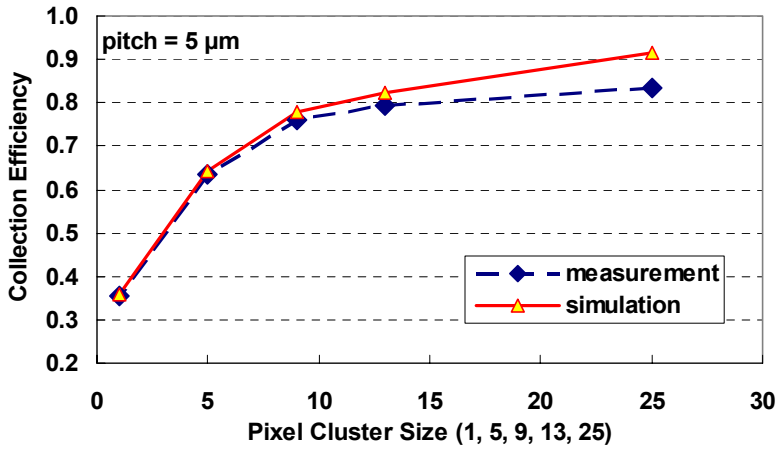

(a)

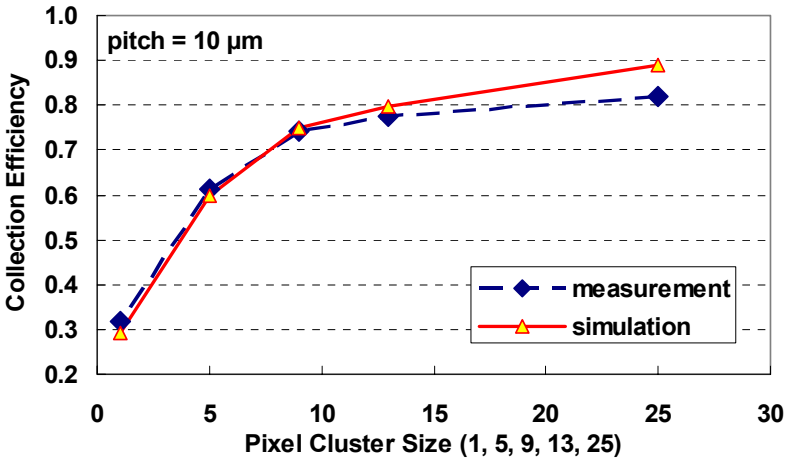

(b)

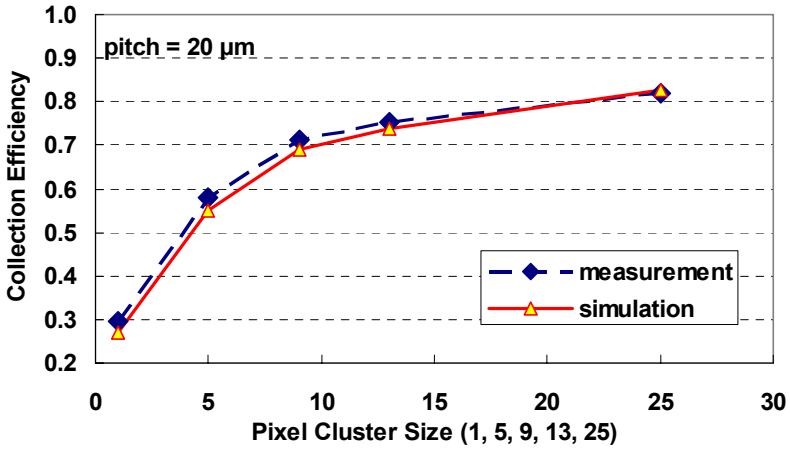

(c)

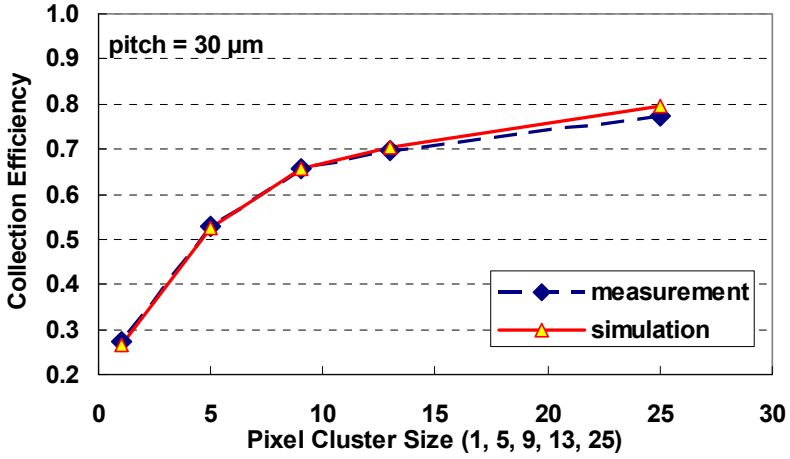

(d)

Figure 4.5: Collected charge (^{55}Fe X-rays) vs. pixel pitch and region of summed pixels (e.g., 5 by 5 pixels is a cluster of 25 pixels). Pitch: (a) 5 µm, (b) 10 µm, (c) 20 µm, (d) 30 µm.

Larger pixel pitches reduces the probability that electrons will be collected quickly, since charge necessarily diffuses further on average before being collected, and hence recombination becomes increasingly prevalent. This eventually leads to a smaller total amount of charge collected, as seen by the progressively-lower sums for the 10 to 30 µm cases in Figure 4.5. When accounting for all electrons, pixels of 5 µm pitch were found to

have about 98% charge-collection efficiency up to a 5 by 5 pixel cluster, while the 30 µm pitch resulted in about 80% efficiency due to recombination.

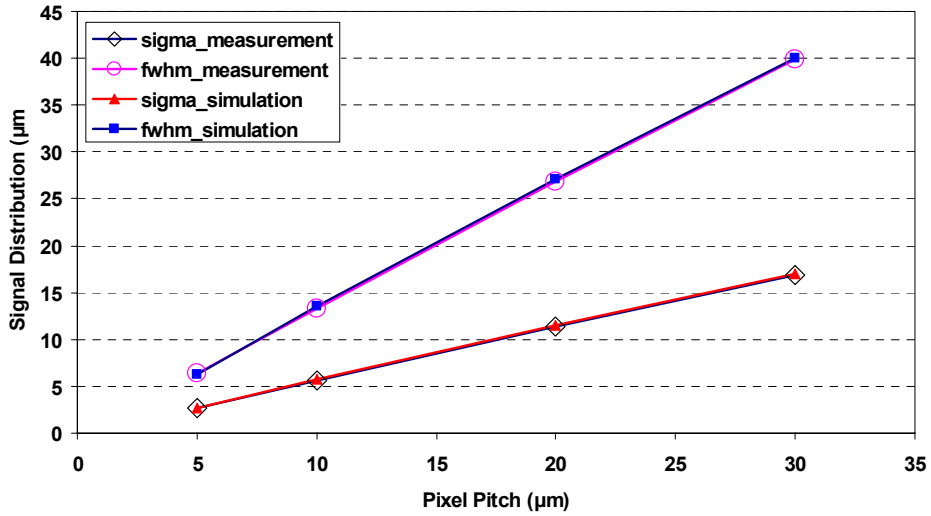

Figure 4.6: Full-width half-maximum (FWHM, upper lines) and sigma (lower lines) of the signal distribution as a function of pixel pitch ($FWHM = 2\sqrt{2\ln 2}\sigma \approx 2.3548\sigma$).

Third, measurements and simulation results of different pixel pitches showed that scaling to smaller pixel pitches results in proportionally higher spatial resolution despite the fact that charge diffusion is the dominant transport mechanism. Figure 4.6 demonstrates that this improvement continues, in simulation, down to about a 3 µm pitch, despite the fact that the epi thickness is many times greater. The simulation and measurement agrees remarkably well when the substrate events are properly accounted. Measurement and simulation of sensor response to X-ray events allow us to calibrate the Monte Carlo model and based on which we are able to tackle sensor response to high energy electrons, which will be presented in the next chapter.

4.5 Summary

Monte Carlo simulation has been applied to study sensor array response to ^{55}Fe 5.9 keV X-ray photons and compared with experimental measurement. Monte Carlo simulation reveals that x-ray events occurred in p-substrate can still lead to significant ionization electron collection, in particular, for those near the boundary between bulk substrate and epitaxial layer. The reason is two-fold: 1) the recombination rate in p-substrate is finite, although much higher than that of the p-epitaxial layer, 2) the electrical potential of the p-epitaxial layer is lower than that of the p-substrate and no barriers exist for electrons to enter into the p-epitaxial region from the p-substrate. On the other hand, ionization electrons originate from deep in silicon add to the signal intensity but result in more severe lateral diffusion. Both simulation and measurement identify that the smaller the pixel pitch, the higher the spatial resolution. Recombination loss of ionization electrons becomes noticeable when the pitch is greater than 10 μm. Simulation results agree with the measurement remarkably well when substrate contribution is properly accounted.

CHAPTER 5: HIGH ENERGY ELECTRON RESPONSE

5.1 Simulation Setup

The number of ionization electron generated by high energy impinging electrons follows Bichsel distribution and the corresponding random number generator has been discussed in Chapter 2. All the ionization electrons are assumed to distribute along the track of the incident high energy electron which strikes the center pixel of an (2n+1) by (2n+1) pixel array. The initial coordinates of ionization electrons are thus given by

$$\begin{pmatrix} x_{x,0} \\ y_{x,0} \\ z_{x,0} \end{pmatrix} = \begin{pmatrix} n \cdot pitch \\ n \cdot pitch \\ 0 \end{pmatrix} + \begin{pmatrix} randu \cdot pitch \\ randu \cdot pitch \\ randu \cdot thicknes \end{pmatrix} \tag{5.1}$$

n has to be adequately large so that no ionization electrons can go beyond the (2n+1) by (2n+1) pixel array. All ionization electrons are submitted to the Monte Carlo procedure outlined in Chapter 2. As ionization electrons are generated in both p-epi layer and p-substrate, the Monte Carlo code was slightly modified so that we could track the collection profile of ionization electrons in the p-epi layer and p-substrate simultaneously for each incident electron. With the flexibility afforded by the Monte Carlo method, we will discuss five important factors: substrate contribution, pixel pitch, diode area, epitaxial layer thickness, and the energy of incident electrons in sequence. The general methodology in the following sections would be to examining the impact of a specific parameter while holding other parameters constant or in a few fixed values. This way, we de-construct these important parameters entangled together and evaluate the relative

significance of each parameter and hopefully uncover the critical factors that can help optimize sensor performance.

5.2 General High Energy Electron Response

Similar to the case of X-ray response, typical collection matrices for individual incident electrons are examined first. However, compared to X-ray events, absorption depth is not defined for high energy electrons. High energy electrons can easily penetrate very thick silicon layer. What makes difference here is the relative location of incidence point with respect to the active collection region (the diode and the depletion region). As an example, Figure 5.1 shows the collection profiles of two high energy electron events. Only ionization electrons generated in the epitaxial layer are counted in calculating these two collection profiles.

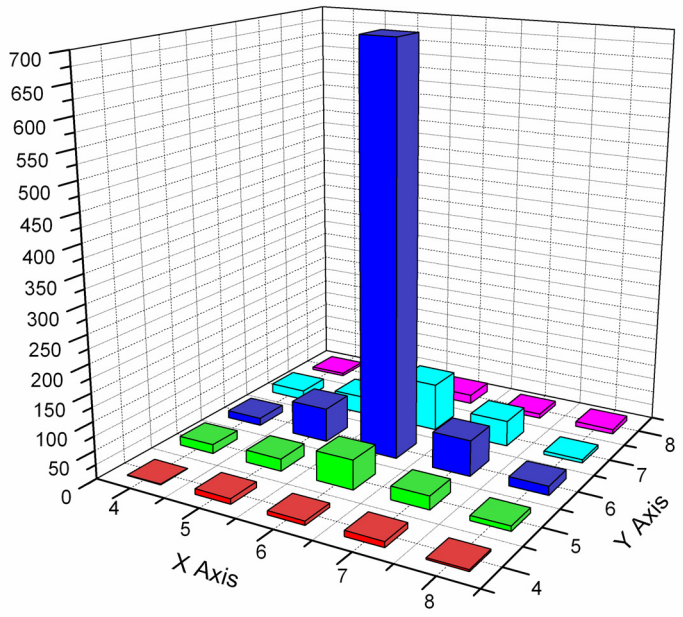

(a)

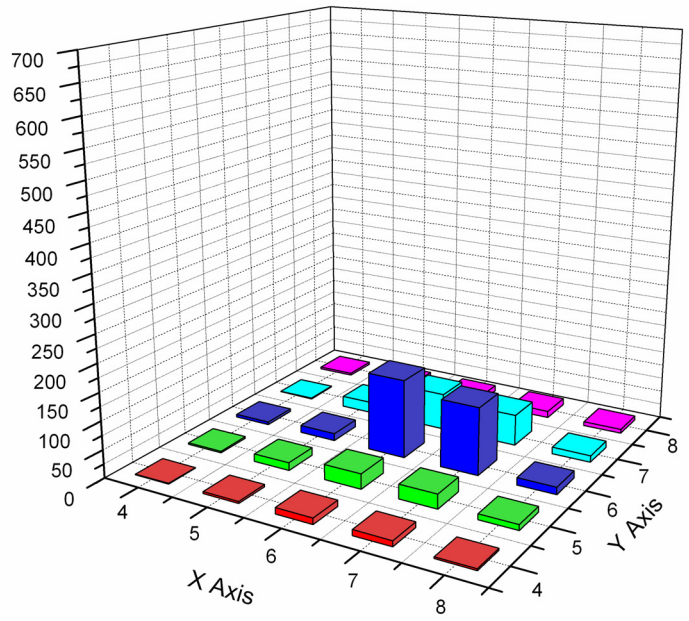

(b)

Figure 5.1: Typical single electron response only consider the p-epi contribution. (a) Strike the diode, (b) Strike outside the diode (Epitaxial layer thickness = 8 μm, pixel pitch = 5 μm, Electron energy = 300 keV).

Figure 5.1 (a) is the simulated collection profile when the incidence position of a 300 keV electron is right inside the active collection region. In this case, it is more likely for ionization electrons generated along the track to be collected by the center pixel and many of them are actually generated right inside the active collection region. Thus the center pixel in Figure 5.1 (a) collects many more ionization electrons generated in the p-epi layer than any neighboring pixels, yielding a sharp collection profile. By contrast, Figure 5.2(b) is the case when the incidence point is outside of the active collection region of a 5μm pitch pixel. Ionization electrons generated in this case are more likely to diffuse to any of the four surrounding pixels. As a result, there is no single pixel collects overwhelming greater number of ionization electrons. Lateral diffusion in Figure 5.1 (b)

is much more pronounced than Figure. 5.1 (a). The worst-case scenario is when the incident point is right at the corner of the center pixel. In this case, ionization electrons are equally likely to diffuse to any of the four surrounding pixels.

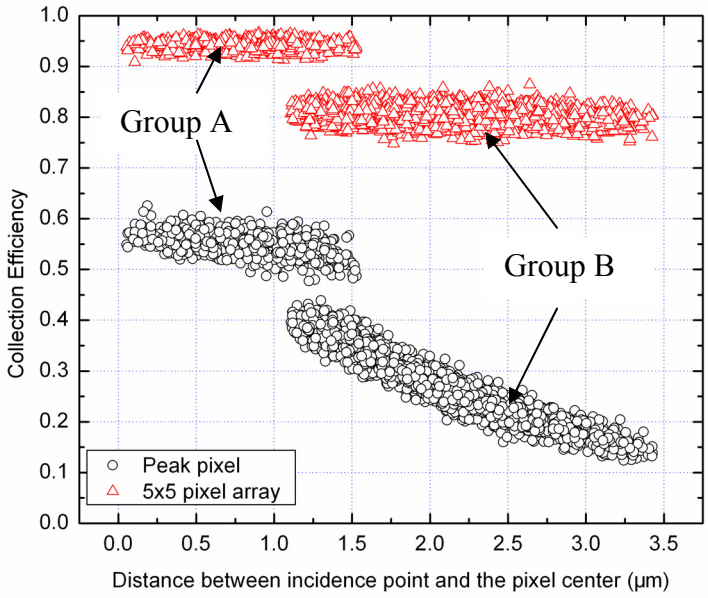

Figure 5.2: Scatter plot of collection efficiency (only consider epitaxial layer contribution) vs. incidence point and center distance (Epitaxial layer thickness = 8 μm, pixel pitch = 5 μm, Electron energy = 300 keV). Pixel clusters are the center pixel (1×1), and the 5×5 array centered on the center pixel, respectively.

Similar to those in Chapter 4 for X-ray events, we depict the scatter plots of collection efficiency of 2000 individual high energy electrons in Figure 5.3. Shown are the collection efficiencies of four different pixel clusters: 1×1 (the center pixel) and the 5×5 pixel array centered on the center pixel, respectively. The collection efficiency is calculated by dividing the number of electrons collected in each pixel cluster by the total number of ionization electrons generated in 8 μm epitaxial layer following Bichsel's theory.

There are two groups of data points in Figure 5.2. The first group consists of those data points that are calculated when the incident electrons hit right inside the diode. In this case, the collection efficiency is from 48% to 65% for the center pixel and nearly 90% for the 5×5 sum. As long as the incidence points are inside the diode area, many ionization electrons are immediately swept to the positive end of the reversely biased diode and the distance from the center of the pixel is not very critical. Group B represents the data points calculated when the incidence points are outside the diode. Ionization electrons generated in this case have to undertake many random-walk steps before reaching the active collection region and be collected. In the diffusion process, these ionization electrons may diffusion to a neighboring pixel or even disappear by recombination. As a result, the collection efficiency in this region is generally less than 40% for the peak pixel and about 80% for the 5×5 sum, both lower than those in Group A. Figure 5.2 also indicates that the further the incidence points are away from the pixel center, the larger the lateral diffusion.

5.3 A Closer Look at High Energy Electron Response

5.3.1 Substrate Effect

Both the measurement and simulation results on X-ray events in Chapter 4 have demonstrated substantial substrate contribution. For high energy electrons, as the substrate (20~30 μm for chemically-thinned chips and ~ 500 μm for regular chips) is typically much thicker than the epi layer, an incident electron can generate many more ionization electrons in the p-substrate. As shown in Figure 2.7 (b) and (c), the most probable value for the number of ionization electrons in is only ~ 550 for 8 μm silicon but

~ 1550 for 20 μm silicon, nearly three times greater. In addition, because of the difference in doping density, the p-substrate/p-epi interface can facilitate the transfer of bulk substrate electrons into the epitaxial silicon region and be collected eventually. Consequently, there may be substantial substrate contribution for high energy electron detection and we strive to quantify it.

We first show two typical collection profiles caculated solely from ionization electrons generated in the substrate in Figure 5.3 (a) and (b). These two points actually correspond to the same two incident electrons in Figure 5.1 (a) and (b). The only difference is that Figure 5.2 plots the collection profiles solely due to the epitaxial layer contribution. Compared to the collection profiles obtained from epitaxial layer ionization electrons, substrate collection profiles are much lower. For the peak value shown in Figure 5.1(a) and Figure 5.3(a), the former is about 4 times greater despite that the epatixial layer is only 8 μm thick and the simulated substrate thickness is 13 μm. Indeed, a majority of ionization electrons generated in the bulk substrate recombine and disappear. As the for the collection profiles themselves, the center pixels do not show considerably high collection values than the immediate neighboring pixels because of diffusion over long distance is required for any electrons be collected.

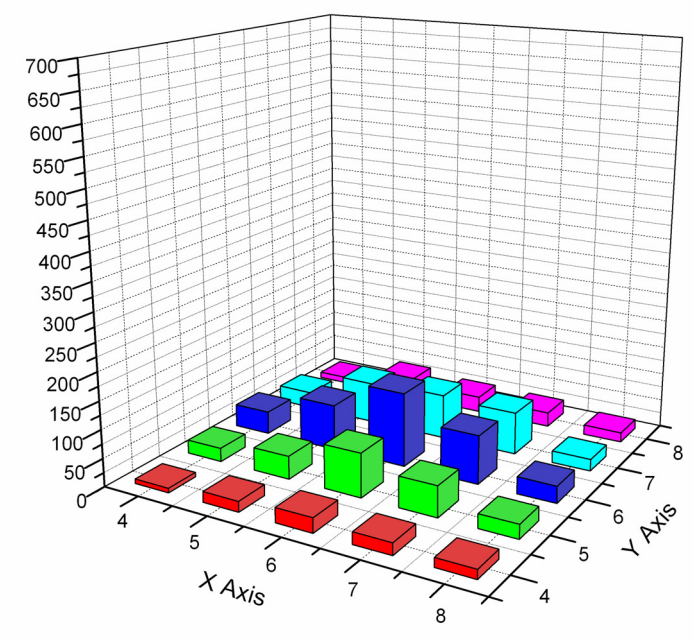

(a)

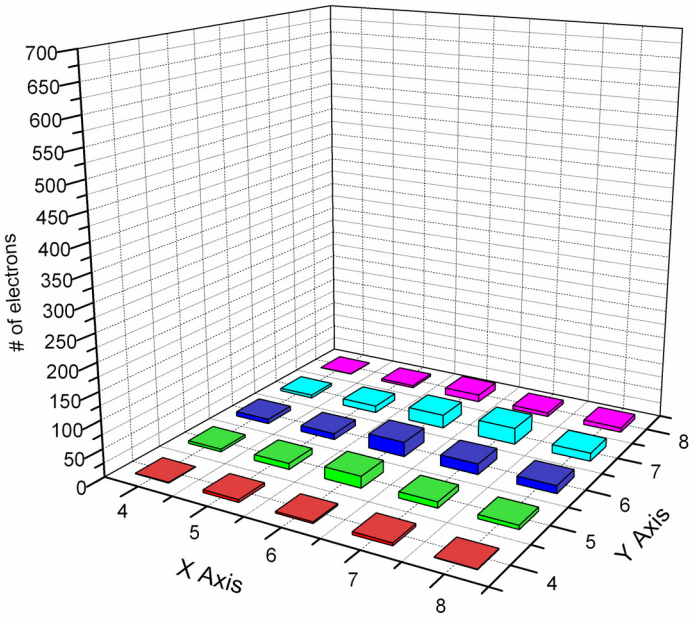

(b)

Figure 5.3: Typical single electron response only considering the bulk substrate contribution. (a) Incident electron strikes the diode, (b) Incident electron strikes outside the diode (Epitaxial layer thickness = 8 μm, pixel pitch = 5 μm, Electron energy = 300 keV).

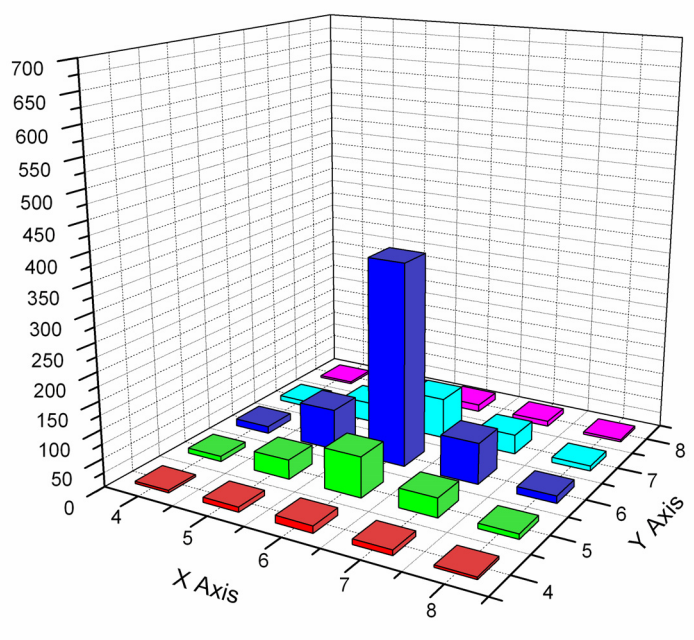
700
650
600
550
500
450
400
350
300
250
200
150
100
50
0
4
5
6
7
8
X Axis
4
5
6
7
8
Y Axis

(a)

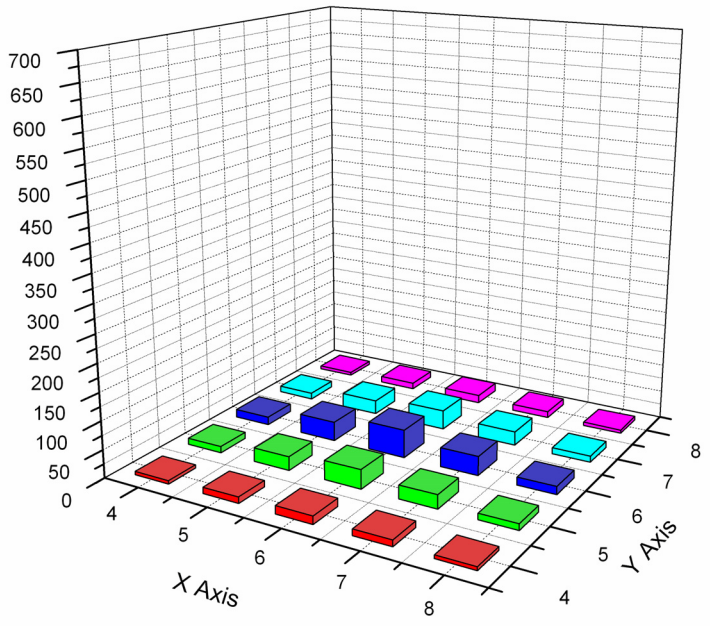
700
650
600
550
500
450
400
350
300
250
200
150
100
50
0
4
5
6
7
8
X Axis
4
5
6
7
8
Y Axis

(b)

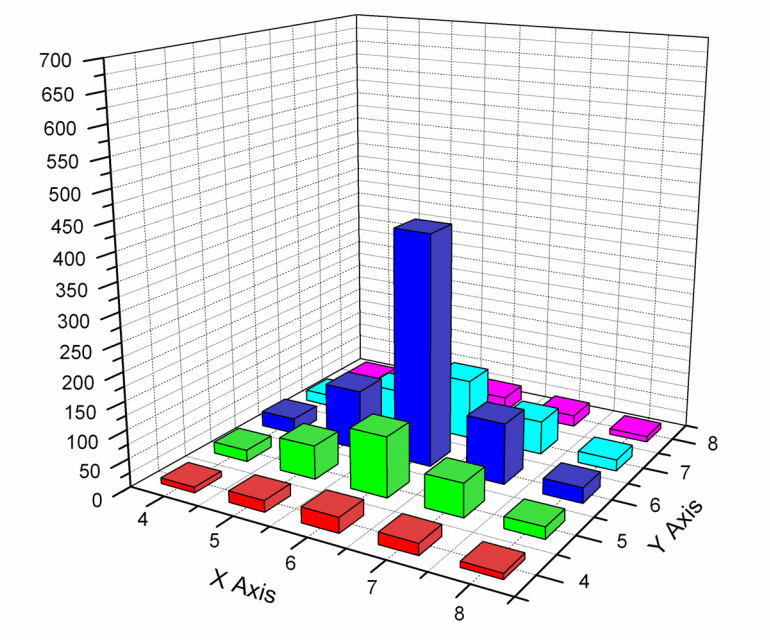

(c)

Figure 5.4: Typical single electron response only considering the bulk substrate contribution. (a) Incident electron strikes the diode, (b) Incident electron strikes outside the diode (Epitaxial layer thickness = 8 μm, pixel pitch = 5 μm, Electron energy = 300 keV).

The difference in collection values becomes clearer if we plot the average collection matrices for epitaxial layer and bulk substrate separately. In Figure 5.4 (a) and (b), we plotted the average collection matrix solely due epitaxial layer and substrate ionization electrons. On average, the epitaxial layer contributes about 5 times more ionization electron than the substrate. But substrate contribution does raise the number of ionization electrons collected per incident electron. Also shown in Figure 5.4 (c) is the combined average collection matrix, obtained by adding the average substrate collection profile to the average p-epi collection profile. The significant values (~ 87%) are enclosed in an array of 5x5 pixels. Another noteworthy comparison is the width the collection profiles if approximated using a Gaussian. The average collection profile for the substrate contribution is much wider than that of the epitaxial layer and thus adversely affecting the

spatial resolution. In Table 5.1, we listed the sigma and FWHM calculated for the average collection profile solely due to the epxitaxial and those combining the substrate contribution. The substrate contribution leads to 8.6% increase in the sigma and FWHM.

Table 5 1: Impact of substrate contribution to sigma and FWHM.

Unit: μm	σ	FWHM
p-epi only	2.75	6.48
P-epi + p-sub	3.07	7.09
Relative increase	8.5%	8.6%

Similar to the case of X-ray events, ionization electrons generated very deep in the bulk substrate may never be collected and have negligible effect on the collection matrices. In the next step, we simulated the number of ionization electrons collected vs. different substrate thickness. It is aimed to identify a critical substrate thickness, beyond which the contribution is negligible. The simulation results for 300 keV electrons are shown in Figure 5.5. Substrate thickness ranges from 0 μm to 20 μm. The pixel cluster plotted are the peak pixe, 3×3 array, and 5×5 array.

We notice all three curves in Figure 5.5 rise with the increase of substrate thickness, up to a value between 8 μm and 13 μm. Within this range, ionization electrons generated are likely to enter into the epitaxial layer and be collected eventually. When the thickness is greater than 13 μm, the collection values start to level off, suggesting that additional increase in substrate thickness makes not appreciable contribution to the average collection matrices. Second, in the rising range, the slopes for 5×5 sum and 3×3 sum are much greater than that of the pixel value, indicating more substrate electrons reach the

neighboring pixels instead of the center pixel, broadening the collection profiles. Based on these findings, 13 μm is selected as the substrate thickness that should be considered in the Monte Carlo simulation. Choose a proper bulk substrate thickness is also important when it comes to simulation speed. From the perspective of computation speed, electrons generated deep in the substrate takes huge number of random steps to reach the active collection regions on the top surface and demands a lot of CPU time. The collection matrices simulated for various substrate thicknesses suggests that the effect of ionization generated deeper than ~13 μm in the p-sub is negligible. Therefore, we only need to simulate ionization generation up to 8~13 μm, the trade-off between accuracy and simulation speed can be balanced. All simulation results discussed thereafter consider only 13 μm bulk substrate unless noted otherwise.

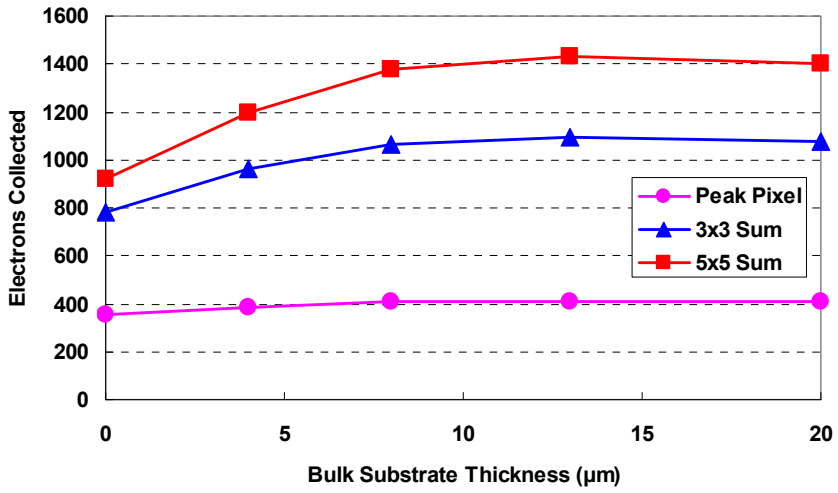

Figure 5.5: Electron collection vs. bulk substrate thickness (Epitaxial layer thickness = 8 μm, pixel pitch = 5 μm, Incident Electron Energy = 300 keV.

In experimental measurement, ionization electrons emerging from the bulk substrate are indistinguishable from those from the epitaxial silicon. An interesting question to ask is then what is the equivalent epitaxial layer thickness of the bulk substrate. This question

has been briefly examined by Dr. Deptch [55] using the built-in ionization radiation simulator in ISE-TCAD. Dr. Howard Matis [50] later developed a more sophisticated method to calculate the equivalent thickness. What he did is to calculate the equivalent thickness by matching the measured histogram of collected ionization electrons to Bichsel's theoretical histogram. Dr. Howard Matis obtained an equivalent thickness of ~ 4 μm for a similar 0.25 μm CMOS chip. The same methodology is applied here and the only difference is for us to replace the measured histogram with the simulated histogram.

The simulated histograms of ionization electrons collected in a 5×5 pixel cluster at 300 keV and 400 keV are shown in Figure 5.6 (a) and (b), respectively. In order to perform the comparison, we also show Bichsel's theoretical histograms corresponding to the nominal thickness of the epitaxial layer, which is ~ 8μm at 300 keV and 400 keV in two figures. It is clear that the simulated histogram significantly deviate from the Bichsel histograms considering only the nominal epitaxial silicon thickness. The most probable values of the simulated histograms shift right, indicating the equivalent silicon thickness is much larger. By trying many different values, we found the simulated histograms overlap nicely with Bichsel curves for 11.7 μm silicon at 300 keV and 400 keV. Therefore, the equivalent epitaxial layer thickness of the bulk substrate contribution is ~ 3.7 μm, rather close to Dr. Howard Matis's finding through experimental measurement. These findings also indicate the validity of our proposed Monte Carlo model.

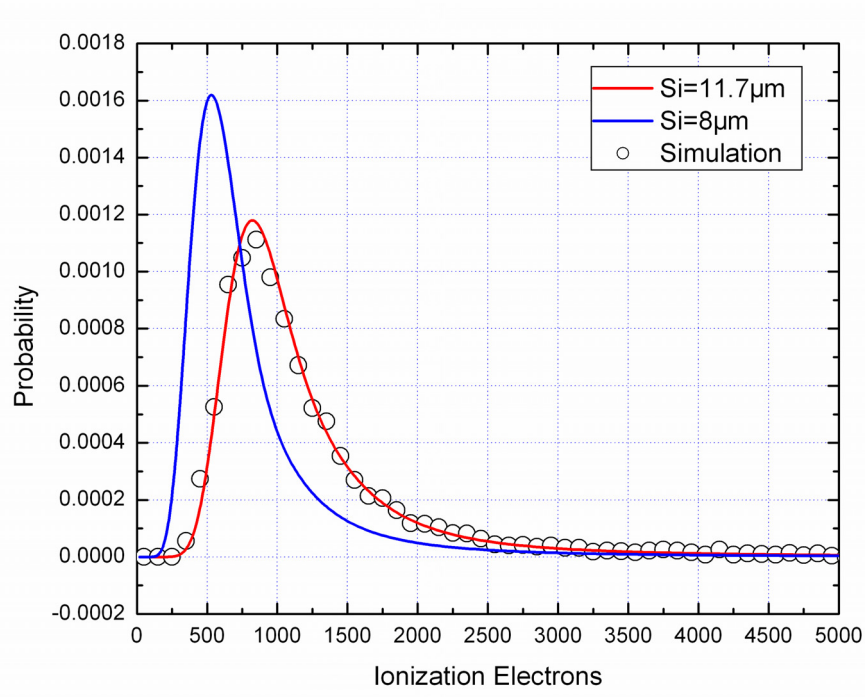

(a)

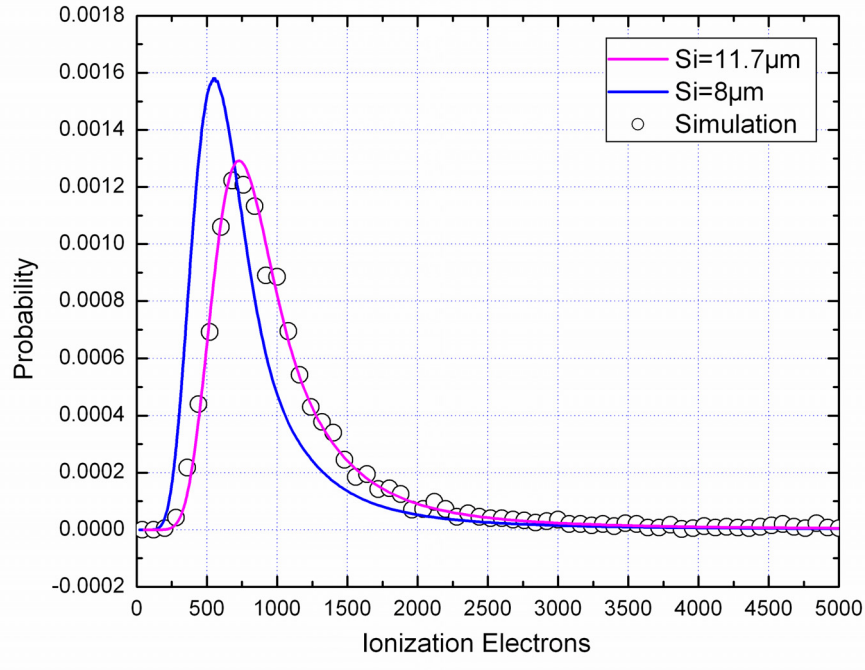

(b)

Figure 5.6: Comparing the histogram of collected electrons with Bichsel distribution (Epitaxial layer thickness = 8 μm, pixel pitch = 5 μm). (a) 300 keV, (b) 400 keV.

Chapter 4 indicates that bulk substrate contribution for x-ray events depends on bulk substrate recombination rate. This finding is also true for high energy electron detection. In Figure 5.7, we plotted the ionization electrons collected by the center pixel for various p-sub thicknesses at two different bulk substrate recombination rates. The dashed curves with hollow squares and diamonds represent the data points simulated for 300 keV and 400 keV electrons at a p-substrate recombination rate of 5×10^{-3}, respectively. The solid curves with solid squares and diamonds represent the data points simulated for 300 keV electrons and 400 keV incident electrons when the bulk substrate recombination rate is 1×10^{-4}, respectively. For both recombination rates, the substrate contribution raises the number of electrons collected at the center pixel. However, the slope of the rise is smaller for in the case of high recombination rate and the collection curves level off much more rapidly, approximately 4 μm inside the p-sub. By contrast, a lower recombination leads to greater slope of rise and the substrate continues to raise the center pixel collection up to about 8~13 μm. A possible explanation from the point view of random-walk is given as follows. Statistically, the average displacement traveled a random particle with step size s is proportional to the square root of the number of steps. Because the recombination rate, $rr_{p\text{-}sub}$, is non-zero, the probability for an electron to survive after Nr steps is given by Nr* $rr_{p\text{-}sub}$. Thus, at $rr_{p\text{-}sub} = 1\times10^{-4}$, the probability for an electron to recombine after 10,000 random steps is nearly 100%. The average distanced travel for an electron with unit step size is the product of the square root of the number steps and the step size[56]. An expected displacement of 8 μm is easily calculated this way. In another word, ionization electrons generated deeper than 8 μm has a 100% probability to recombine before

reaching the epi region on average. If the recombination rate is 50 times larger, 5×10^{-3}, similar calculation show that it only takes about 200 steps before electrons reach a collective recombination probability of 100%. With the same unit step size, this only corresponds to about 1.1 μm in displacement. As 200 is not a statistically significant number, the simulated curves shows the level-off region occurs a bit deeper than 1.1 μm. The aforementioned argument helps explain why the central pixel collection curve levels off much faster for higher recombination rate than otherwise.

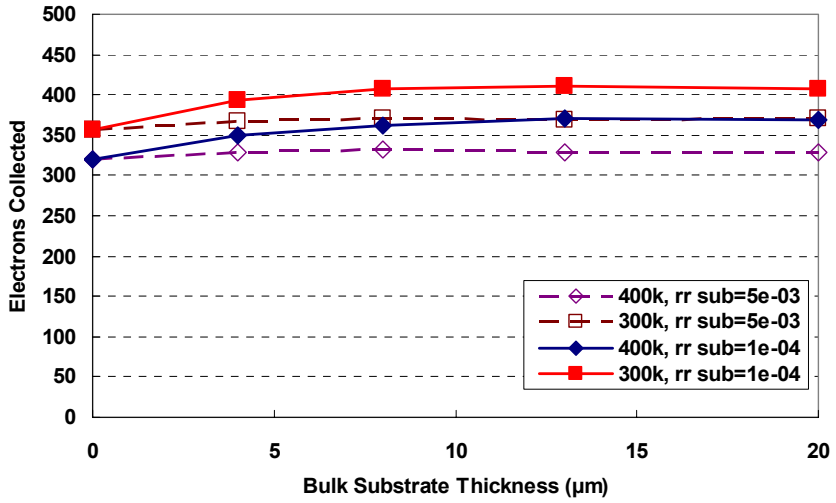

Figure 5.7: Electron collection vs. substrate thickness collected by the central pixel for em2 at 300k and 400 keV for two different p-sub recombination rates (Epitaxial layer thickness = 8 μm, pixel pitch = 5 μm).

In addition to influencing on the magnitude of the collection profile, ionization electrons from p-substrate increase the sigma and FWHM of the collection profile. We plotted in Figure 5.8 the simulated sigma and FWHM for substrate thickness from 0 to 20 μm for EM2 with 8 μm epi at 300 keV. The data for substrate recombination rate equals to 1e-04 and 5e-03 are shown simultaneously for comparison. Similar to the trend illustrated in Figure 5.7, the substrate effect increases sigma and FWHM. When the substrate thickness

is greater than 8 μm, additional increase in thickness does not further degrade sigma and FWHM as the recombination becomes overwhelming. We also plotted the relative contribution to the overall sigma and FWHM for various substrate thicknesses for 300 keV incident electrons. The contribution is less than 10 % even for a substrate thickness greater than 8 μm. The simulation results at 400 keV show similar behavior.

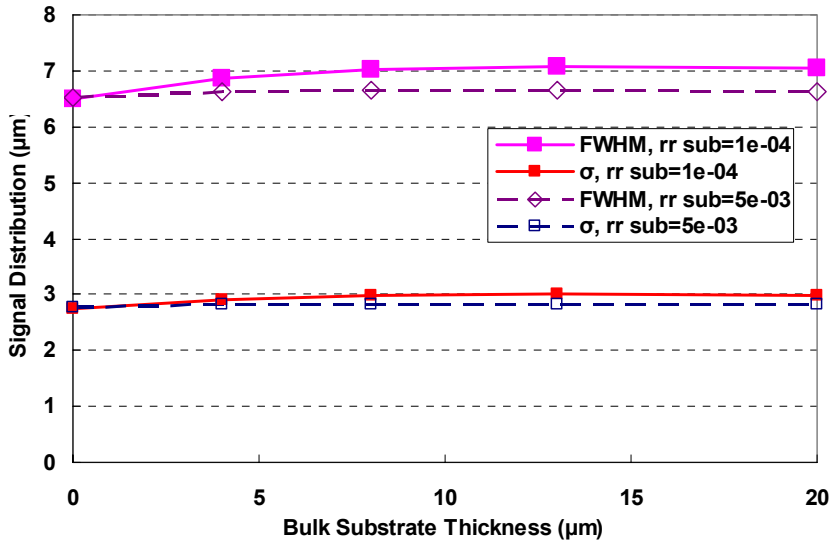

Figure 5.8: FWHM and sigma simulated for em2 for different recombination rates at 300 keV (Epitaxial layer thickness = 8 μm, pixel pitch = 5 μm).

5.3.2 Pixel Pitch

In general, smaller pixel pitch translates into higher spatial resolution for optical imaging. In the case of electron imaging, as the dominating charge transport mechanism is diffusion, the scaling law of spatial resolution with respect to pixel pitch need to be re-examined and we present our important findings in this sub-section.

We first revisit the collection profiles corresponding to individual incident high energy electron at two extremes: 1) the incidence point is right at the center of the pixel array

(center event), 2) the incident point is right at the corner of the center pixel (corner event). General situations approaching the two extremes have been discussed in Section 5.1). The difference here is the Bichsel random number, that is, the number of ionization electrons generated is selected from a value very close to the most probable value from the Bichsel histogram. It is held the same for both the corner event and the center event for direct comparison. A small diode area of 0.16 μm2 is used so that the pixel pitch can also be scaled to a very small value. The collection profiles considering only the epixtaxial layer contribution for the corner event and the center event are plotted in Figure 5.9 (a) and (b), respectively. For both Figures, the collection profiles are concentrically symmetrical with respect to the incidence points. For the corner event, ionization electrons are nearly equally collected by the 4 pixels immediately surrounding the incident point. This is actually the worst-case scenario for calculating FWHM mentioned in Section 5.1, as no single pixel has higher collection values than others. For the center event, because the incidence point is right at the center, ionization electrons generated close to the top surface are more likely to diffuse to the collection region of the center pixels and be collected. For electrons generated deep in the epi layer, the distance advantage of the center diode became less significant. The collective outcome would be high center collection efficiency and also the best case scenario for calculating FWHM ~ 5.07 μm as shown in Figure 5.9 (b).

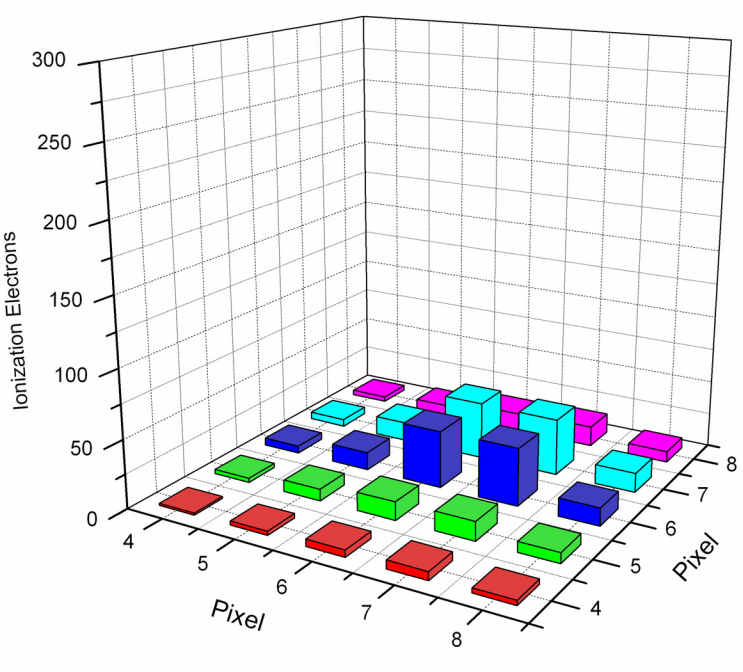

(a)

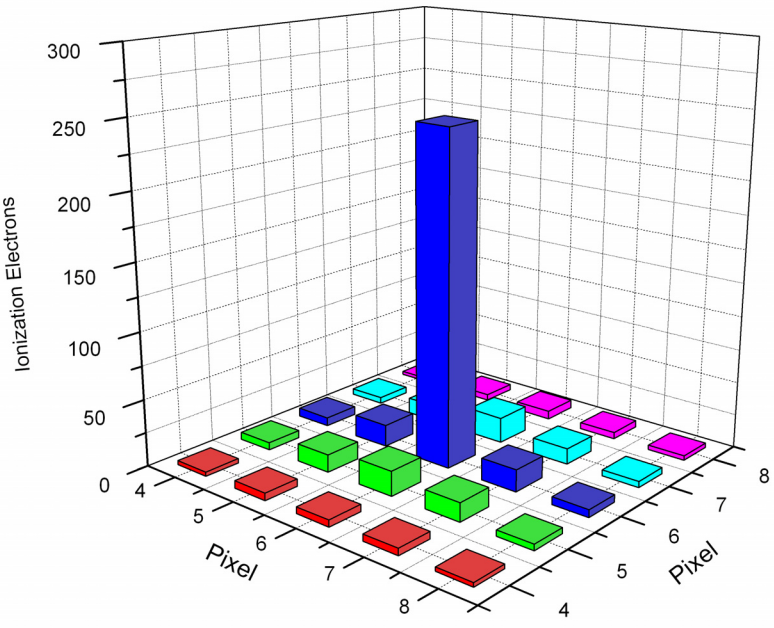

(b)

Figure 5.9: Drastically different collection profiles for the same impinging electron ionization. (a) Incident electron strikes the pixel center, b) Incident electron strikes the pixel corner.(Epitaxial layer thickness = 8 µm, pixel pitch = 5 µm, Incident electron energy = 300 keV, $rr_{p\text{-}sub}$=0.0001, only considering epitaxial layer contribution).

Next, we present the scaling of the collection efficiency for the center event with respect to pixel pitch in Figure 5.10. The simulation is done similar to those presented in Figure 5.9. The data points for collection efficiencies at difference pixel cluster sizes are calculated by dividing the sum of ionization electron by the original Bichsel random number, which is held constant for all the simulation runs here. In order to reduce statistical variation, the same simulation run was for many times and the average collection matrix for the same center event is adopted. The four curves in Figure 5.10 stand for the percentage of simulated collection values for the center pixel, the 3×3 sum, 5×5 sum divided by the number of ionization electrons obtained from Bichsel distribution. The pixel pitch ranges from 0.8 μm to 20 μm.

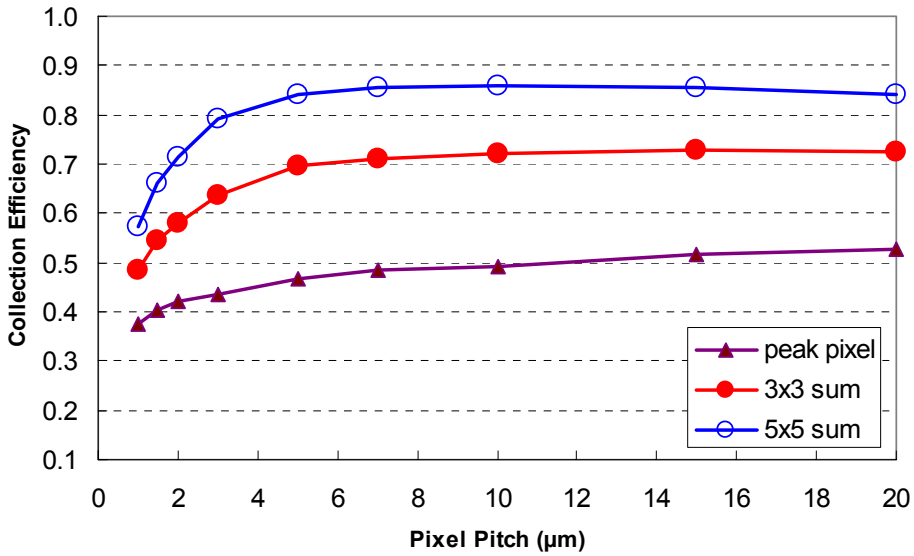

Figure 5.10: The average collection profile for center events (Epitaxial layer thickness = 8 μm, pixel pitch = 5 μm, Incident electron energy = 300 keV, $rr_{p\text{-}sub}$=0.0001, only considering epitaxial layer contribution).

The first observation from Figure 5.10 is collection efficiencies simulated rises with the increase of pixel pitch from 0.8 μm to 10 μm. For pixels with larger pitch, ionization

electrons have to travel longer distance in order to reach the neighboring pixels. At each point along the random-walk pathway, it is always equally likely for ionization electrons to turn back to the center pixel instead of the neighboring pixels. Then, when pixel pitch becomes larger than 10 μm, ionization electrons have to travel a much longer distance before reaching an active collection region are thus subject much high probability to recombine and disappear. This is reflected by the slight decrease of collection efficiency for the 5×5 sum in Figure 5.10 when the pitch is greater than 10 μm. These findings are consistent with the average collection efficiencies presented for X-ray events.

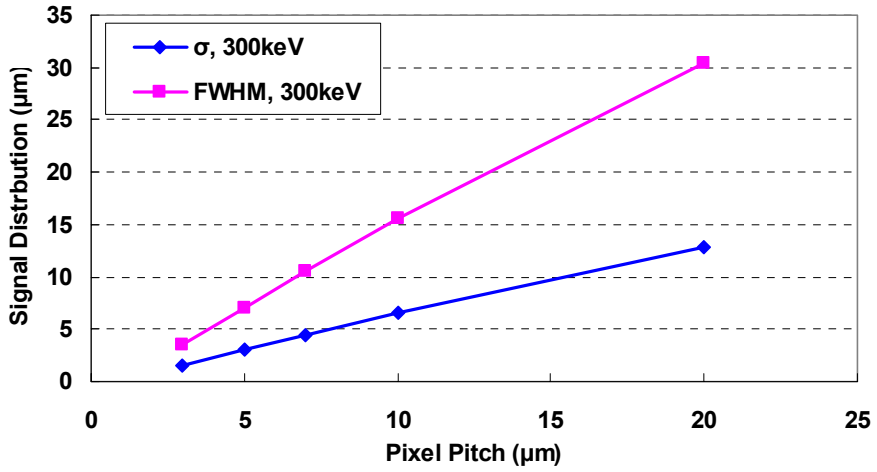

Figure 5.11: Signal distribution vs. pixel pitch for 300 keV electrons (Epitaxial layer thickness = 8 μm, pixel pitch = 5 μm, Incident electron energy = 300 keV, $rr_{p\text{-}sub}$=0.0001).

In order to understand the collective behavior of pixel array in response to high energy electrons, we set up the Monte Carlo procedure to take tens of thousands of Bichsel random numbers, each corresponding to the ionization electrons generated by an individual incident high energy electron. Many collection matrices at different pixel pitch values were obtained this way and the average collection profiles were then approximated using a Gaussian. The sigma and FWHM of the Gaussian approximation with respect to

various pixel pitch values are shown in Figure 5.11. Despite the fact that charge diffusion is the dominant transport mechanism, the spatial resolution scales linearly with pixel pitch, down to at least 3 μm in Figure 5.11. Simulation runs for 400 keV electrons also show similar trend. We would not plainly extrapolate the simulation results to even smaller pitch. As the device dimension becomes small, the boundaries between different layers may be very complicated due to dedicated fabrication process. An accurate modeling of finer devices would necessitate detailed knowledge of a given fabrication process, beyond the reach of our simple step-junction approximation and finite element analysis in ISE-TCAD assuming ideal boundary conditions in 0.25 μm CMOS technology. Another important aspect should be considered for smaller pitch in finer technology is read-out bandwidth. In finer CMOS technologies, devices may exhibit relatively larger leakage current. In order to avoid pixel saturation due to relatively large leakage current, the integration time may have to be reduced. A greater number of pixels per unit area and shorter integration time may demand excessively large read-out bandwidth. For our electron image sensor design in 0.25 μm CMOS technology, we have selected 5 μm pitch as the optimum value considering the design rule and spatial resolution.

5.3.3 Diode Area

Diode area is another major concern in the pixel design. We first simulated the average collection matrices for various diode areas for 5 μm pitch pixels. Plotted in Figure 5.12 are the peak pixel collection values for 300 keV electrons and 400 keV electrons. The left-most data points in Figure 5.12 represent small diode area calculated using finite element analysis tool in ISE-TCAD instead of simple step-junction approximation.

Figure 5.12 shows that for a given pixel pitch, a large diode would pick up more ionization electrons than a smaller diode.

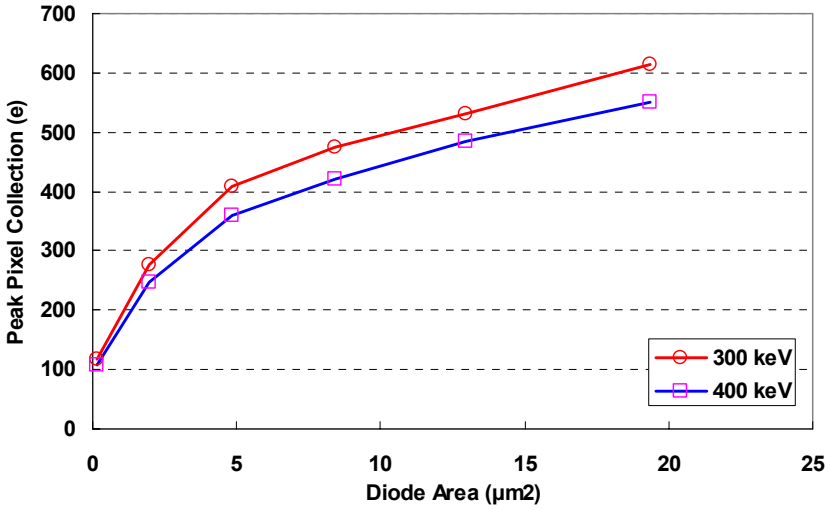

Figure 5.12: Ionization electrons collected by center pixel vs. diode area for 300 keV electrons and 400 keV electrons (Epitaxial layer thickness = 8 µm, pixel pitch = 5 µm).

While a larger diode collects more ionization electrons, more noise electrons can also be collected. On the other hand, smaller diode may collect less ionizations but the noise electron it picks up may also drops. The dependence of signal-to-noise ratio on diode area is plotted in Figure 5.13. The noise data are derived from the dark current measurement for EM3. The simulation alludes that achieving a maximum SNR requires a rather small diode area, even smaller than the minimum diode in the 0.25 µm process). When very small diodes are used, the dominant source of capacitance at the diode readout node is not the diode itself but the readout out transistor gate capacitance in addition to other sources such as the reset transistor drain. Every effort must be made to keep stray capacitance as low as possible.

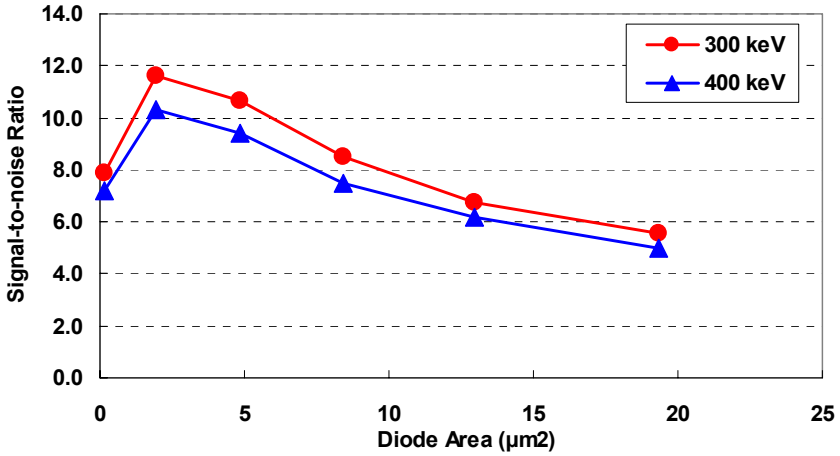

Figure 5.13: Signal-to-noise ratio vs. diode area for 300 keV electrons and 400 keV electrons (Epitaxial layer thickness = 8 µm, pixel pitch = 5 µm).

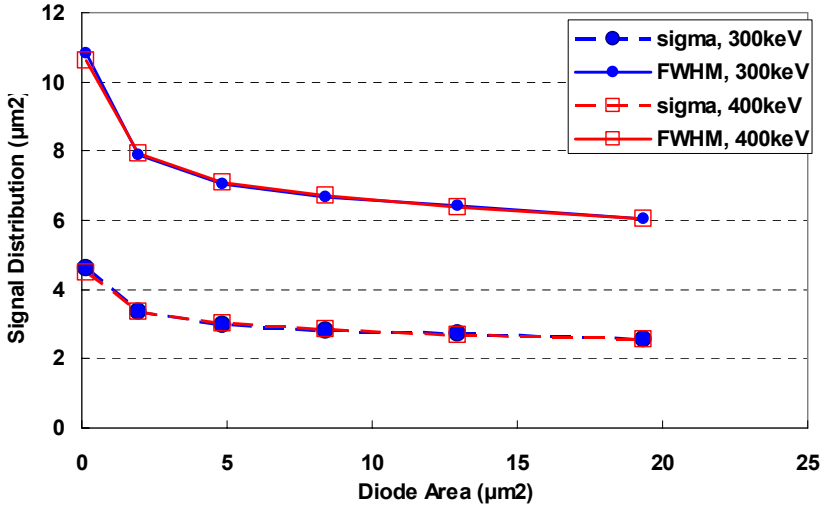

Figure 5.14: Signal distribution (FWHM and sigma) vs. diode area at 300 keV and 400 keV (Epitaxial layer thickness = 8 µm, pixel pitch = 5 µm).

Diode area has less influence on the spatial resolution characterized by FWHM and sigma and the data points simulated for 300 keV and 400 keV electrons are shown in Figure 5.14. The general trend is that the smaller the diode, the larger the signal distribution due to reduced local collection efficiency. The smallest diode area allowable in 0.25 µm CMOS design rule is around 4 μm^2. Shrinking the diode area from right to the

left up to this point gives very limited spatial resolution degradation, as compared to a much stronger relationship between pixel pitch and spatial resolution.

5.3.4 Epitaxial Layer Thickness

As shown in Figure 2.7, ionization generation has strong dependence on the thickness of silicon layer where the high energy electrons pass by. Intuitively, a thick active region could be superior, as it results in more ionization charge per incident particle. However, under this circumstance the pixel pitch may be small compared to the depth of the volume in which ionization electrons diffuse, and the extent of lateral diffusion may be large, reducing contrast and spatial resolution.

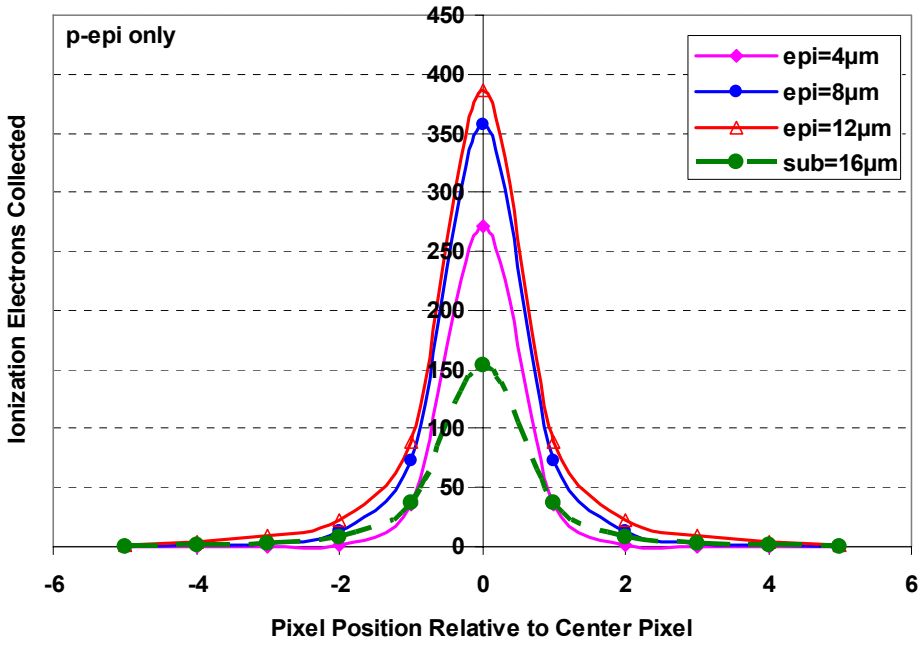

Figure 5.15: Average signal strength in electrons and lateral spreading expressed in pixels vs. silicon thickness (Epitaxial layer thickness = 8 μm, pixel pitch = 5 μm, Incident electron energy = 300 keV). Substrate contribution is temporarily neglected in calculating the three epi curves.

Figure 5.15 shows a set of simulation results of the average amount and spread of ionization electrons collected by 5 μm pixels in response to a 300 keV incident electrons, for silicon thicknesses ranging from 4 to 12 μm. Only ionization electrons generated in the epitaxial layer are considered here. As expected, increasing the silicon thickness results in an increased amount of collected charge, but with decreasing benefit, as well as increasing lateral charge spread. Note that there is no distinction between ionization electrons from the epitaxial silicon and the bulk silicon. We have shown previously that substrate also contributes charge due to finite recombination rate. For comparison, collection profile when the diode is built upon n-well over bulk substrate is also shown in Figure 5.16 as the dashed curve. With about 8 μm epiatxial, the signal strength is about 2.5 times larger than without epitaxial layer. Two possible reasons why the nwell over bulk substrate scheme achieves much lower signal strength are: 1) the depletion region is much smaller for n-well/p-substrate diode. A simple estimation using step-junction model gives only about 0.2 μm depletion width for n-well/p-substrate diode. By contrast, the depletion width for n-well/p-epitaxial diode is about 2 μm and it is primary located in the more lightly doped epitaxial region. 2) the recombination rate in the bulk substrate is much larger, about 3 orders of magnitude larger than that of epitaxial layer according to our previous calculation. This may also explains why our earlier testing of conventional CMOS image sensor chips for electron imaging produced inadequate signal-to-noise ratio.

Figure 5.16 shows the simulated spread in collected charge, expressed in sigma and FWHM, as the silicon thickness varies. One can see that the spatial resolution worsens as

the silicon thickness is increased due to the increase in lateral charge diffusion. Above about 12 μm thickness no significant further degradation occurs in that deeply liberated charge suffers increased probability of recombination and lateral diffusion.

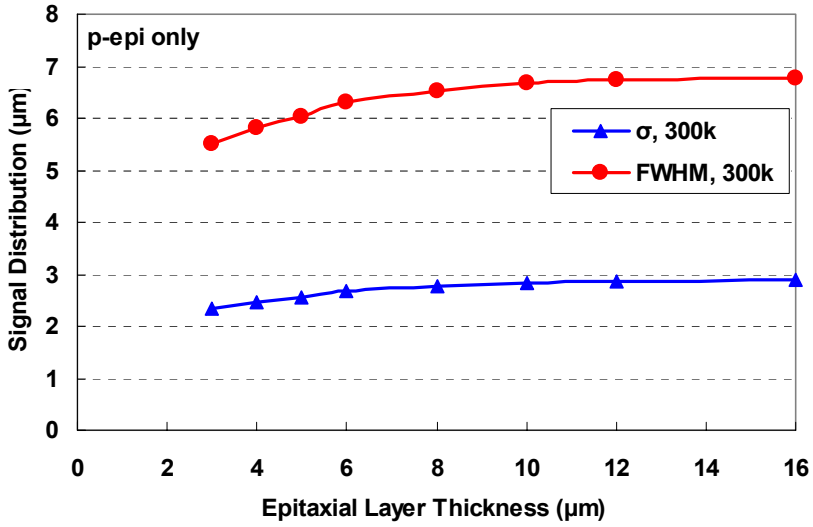

Figure 5.16: The impact of epitaxial silicon thickness on spatial resolution, expressed s the sigma and FWHM (Epitaxial layer thickness = 8 μm, pixel pitch = 5 μm, Incident electron energy = 300 keV). Substrate contribution is temporarily neglected in calculating the three epi curves.

Next, we show the combined collection profiles where ionization electrons from the bulk substrate are also considered. Similar to Figure 5.15, the simulated average amount and spread of collected charge for 5 μm pixels in response to 300 keV incident electrons are shown in Figure 5.17. Similar curve calculated for n-well over p-substrate diode is also plotted for comparison. And the simulated spread in collected charge, expressed in sigma and FWHM, as the silicon thickness varies is shown in Figure 5.18. Because of additional ionization electrons collected from the substrate, all three profiles corresponding to 4 μm, 8 μm and 12 μm epitaxial silicon rise. The curve corresponding to 4 μm eptiaxial layer has the largest gain. For a thinner epitaxial layer, ionization electrons generated in the substrate are more like to be collected by the struck pixel, because they are closer to those

beneath thicker epitaxial silicon in the sensor array. The gain in signal strength for thicker epitaxial layer is much smaller due to increased probability of recombination and lateral diffusion. Due to substrate contribution, in particular, relatively larger substrate contribution when the epitaxial layer is thinner, the spatial resolution levels off much faster than that in Figure 5.17. ~ 4 μm epitaxial silicon may be sufficient to maintain adequate signal strength while achieve better spatial resolution. The relative bulk substrate contribution vs. epitaxial silicon thickness expressed in sigma is plotted in Figure 5.19. The data points in square are obtained for the substrate recombination rate of 0.0001 and those in diamond corresponding to the simulated results when the bulk substrate recombination rate is about 50 times larger.

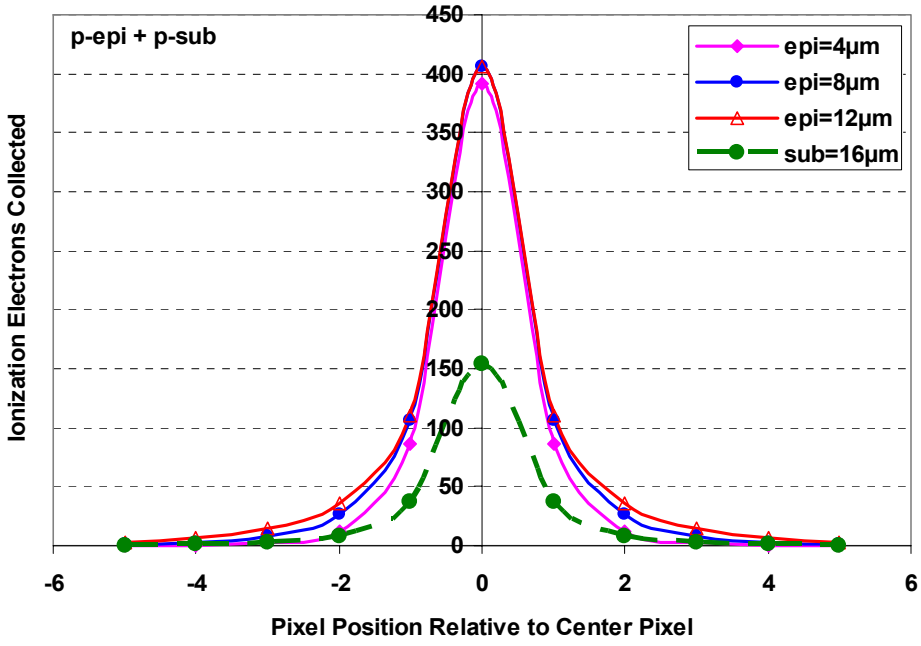

Figure 5. 17: P-epi thickness vs. sigma for EM2 at 300 keV, combining electrons collected from p-epi and p-substrate.

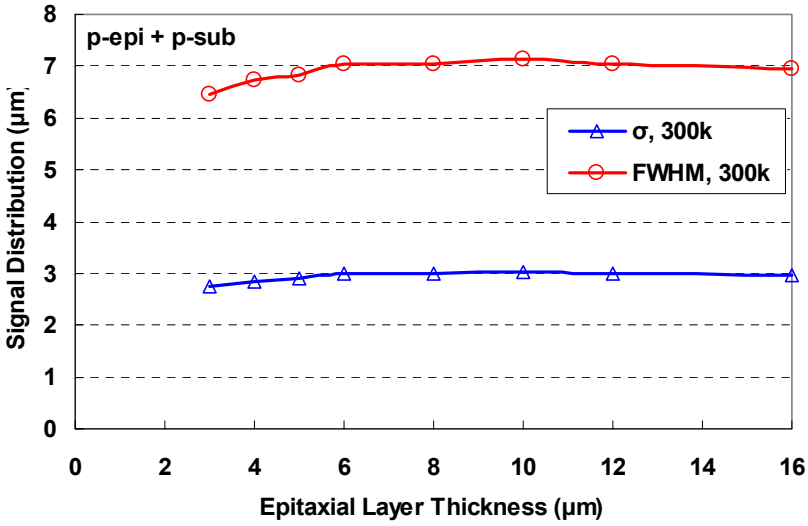

Figure 5.18: The impact of epitaxial silicon thickness on spatial resolution, expressed s the sigma and FWHM (Epitaxial layer thickness = 8 µm, pixel pitch = 5 µm, Incident electron energy = 300 keV).

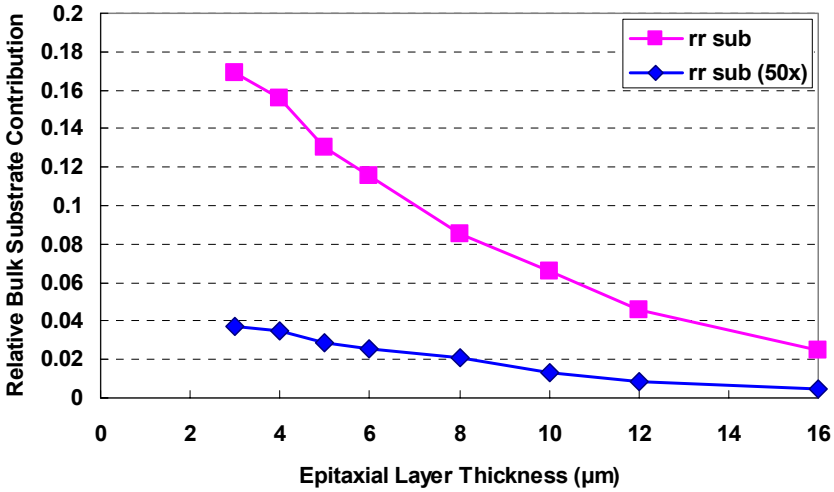

Figure 5.19: Relative bulk substrate contribution. he impact of epitaxial silicon thickness on spatial resolution, expressed s the sigma and FWHM (Epitaxial layer thickness = 8 µm, pixel pitch = 5 µm, Incident electron energy = 300 keV).

Another interesting question we would like to address is the average single electron response when the doping density of the epi layer is similar to the p-substrate. In other words, we would like to know the sensor response when the diode is built on a regular p-

type wafer without the epi layer, which is n-well/p-substrate. High doping density of the p-substrate not only dramatically increases the recombination rate, but also leads to much more narrow depletion region, as demonstrated by both step-junction approximation and finite element method in ISE-TCAD. With new physical parameters extracted and plugged into the simulation program, we obtained the single electron response for sensor array with n-well/p-substrate diodes. Shown in Figure 5.20 is the average single electron response of sensor array with n-well/p-substrate diodes at 300 keV simulated with respect to various substrate thickness, respectively.

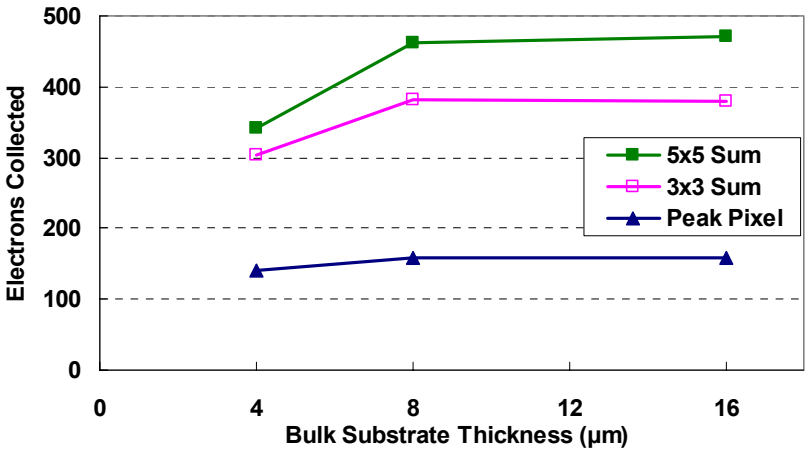

Figure 5.20: Average ionization electron collection for pixel array with n-well/p-substrate diodes vs. various bulk substrate thicknesses (pixel pitch = 5 µm, Incident electron energy = 300 keV).

It is worthwhile to take a further look at the performance of pixel array with n-well/p-substrate diodes. The average collection profile was simulated for bulk substrate thickness ranging from 4 µm to 16 µm and the results are plotted in Figure 5.20. Because of the high recombination rate in the p-substrate, the number of electrons collected by n-well/p-substrate diodes is much less than those of diodes built on epitaxial silicon. Beyond a p-substrate thickness of 8 µm, both the central pixel collection value and 3×3

sum value saturate. Additional increase in the 5×5 sum is also much less pronounced. We used the simulation results corresponding to 16 μm bulk substrate in all other figures in this subsection.

5.3.5 Electron Beam Energy

As shown in Figure 2.6, ionization generation also depends on the energy of incident electrons. For a silicon layer of given thickness, a lower energy leads to larger likelihood in depositing more energy in the silicon and thus leading to a larger most probable value in Bichsel histogram.

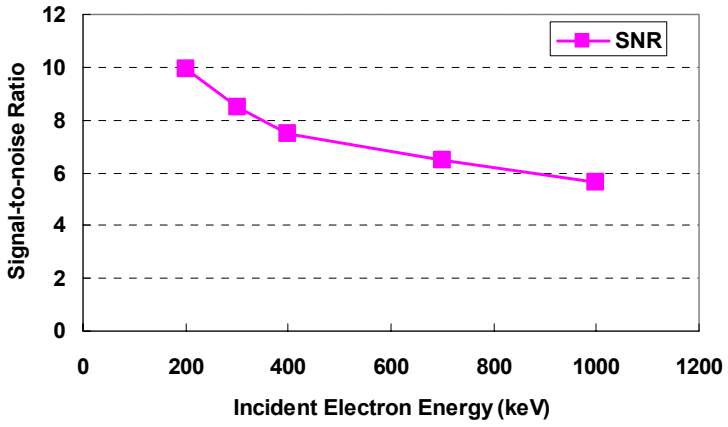

Figure 5.21: Signal-to-noise ratio vs. incident electron energy (Epitaxial layer thickness = 8 μm, pixel pitch = 5 μm).

We simulated the average collection profiles for incident electrons with energy ranging from 200 keV to 1000 keV. The signal-to-noise ratio calculated for peak pixel is shown in Figure 5.21. The noise data is from the measured dark current for EM3. It can be seen clearly that higher energy electrons tend to produce lower signal-to-noise ratio due to the left-shift of most probable value in Bichsel histogram.

Additionally, the signal distribution due to the difference in incident electron energy is shown in Figure 5.22. It is somewhat surprising that the sigma and FWHM are almost the same for a very wide range of incident electron energy. In the real imaging experiments, simply increasing the acceleration voltage of the transmission electron microscope would have very limited effect on the sensor spatial resolution. But this observation does not necessarily suggests that lower acceleration voltage is more favorable. As they deposit more energy when passing the sensor body and yields high signal magnitude, lower energy electrons are more likely to experience backscattering, a detrimental effect that seriously degrades the spatial resolution and often times leads spurious counts. Our model presented here does not take into account backscattering. Additionally, the resolving power of an electron microscope is proportional to the wavelength of electrons, which is inversely proportional to the square root of the kinetic energy. Higher energy electrons can resolve finer structure than lower energy ones and may be more desirable in certain applications.

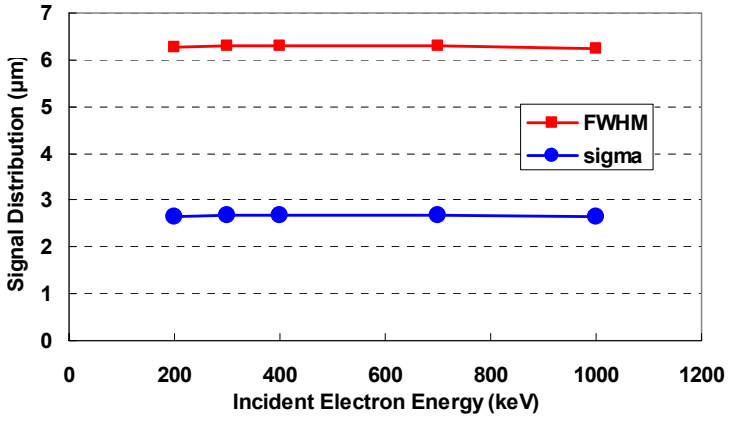

Figure 5.22: Signal distribution vs. incident electron energy (Epitaxial layer thickness = 8 μm, pixel pitch = 5 μm).

5.4 EM3 Testing and Measurement

5.4.1 Representative Images of Biological Samples Taken Using EM3

To see is to believe. With a pixel array consisting of 512 by 550 pixels, EM3 allowed us to capture images of biological samples in transmission electron microscopes. Figure 5.23 is a representative image of a mouse's muscle cell taken using 200 keV electrons. Muscle is a classic example of a biological structure-function relationship. The dark area in the middle is the mitochondria that are responsible for oxidative metabolism of nutrients. The lines around the mitochondria are the muscle fibers. High resolution images like these can facilitate the diagnosis and treatment of muscle diseases.

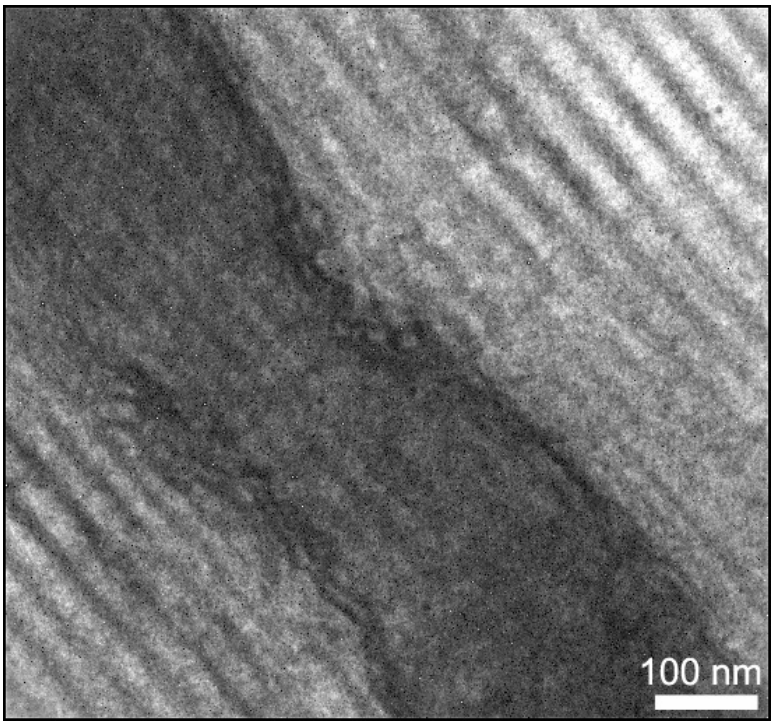

Figure 5.23: Longitudinal cross-section of a mouse's muscle cell taking using EM3 (Incident electron energy: 200 keV).

Figure 5.24 is an image of a negatively stained catalase crystal taking at 300 keV in a TEM at a magnification of 10k, using EM3. Catalase is a common enzyme found in living organisms. Its functions include catalyzing the decomposition of hydrogen peroxide, a waste product of metabolism in many living organisms, into water and oxygen. Catalase can form rectangular 2D crystals and has long been used in electron microscopic studies of protein structure-function relationships. The main lattice spacing of catalase crystals (8.75nm) and 6.86 nm) are clearly resolved. The darker regions are due to the overlapping of more than one catalase membrane, a common phenomena in protein crystallization.

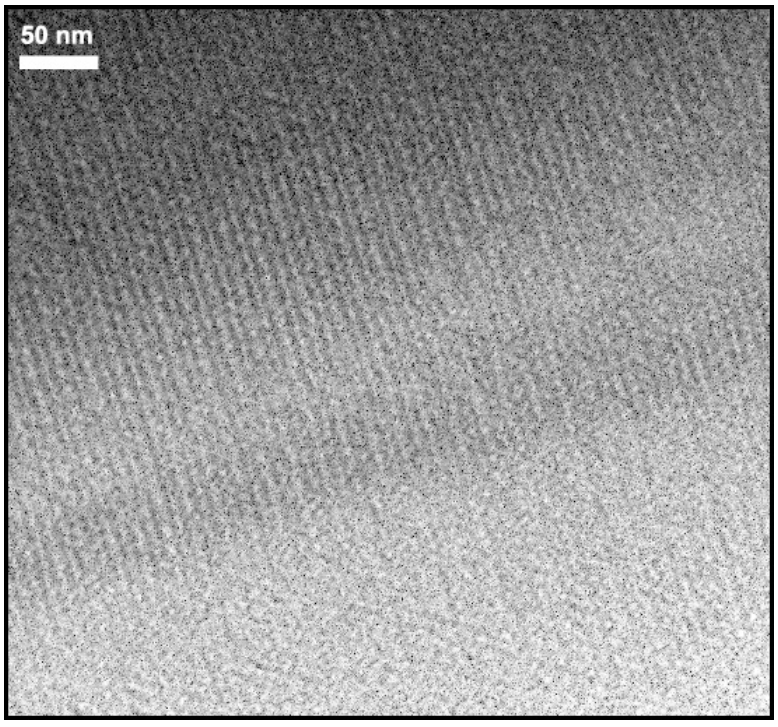

Figure 5.24: Catalase crystal image taken using EM3 at a magnification of 10k (Incident electron energy: 200 keV)..

We also attempted to directly compare our direct electron imaging sensor with the indirect CCD counterpart. We used a nerve cell's myelin sheath as the example.

Individual layers in the myelin sheath are about 10 ~ 15 nm apart. The images taken using EM3 clearly clearly resolve these structures in Figure 5.25. The spatial resolution of our direct electron imaging sensor is much higher as compared to the CCD counterpart. Due to the limited number of pixels available in EM3, we would delay a quantitative comparison to a much larger prototype chip.

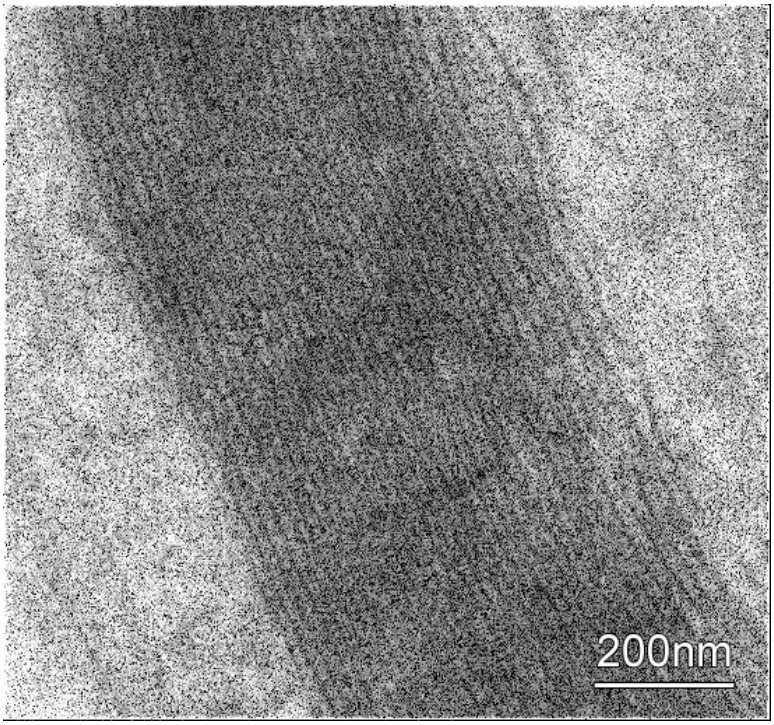

Figure 5.25: Neuron myelin sheath image taken using EM3 (Incident electron energy: 200 keV).

5.4.2 Summary of EM3 Performance

The performance of EM3 is summarized in Table 5.2. Modulation transfer function (MTF) of the sensor array at the Nyquist limit is estimated by approximating the incident electron point spread function as the average impulse response for the pixel[16]. MTF is then given by:

$$MTF = \frac{-\rho\frac{\pi}{\lambda} + \sin\frac{\pi}{\lambda} - \rho\sin^3\frac{\pi}{\lambda}}{\frac{\pi}{\lambda} - \rho\sin\frac{\pi}{\lambda} + \rho\sin^3\frac{\pi}{\lambda}} \tag{5.2}$$

where ρ is the ratio of diffusion signal component to the overall signal collected and λ=2 at the Nyquist frequency. We find the MTF at the Nyquist limit to be equal to 31.4 %.

Table 5 2: Summary of EM3 Performance

Parameter	Value
Process	0.25 μm 5M, 1P CMOS
Pixel pitch	5 × 5 μm
Diode size	2.5 × 2.5 μm
Noise (temporal)	~1 mV, RMS
Noise (fixed pattern)	~4 mV, RMS
Sensitivity	24 μV / e-
Range	41,000 e-
Dynamic range	60 dB
Dark current	18.2 nA/cm2 at room temperature
Power @ 70 frames/s	20 mW
MTF @ Nyquist limit	32% for single incident e-

5.4.3 Radiation Tolerance

A critical issue in direct charged-particle imaging is radiation tolerance[57]. The main mechanism of radiation damage due to energetic electrons is the generation of charge traps in the sensor's oxides, which in turn translates into increased dark current[14, 58, 59]. The dark current of the prototype prior to irradiation was ~18.2 nA/cm^2 when

measured at room temperature, similar to that measured in other image sensors fabricated in standard CMOS processes[60].

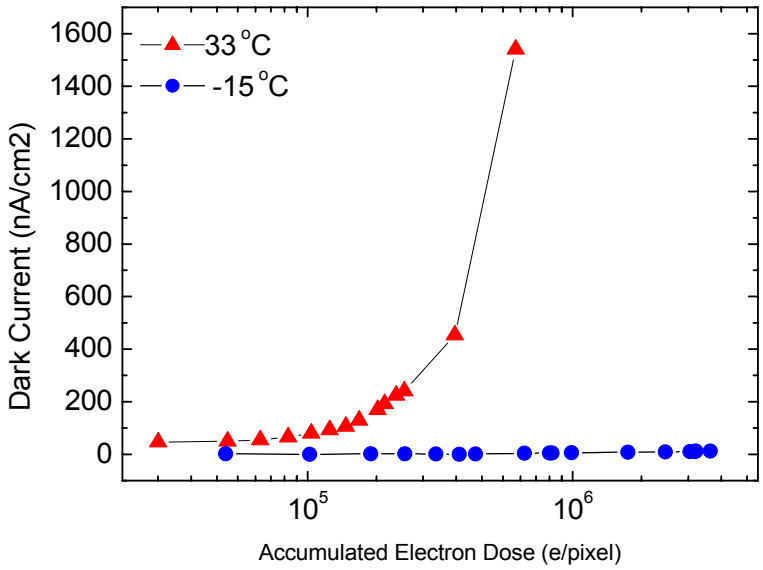

Figure 5.26: Dark current vs. electron dose (EM3, incident electron energy: 300 keV).

To study the radiation tolerance, an EM3 chip was exposed to a continuous 300 keV electron beam at an average intensity of 5 electrons/pixel/second. The change of dark current with respect to accumulated electron dose was monitored and plotted in Figure 5.26. At 33 °C, the dark current increased rapidly, leading to saturation of the pixels when the total dose reached 6.5×10^5 electrons/pixel. However, when cooled to -15 °C, the sensor exhibited comparatively little performance degradation even when 10 times higher total dose was applied. Furthermore, radiation-damaged sensors could be recovered by thermal annealing at 80 °C for one day. Results to date demonstrate that cooling and/or annealing the sensors should permit at least a year of full-time operation in an electron microscope. Radiation-hardened design techniques[61-63] may be pursued in the continued development of this project.

5.5 Summary

While a general analytic optimization is difficult, Monte-Carlo simulation and experimental measurement have enabled us to analyze five important factors that are critical in determining the performance of the direct imaging sensor array. First, the bulk substrate effect is studied systematically in a quantitative manner. Due to finite recombination rate, substrate contributes significant among of ionization electrons, enhancing signal strength but adversely affecting spatial resolution. The equivalent eptaxial silicon thickness of bulk substrate in a 5 μm pitch pixel array with 8 μm epitaxial silicon is nearly 3.7 μm. Second, the spatial resolutioin scales linearly with the pixel pitch, down to at least 3 μm, despite that diffusion is the dominating mechanism. Third, an optimum diode area should maximize signal-to-noise ratio. For 5 μm pitch pixels build on 8 μm epitiaxial silicon, the optimum diode area is around 1 μm2, smaller than the minimum diode area allowed by the design rule in 0.25 μm CMOS process. Fourth, epitaxial layer also plays an important role in determining the spatial resolution and signal-to-noise ratio of the sensor array. As compared to diode directly built upon bulk substrate, an 8 μm epitaxial layer leads to about 2.5 time increase in signal strength at the peak pixel. Due to substrate contribution, optimum eptaxial silicon may be ~ 4 μm. Finally, Monte Carlo method allows us to analyze the impact of the energy of incident electrons. While the spatial resolution and energy dependence is negligible for electron energy ranging from 200 keV to 1000 keV, incident electrons with lower energy tend to generate more ionization electrons in silicon with given thickness, leading to higher signal-to-noise ratio. However, lower energy electrons may cause more back-scattering in

the substrate, a detrimental effect that should be minimized and a possible solution is to thin the chip down to ~ 30 μm.

Some comments and suggestions on design optimization:

1) A design optimized for spatial resolution would have a narrow pixel pitch of 3~5 μm, a thin epitaxial layer of roughly 4 μm thickness, and the largest diodes that can fit in the pixels.

2) In contrast, a design optimized for highest signal to noise ratio would have a moderately-small pitch of 5~10 μm to prevent excessive recombination, the smallest possible stray capacitance associated with reset and readout electronics, and an optimal diode size that depends heavily on other parameters but is generally also quite small; perhaps 1 μm2, and a thicker epi that is perhaps two to three times as thick as the pixel pitch.

3) Certain applications may seek a design that is optimized for larger pixels, e.g., where high spatial resolution is not required and to reduce readout time. Recombination becomes a serious issue, and techniques to combine multiple sub-pixels that are independently buffered for low diode-node capacitance should be examined.

Images of biological samples such as mouse muscle cells, catalase protein crystal, neuron's myelin sheath have bee successfully captured using EM3. Reasonable radiation tolerance has also been verified and stable long-term operation is possible with cooling and thermal annealing.

CHAPTER 6: DESIGN AND TESTING OF A ONE-MEGA PIXEL ANALOG READ-OUT PROTOTYPE AND A 560 × 460 PIXEL PROTOTYPE WITH PER-COLUMN ANALOG-TO-DIGITAL CONVERSION

Initial success on the modeling, design and analysis of the first three generations of prototypes provides direct and hard evidence that epitaxial silicon active pixel sensor technology can be used for directly electron detection and imaging. To further explore the potential of this direct detection technology, more sophisticated chips with greater pixel counts and high speed read-out are presented in this chapter.

6.1 EM4 – A One-mega Pixel Prototype

The images obtained from EM3 have been encouraging; however, the relative small number of pixel counts limits its applicability. In order to obtain a full view of a biological structure, many individual EM3 images have to be collected and then join together using tomography techniques[64]. In addition, an adequately large number of pixels counts are necessary to perform a direct comparison with CCD camera which typically has 4000 × 4000 pixels for electron microscopy applications. As such, we expand the design of EM3 into a one-mega pixel fourth generation (EM4).

6.1.1 EM4 Design

A 4th generation APS chip (EM4) has been designed, fabricated, and tested. EM4 consists of 1024 × 1024 pixels and is implemented very similar to EM3. EM4 is organized into 16 identical sectors with 64 × 1024 pixel each. Each sector has its own

column multiplexing circuits, unity gain buffer output, and biasing circuits. The pixel pitch is 5 μm and the entire area of the chip is 5540 μm × 5510 μm. The block diagram of EM4 is shown in Figure 6.1.

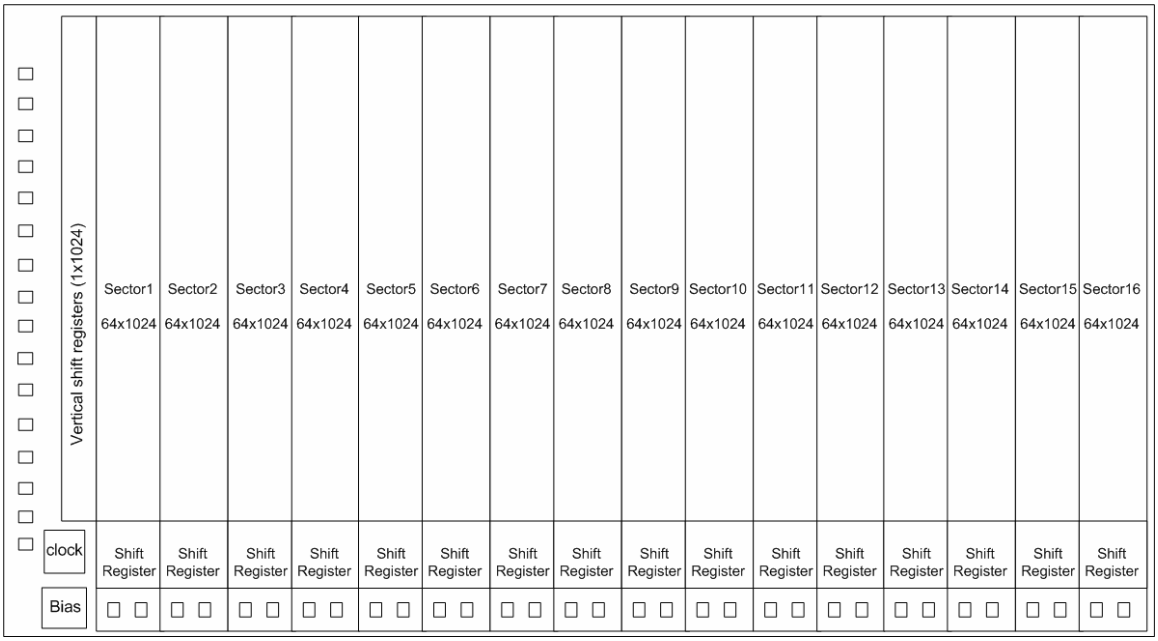

Figure 6.1: Block diagram of EM4, a 16 parallel analog readout one-mega pixel chip.

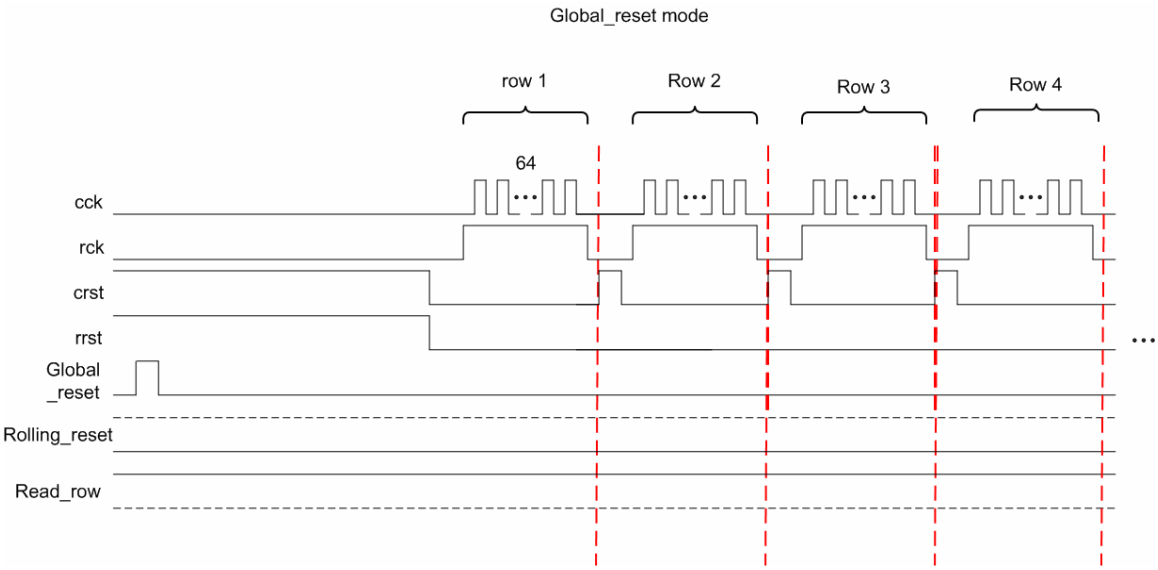

Figure 6.2: EM4 global reset mode timing diagram.

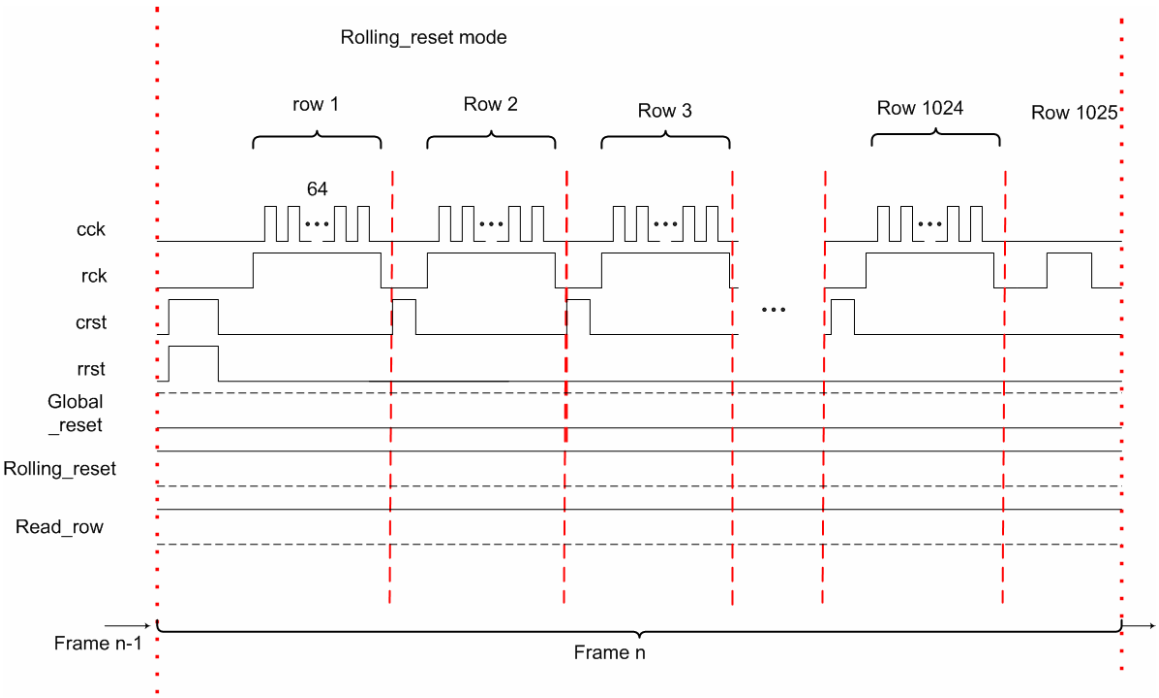

Figure 6.3: EM4 rolling reset mode timing diagram. The (n-1)th row is reset while reading the nth row.

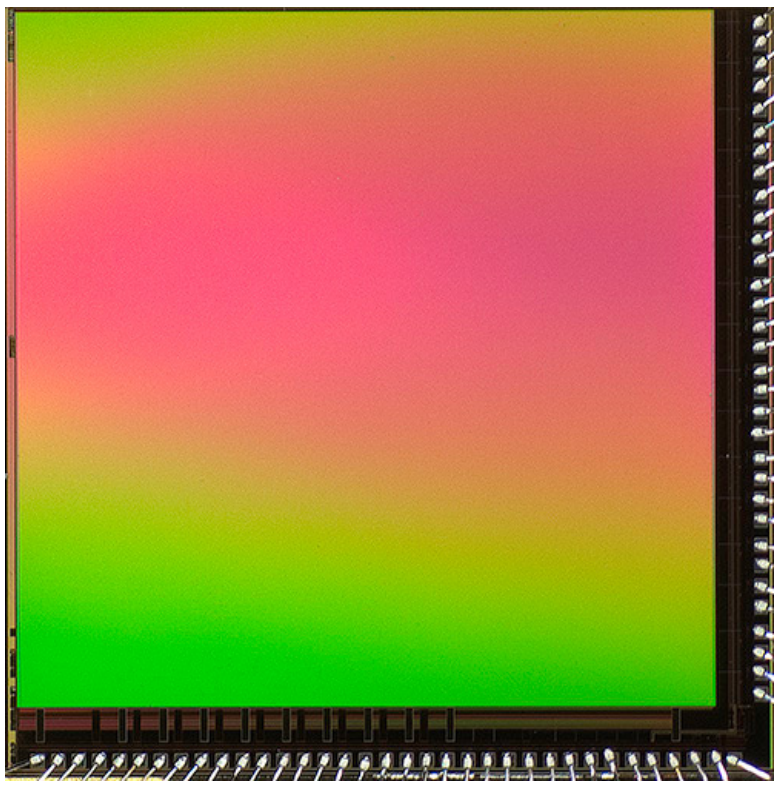

Figure 6.4: EM4 Die photo.

EM4 allows two modes of operation: global-reset mode and rolling-reset. The timing diagrams are shown in Figure 6.2 and Figure 6.3, respectively. The die photo of EM4 is shown in Figure 6.4.

6.1.2 EM4 Testing and Measurement

EM4 has been mounted onto an SSM CPG 13226[**] ceramic leadless chip carrier with a cavity in the center. EM4 responds to optical, X-ray, and high energy electron in similar way as EM3. With one million pixels, a direct comparison with CCD camera is possible. Shown in Figure 6.5 is the t-tubule and z-lines in a muscle cardiac cell. Figure 6.5 (a) was taken with EM4 and Figure 6.5 (a) was taken with a 4k by 4k CCD camera under the same imaging conditions for the same sample area in the cardiac cell. The EM4 image is the sum of 200 frames after CDS. The images were taken using 200 keV electrons and the magnification factor is 5,000. The integration time per frame is 100 ms and the corresponding dosage is ~ 0.125 e/pixel/frame (~ 0.8 pA/cm^2 in current density). The contrast between EM4 and the CCD becomes obvious if we look at the zoom-in view shown in Figure 6.6 (a) and (b). The fine structures in both figures are the gold nanoparticle alignment markers (~ 10 nm in diameter). EM4 image clearly resolves these nanoparticles but they are corrupted in the CCD image. The improvement in spatial resolution is at least nine times. More detailed comparison is still ongoing. And test chips of the fourth generation prototype have been installed in electron microscopes in NCMIR to study biological structures that are of practical significance.

[**] Supplied by Sepectrum-semi.com

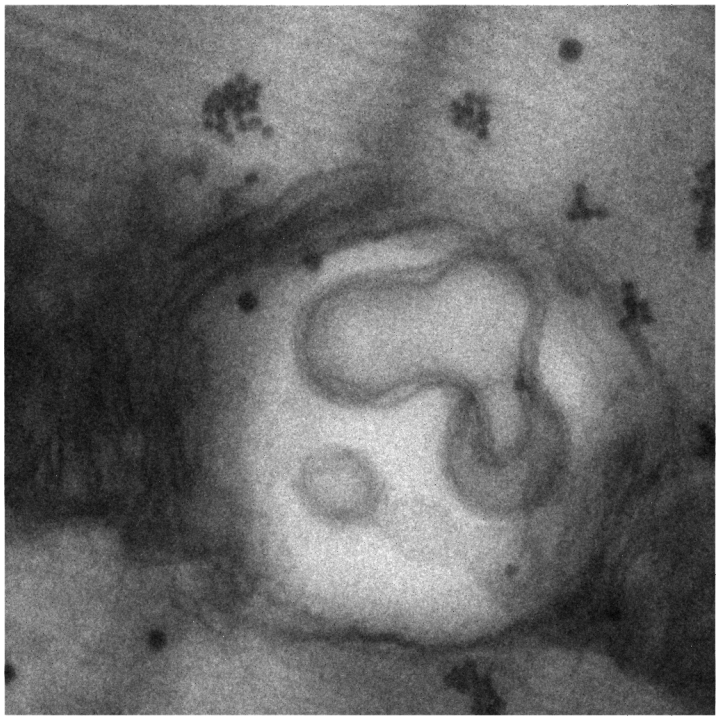

(a)

(b)

Figure 6.5: Image shown part of a mouse cardiac cell, electron beam energy = 200 keV, magnification = 5,000. (a) EM4 image, (b) CCD image.

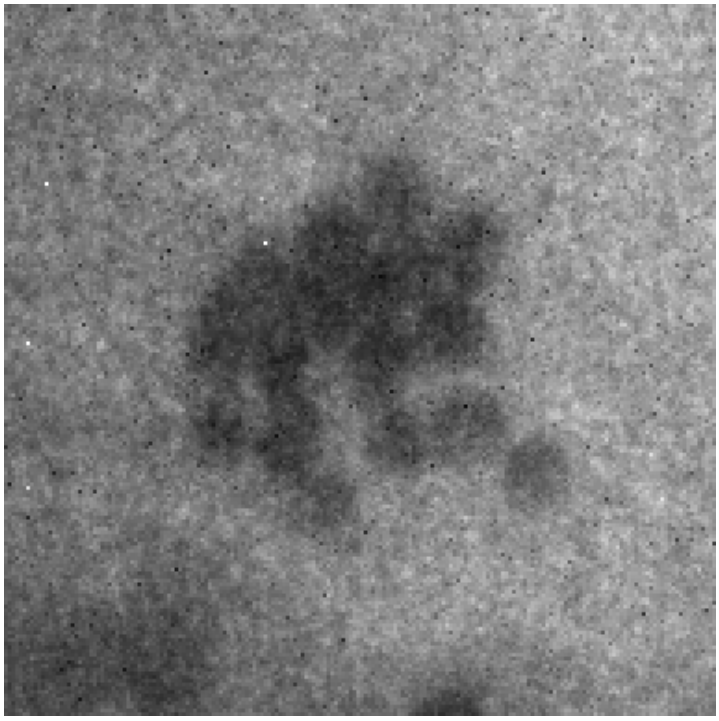

(a)

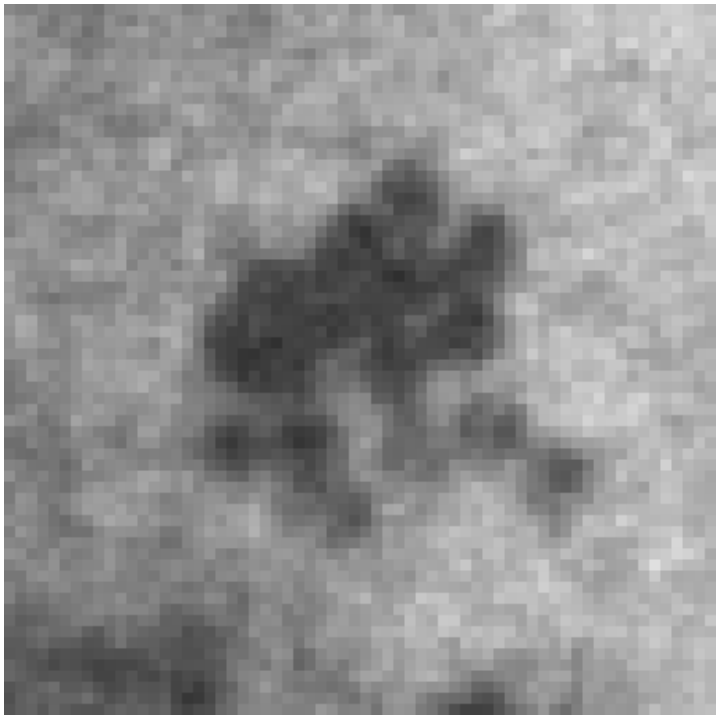

(b)

Figure 6.6: Zoom-in view of several gold nanoparticles (~ 10 nm in diameter) in Figure 6.5. (a) EM4 image, (b) CCD image.

6.2 EM5 – A 560 × 460 Pixel Chip with Per-column Analog-to-digital Conversion

On-chip analog-to-digital conversion has been implemented in almost all commercial optical image sensors to allow high speed readout and on-chip digital signal processing[65]. In EM5, analog-to-digital conversion is implemented at the column level, together with noise-cancellation and programmable gain amplification circuits.

6.2.1 EM5 Design

The block diagram of EM5 is shown in Figure 6.7. The pixel array consists of 560 by 460 pixels with a 5 μm pixel pitch a 2.5 μm wide diode. The read-out of signals from pixel array is accomplished through two identical read-out blocks distributed on two sides of the pixel array. The bottom block reads out pixels in the odd columns and the top block reads out pixels in the even columns. As such, the column read-out circuits can be made 10 μm wide – twice the pixel pitch. Major components implemented in each column read-out sub-block include the biasing circuit, programmable gain amplifier (PGA), sample and hold, 10-bit gray code counter, and 10-bit single-slope analog-to-digital converter.

Single-slope analog-to-digital converter is adopted in this chip because of its compactness in silicon area and low power consumption and can thus be implemented at column level. Other popular data converter architectures for CMOS image sensors include chip-level high precision and high speed pipeline analog-to-digital converters[66].

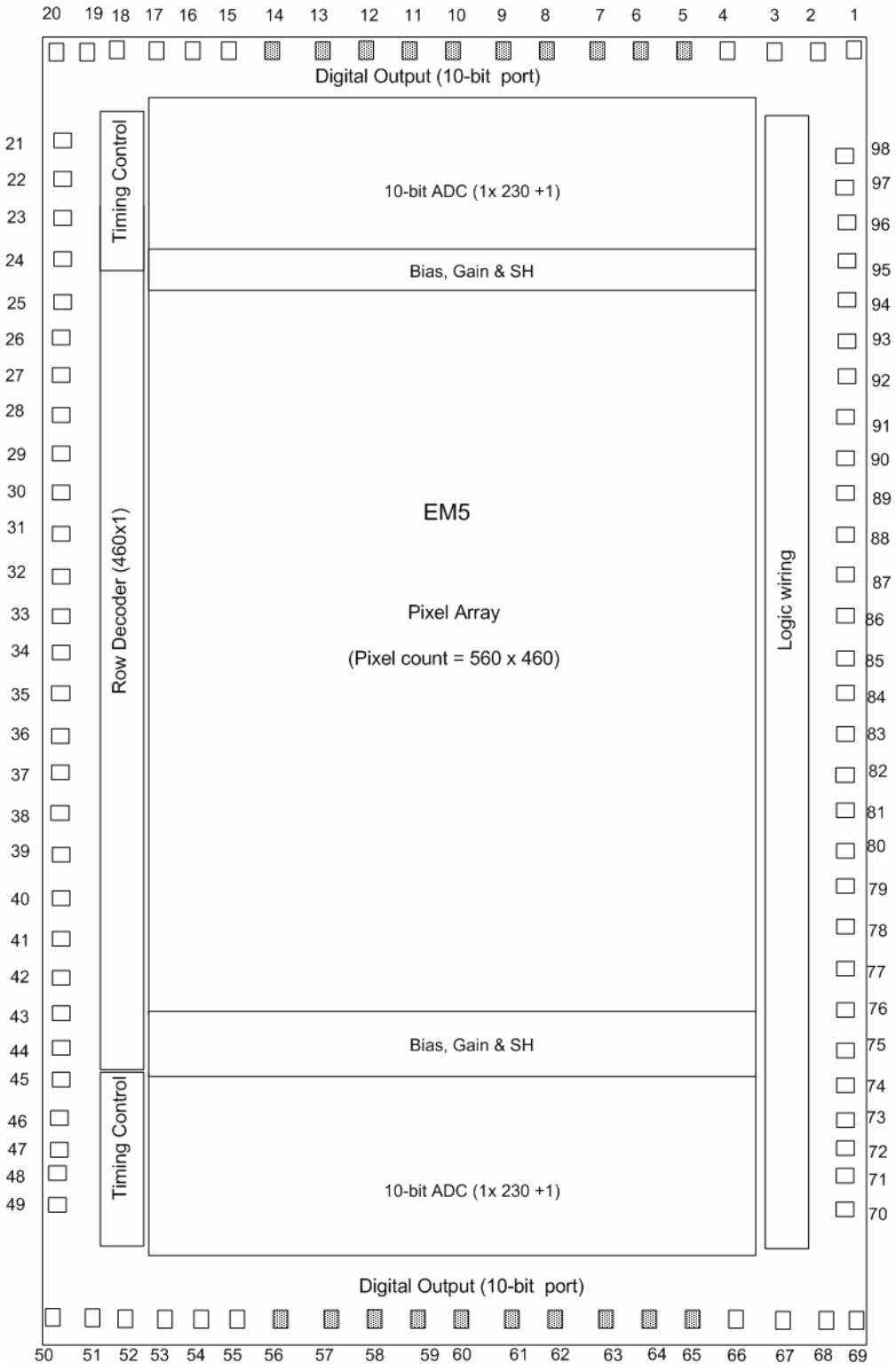

Figure 6.7: EM5 block diagram. Major components implemented in each column read-out sub-block include the biasing circuit, PGA, sample and hold, 10-bit gray code counter, and 10-bit single-slope analog-to-digital converter.

Programmable gain amplifier is implemented using a switch-capacitor amplifier as shown in Figure 6.8. The input sampling switch sc is connected to a column output wire. C_{in} is the input sampling capacitor and is connected to the positive input node of an op amp. Signal amplification is realized by closing switch sg and controlling the feedback fact -- the ratio of cg to cf. The operation of programmable gain amplifier is a two-step process:

1) reset phase

At time t_0, sc is closed and the bottom plate of cin is connected to the column line which carries the pixel signal after integration. With switches s2, s1, and s3 closed and s4 open, V_{ref} is applied to inp and bcf. Considering an op amp offset voltage V_{os}, the voltage level at inn and out is simply $V_{ref} + V_{os}$ and the offset voltage is stored across the feedback capacitor cf and cancelled out.

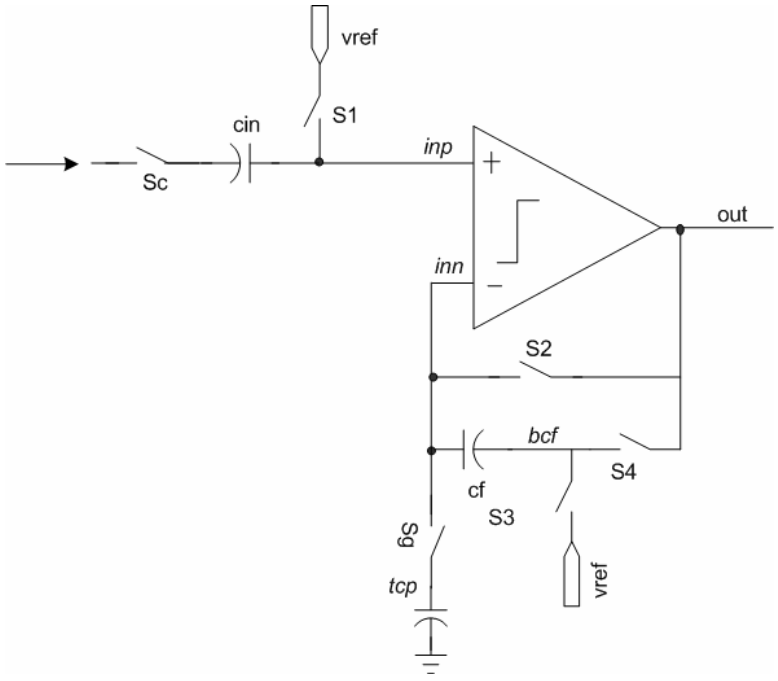

Figure 6.8: EM5 PGA Circuit Diagram

2) amplification phase

After time Δt, PGA reset phase completes and switch s2 turns off first, followed by s1 and s3. The charge injected by s1, s2, and s3 is independent of the input level. Then switch s4 turns on and a capacitive feedback loop formed between inn and out. Next, the pixel is reset and the voltage jump is applied to the bottom plate of cin, leading to a voltage jump at out. After V_{out} settles, the voltage signal passes to the next stage and be digitized.

$$A_v(\Delta V_{in} - \Delta V_{inn}) = \Delta V_{out} \tag{6.1}$$

and

$$\frac{\Delta V_{out}}{\Delta V_{inn}} = \frac{c_g + c_f}{c_f} \tag{6.2}$$

thus

$$\frac{\Delta V_{out}}{\Delta V_{in}} = \frac{1}{\frac{1}{A} + \frac{c_f}{c_g + c_f}} = \frac{c_g + c_f}{\frac{c_g + c_f}{A} + c_f} = \frac{\frac{c_g}{c_f} + 1}{1 + \frac{1}{A} + \frac{1}{A}\frac{c_g}{c_f}} \approx 1 + \frac{c_g}{c_f} \tag{6.3}$$

As such, the difference between the pixel level after integration and reset level is read out directly and the fixed pattern noise is subtracted automatically. However, because the integration level carries the noise due to the previous reset which is uncorrelated to the immediate reset after the PGA reset phase, this scheme doubles the kTC noise{Kleinfelder, 2004 #279;Chen, 2004 #220}. The advantage is that only one digitization is needed and it is faster than obtaining real signal by conventional off-chip subtraction of two consecutive reads (one for reset level, and a second for signal after

integration). Bottom-plating sampling minimizes the capacitance at the input of the op amp and reduces the injection of substrate noise into the op amp [69].

The circuit diagram of the column level single slope analog-to-digital converter is shown in Figure 6.9 and its operation is divided into four phases: reset, ramp, latch, and read-out.

1) Reset Phase:

Circuit reset is accomplished by setting setb at high. Reset phase has to be properly aligned with grey code counter reset and PGA operation.

2) Ramp Phase:

At time zero, Vin, the pixel signal processed by the PGA is sampled into the sample/hold stage and applied to the negative input node of the comparator. And a 10-bit grey code counter starts counting from 0 to 1024 and the counter output is written into the 10-bit memory built in each column. A synchronized ramp circuit creates a voltage at the positive node of the comparator rises from Vmin to Vmax.

3) Latch Phase:

When the ramp voltage matches that of the negative node, the comparator switches and activates LDB and LD to latch the digital values written into the 10-bit memory and counter output is detached from the memory. Apparently, the time instance at which locking occurs depends on the pixel signal at each column. It takes longer time to reach a larger input value and the digital value locked is larger as well. Therefore, the gray code output locked in the memory is then a digital representation of the pixel signal applied to the negative input of the comparator.

$$dout_{gray} = \frac{V_{in} - V_{\min}}{V_{\max} - V_{\min}} \cdot 1024_{gray} \tag{6.4}$$

4) Read-out Phase:

Upon the conclusion of ramp signal reaches Vmax and counter reaches 1024, analog to digital conversion completes and resetb switches to high and the comparator is detached from the memory. The memory in each column can then be read-out sequentially.

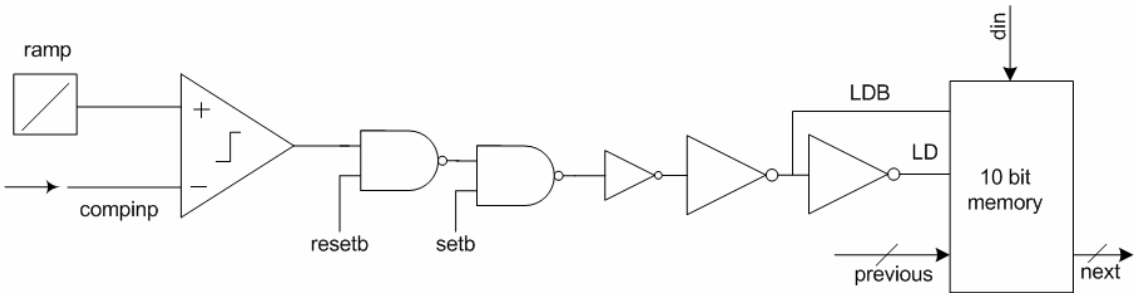

Figure 6.9: EM5 Single-slope ADC Circuit Diagram.

Built-in control circuits allow EM5 to function as both digital still camera and video camera. The timing diagrams of four typical operation modes are shown in Figure 6. 10.

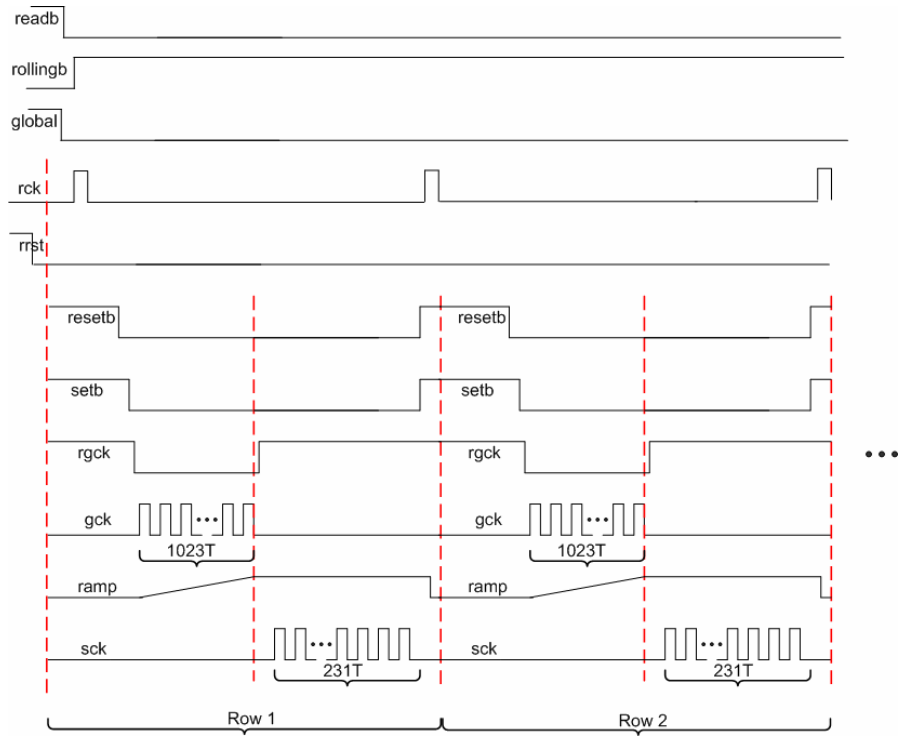

(a)

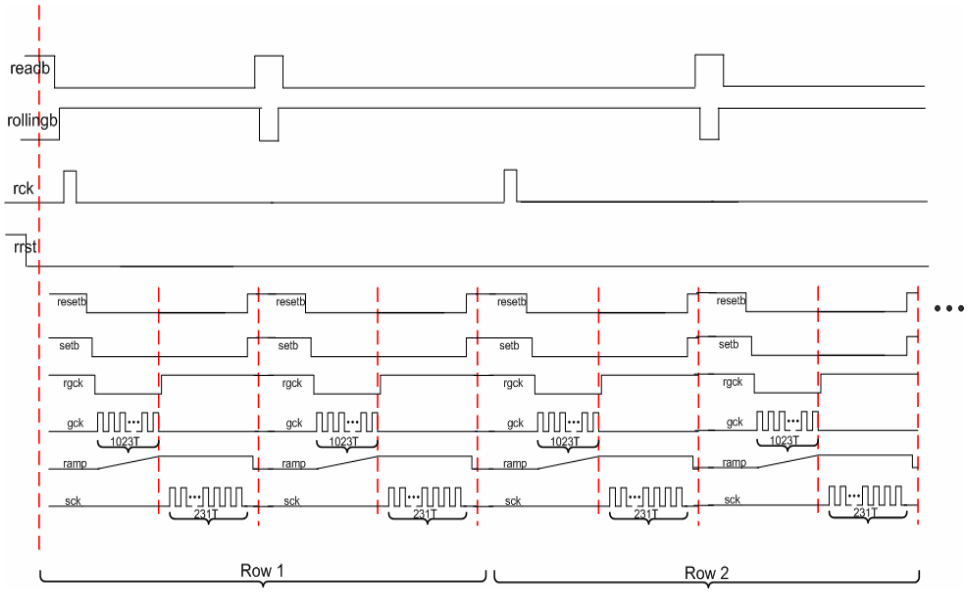
readb
rollingb
rck
rrst
resetb
setb
rgck
gck
1023T
ramp
sck
231T
Row 1
Row 2

(b)

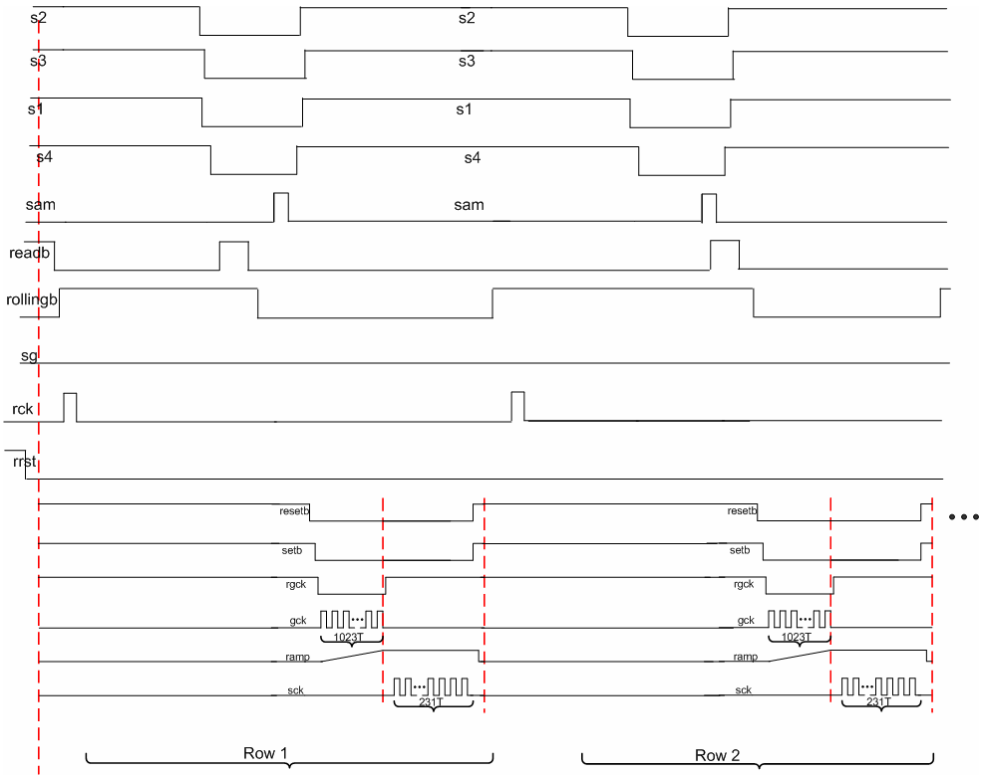
s2
s3
s1
s4
sam
readb
rollingb
sg
rck
rrst
resetb
setb
rgck
gck
1023T
ramp
sck
231T
Row 1
Row 2

(c)

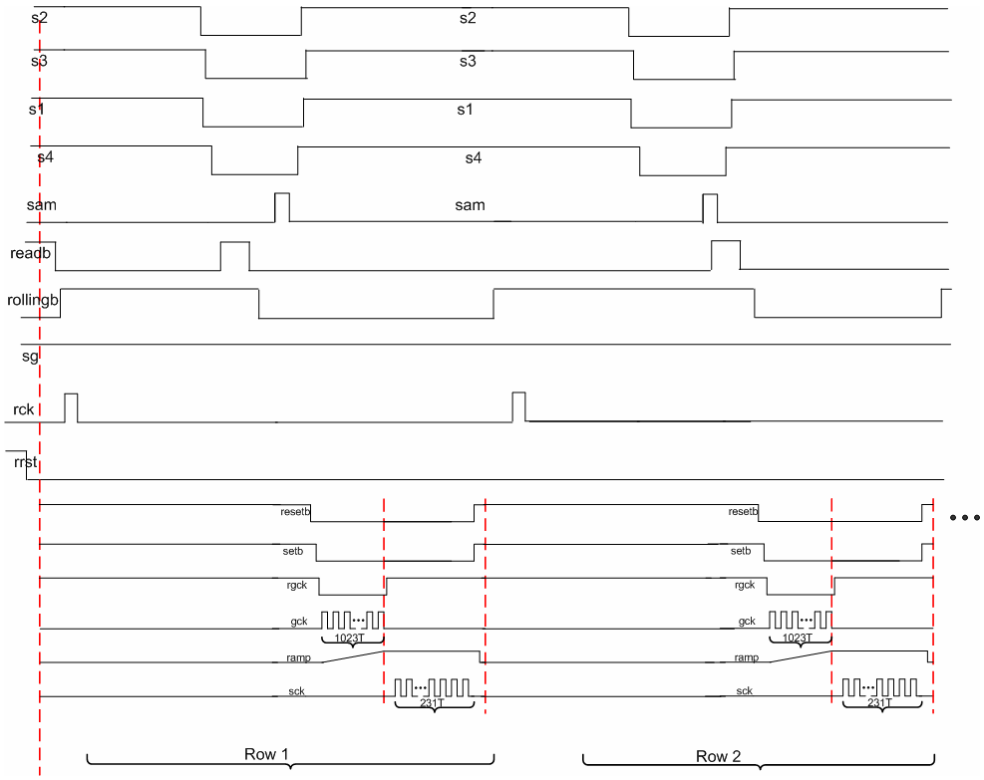

(d)

Figure 6.10: EM5 Timing diagram. (a) UGB-global reset mode, (b) UGB-rolling reset mode, (c) PGA-global reset mode, (d) PGA-rolling reset mode.

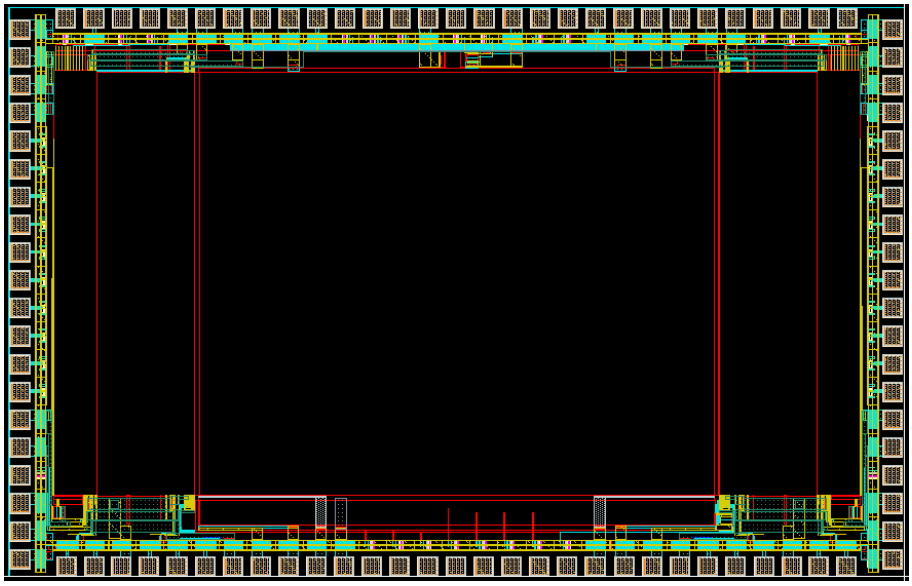

Figure 6.11: EM5 layout in Cadence.

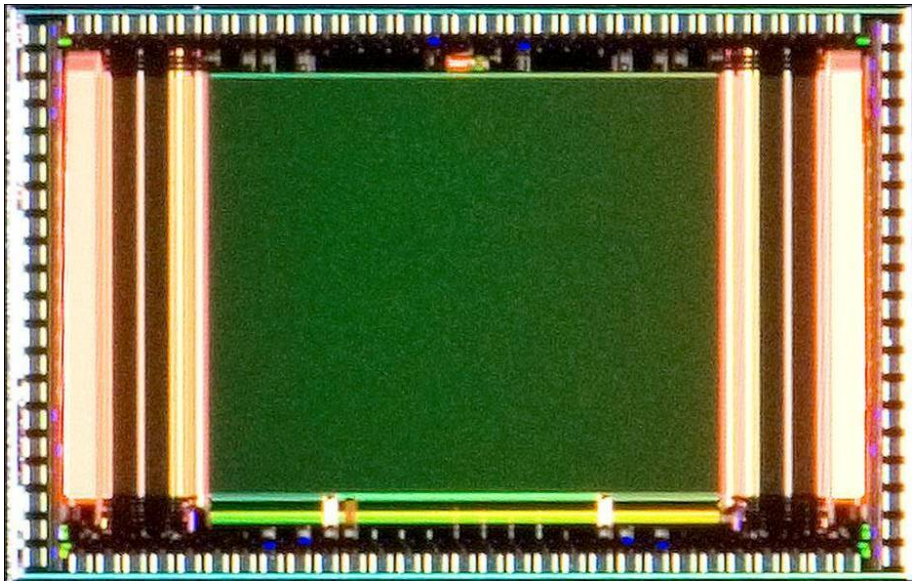

Figure 6.12: EM5 Die Photo

The layout of EM5 is depicted in Figure 6.11 and the die photo is shown in Figure 6.12. There are 98 bonding pads for this chip and total silicon area is 15 mm^2.

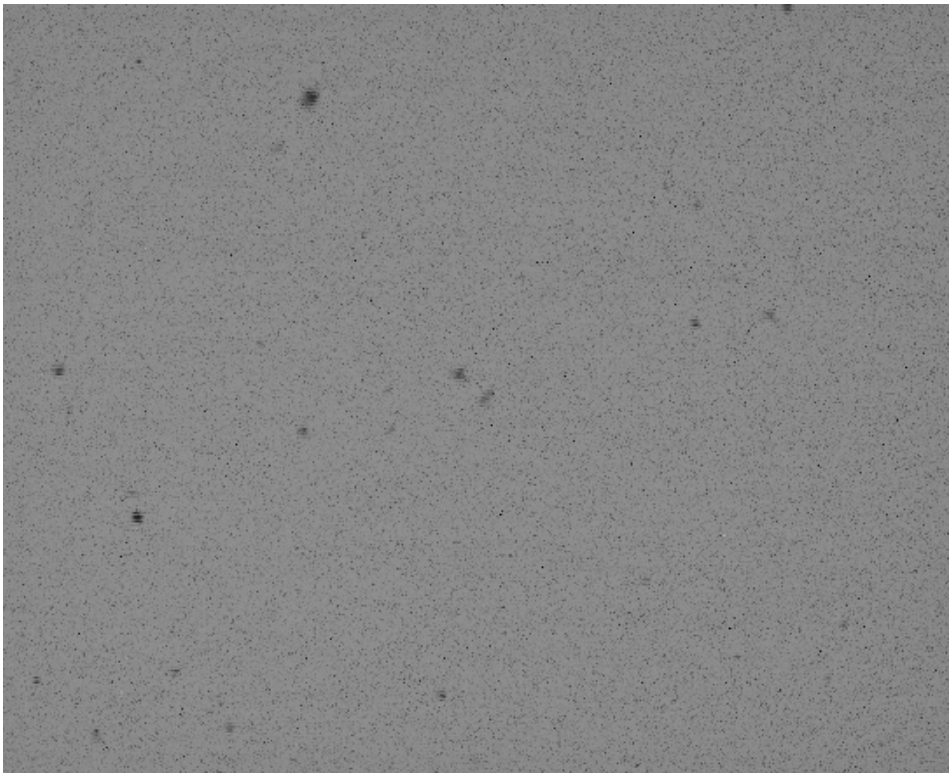

Figure 6.13: Image of a few dust particles using EM5 under visible light.

6.2.3 EM5 Testing and Measurement

EM5 has been package in CPG13226 package and initial testing has confirmed that this chip is working. An image of dust particles taking using EM5 under visible light is shown in Figure 6.13.

6.3 Summary

A fourth generation (EM4) analog read-out chip with one million pixels and a fifth generation (EM5) digital read-out chips with 560 by 460 pixels have been designed, fabricated, and tested. EM4 has been put into direct comparison with CCD cameras under the same condition. EM4 outperforms the later by at least nine times in spatial resolution. EM5 features per-column 10-bit integration mode analog-to-digital conversion and allows massively parallel read-out. Preliminary tests of EM5 have confirmed the basic functionality and several rudimentary images have been successfully captured.

CHAPTER 7: CONCLUSION

Via a combination of Monte Carlo simulation and experimental design and testing, this dissertation has proposed and successfully demonstrated a novel charged-particle imaging technology based on epitaxial silicon APS arrays.

First, in coping with the stochastic nature of ionization generation and charge transport in silicon, a Monte Carlo model from first principles has been developed following Einstein's formulism of Brownian motion. It directly models ionization generation using exponential random numbers and Bichsel random numbers for X-ray photons and high energy electrons, respectively. Movement of individual ionization electrons is initialized and tracked using a Monte Carlo algorithm implemented in C++ and Matlab, yielding a collection matrix for each impinging particle. Three generations of prototype chips including: EM1 (diode area test chip), EM2 (pixel pitch test chip), and EM3 (a 560 by 550 pixel analog read-out chip) are designed, fabricated, tested, and compared with the simulation.

Second, Monte Carlo simulation has been applied to study sensor array response to ^{55}Fe 5.9 keV X-ray photons and compared with experimental measurement. Monte Carlo simulation reveals that X-ray events occurr in p-substrate can still lead to significant ionization electron collection, in particular, for those near the boundary between bulk substrate and epitaxial layer. The reason is two-fold: 1) the recombination rate in p-substrate is finite, although much higher than that of the p-epitaxial layer, 2) the electrical

potential of the p-epitaxial layer is lower than that of the p-substrate and no barriers exist for electrons to enter into the p-epitaxial region from the p-substrate. On the other hand, ionization electrons originate from deep in silicon add to the signal intensity but result in more severe lateral diffusion. Both simulation and measurement identify that the smaller the pixel pitch, the higher the spatial resolution. Recombination loss of ionization electrons becomes noticeable when the pitch is greater than 10 μm. Simulation results agree with the measurement remarkably well when substrate contribution is properly accounted.

Third, sensor array response to high energy electrons is systematically studied focusing on spatial resolution and signal-to-noise ratio. Incident high energy electrons inevitably generate many ionization electrons in the bulk substrate. Due to finite substrate recombination rate, these ionization electrons add to the collection profile of each incident particle. Substrate contribution is quantified by fitting the simulated histogram of ionization electrons collected to the theoretical Bichsel distribution. The substrate contribution is found to be equivalent to ~ 3.7 μm epitaxial silicon for 5 μm pitch APS array built on an 8 μm thick nominal epitaxial silicon layer. We find the spatial resolution scales linear with pixel pitch down to at least 3 μm, despite that diffusion is the dominating transport mechanism. For the effect of diode area, a larger diode collects more ionization electrons per incident particle, however, there is a concomitant increase in noise electrons that can swamp the increased signal. The optimum diode area achieving a maximum signal-to-noise ratio requires a rather small diode area, about 1 μm^2 for our 5 μm pitch pixel array built on top of 8 μm epitaxial layer. For the effect of

epitaxial layer, our simulation shows that 8 μm epitaxial layer leads to about 2.5 times improvement in signal intensity than without epitaxial layer. While a thicker epitaxial layer enhances signal strength, lateral diffusion of ionization electrons from deepr epitaxial silicon compromises the spatial resolution. When the bulk substrate contribution is considered, the optimum epitaxial silicon thickness may be ~ 4 μm for 5 μm pitch pixel array. The effect of incident electron energy is also studied. Simulation results show lower energy incident electrons tend to have higher signal-to-noise ratio due to increased likelihood in generating more ionization electrons per incident particle. While the energy dependence of sensor array spatial resolution is negligible, lower energy incident electrons are more likely to experience backscattering, a severe detrimental effect for charged-particle imaging. Built on the insights gained from these simulation results and measurement, we have successfully captured high resolution images of biological samples such as neuron's myelin sheath and mouse muscle cells have been successfully using EM3, a breakthrough in digital imaging in electron microscopy.

Lastly, a fourth generation (EM4) analog read-out chip with one million pixels and a fifth generation (EM5) digital read-out chips with 560 by 460 pixels have been designed, fabricated, and tested. EM4 has been put into direct comparison with CCD cameras under the same condition. EM4 outperforms the later by at least nine times in spatial resolution. EM5 features per-column 10-bit integration mode analog-to-digital conversion and allows massively parallel read-out. Preliminary tests of EM5 have confirmed the basic functionality and several rudimentary images have been successfully captured.

The Monte Carlo model developed in this dissertation research can be applied to many other applications involving charged-particle detection and imaging. Continued work will lead to a new generation sensor chip with 4k by 4k pixels and on-chip analog-to-digital conversion and noise reduction, ready to tackle the structures of various proteins and viruses.

APPENDIX A: TESTING INSTRUMENTS

The following instruments at the University of California, Irvine are used for testing of the prototype chips presented in this dissertation:

Agilent:

1) 81110A 165/330MHz Pulse/Pattern Generator
2) 3458A 8 ½ Digit Multimeter
3) 1682AD Logic Analyzer
4) Infiniium 54833D MSO 1GHz, 4GSa/s Oscilloscope
5) 33220A 20 MHz Function/Arbitrary Waveform Generator
6) E3610A DC Power Supply
7) 34411A 6 ½ Digit Multimeter

Tektronix:

1) DG2020A Data Generator 200 Mbps
2) P3420 Variable Output Pad
3) ADA 400A Differential Preamplifier
4) TDS3034B Four Channel Color Digital Phosphor Oscilloscope

Newport:

1) Optical Bench

Tenma:

1) Laboratory DC Power Supply 72-2005

Dolan-Jenner:

1) Fiber-Lite Fiber Opti Illuminator Model 190

BIBLIOGRAPHY

[1] J. Frank, *Three-Dimensional Electron Microscopy of Macromolecular Assemblies*. San Diego, CA: Academic Press, 1996.

[2] B. Bottcher, S. A. Wynne, and R. A. Crowther, "Determination of the Fold of the Core Protein of Hepatitis B Virus ky Electron Cryomicroscopy," *Nature*, vol. 386, pp. 88-91, 1997.

[3] S. Subramaniam and J. L. S. Milne, "Three-dimensional Electron Microscopy at Molecular Resolution," *Annual Review of Biophysics and Biomolecular Structure*, vol. 33, pp. 141-155, 2004.

[4] Research Collaboratory for Structural Bioinformatics, "PDB Statistics," http://www.rcsb.org/pdb/home/home.do, 2007.

[5] J. Norvell and J. M. Berg, "The Protein Structure Initiative, Five years later," *Scientist*, vol. 19, pp. 30-31, 2005.

[6] N. H. Xuong, A. C. Miazza, P. Leblanc, F. Duttweiler, J. C. Bouwer, S. Peltier, M. Ellisman, P. Denes, F. Bieser, H. S. Matis, H. Wieman, and S. Kleinfelder, "First Use of A High-sensitivity Active Pixel Sensor Array as A Detector for Electron Microscopy," presented at SPIE, 2004.

[7] P. A. Thuman-Commike and W. Chiu, "Reconstruction Principles of Icosahedral Virus Structure Determination Using Electron Cryomicroscopy," *Micron*, vol. 31, pp. 687-711, 2000.

[8] Y. Liang, J. Jakana, X.-K. Yu, J.-Q. Zhang, W. Chiu, and Z. H. Zhou, "High-Resolution 3D Reconstruction of Cytoplasmic Polyhedrosis Virus," *Microscopy and Microanalysis*, vol. 9 (Suppl 2), 2003.

[9] M. Halic, M. Gartmann, O. Schlenker, T. Mielke, M. R. Pool, I. Sinning, and R. Beckmann, "Signal Recognition Particle Receptor Exposes the Ribosomal Translocon Binding Site," *Science*, vol. 312, pp. 745-747, 2006.

[10] A. C. Milazzo, P. Leblanc, F. Duttweiler, L. Jin, J. C. Bouwer, S. Peltier, M. Ellisman, F. Bieser, H. S. Matis, H. Wieman, P. Denes, S. Kleinfelder, and N. H. Xuong, "Active Pixel Sensor Array as a Detector for Electron Microscopy," *Ultramicroscopy*, vol. 104, pp. 152-159, 2005.

[11] H. S. Matis, F. Bieser, S. Kleinfelder, G. Rai, F. Retiere, H. G. Ritter, K. Singh, S. E. Wurzel, H. Wieman, and E. Yamamoto, "Charged Particle Detection Using a CMOS Active Pixel Sensor," *IEEE Transactions on Nuclear Science*, vol. 50, pp. 1020-1025, 2003.

[12] Synopsis, "ISE TCAD Release 10.0 Manual," 2004, pp. Integrated Systems Engineering.

[13] R. A. Smith, *Semiconductors*, Second ed: Combridge University Press, 1978.

[14] S. M. Sze, *Physics of Semiconductor Devices*, second ed: John Wiley & Sons, Inc, 1981.

[15] N. Tsoulfanidis, *Measurement and Detection of Radiation*: McGRAW-HILL Series in Nuclear Engineering, 1983.

[16] J. R. Janesick, *Scientific Charge-Coupled Devices*: SPIE Press, 2001.

[17] H. Bichsel, "Straggling in Thin Silicon Detectors," *Review in Modern Physics*, vol. 60, pp. 663, 1988.
[18] B. Dierikx, G. Meynants, and D. Scheffer, "Near 100% fill factor CMOS active pixels," presented at 1997 IEEE Workshop on CCD's and Advanced Image Sensors, Brugge, Belgium, 1997.
[19] D. Levy, S. E. Schacham, and I. Kidron, "3-Dimensional Analytical Simulation of Self-Responsivities and Cross-Responsivities of Photovoltaic Detector Arrays," *IEEE Transactions on Electron Devices*, vol. 34, pp. 2059-2070, 1987.
[20] D. Levy and S. E. Schacham, "3-Dimensional Excess Carrier Distribution in Semiconductor Imaging Arrays," *Journal of Applied Physics*, vol. 64, pp. 5230-5233, 1988.
[21] J. S. Lee, R. I. Hornsey, and D. Renshaw, "Analysis of CMOS photodiodes - Part II: Lateral photoresponse," *IEEE Transactions on Electron Devices*, vol. 50, pp. 1239-1245, 2003.
[22] H. Holloway, "Collection Efficiency and Crosstalk in Closely Spaced Photodiode Arrays," *Journal of Applied Physics*, vol. 60, pp. 1091-1096, 1986.
[23] C. S. S. Lin, B. P. Mathur, and M. C. F. Chang, "Analytical Charge Collection and MTF Model for Photodiode-based CMOS Imagers," *IEEE Transactions on Electron Devices*, vol. 49, pp. 754-761, 2002.
[24] X. Belredon, J. P. David, D. Lewis, T. Beauchene, V. Pouget, S. Barde, and P. Magnan, "Heavy Ion-induced Charge Collection Mechanisms in CMOS Active Pixel Sensor," *IEEE Transactions on Nuclear Science*, vol. 49, pp. 2836-2843, 2002.
[25] G. Deptuch, M. Winter, W. Dulinski, D. Husson, R. Turchetta, and J. L. Riester, "Simulation and Measurements of Charge Collection in Monolithic Active Pixel Sensors," *Nuclear Instruments & Methods in Physics Research Section A-Accelerators Spectrometers Detectors and Associated Equipment*, vol. 465, pp. 92-100, 2001.
[26] J. P. Lavine, E. A. Trabka, B. C. Burkey, T. J. Tredwell, E. T. Nelson, and C. Anagnostopoulos, "Steady-State Photocarrier Collection in Silicon Imaging Devices," *IEEE Transactions on Electron Devices*, vol. 30, pp. 1123-1134, 1983.
[27] G. A. Saihalasz and M. R. Wordeman, "Monte-Carlo Modeling of the Transport of Ionizing-Radiation Created Carriers in Integrated-Circuits," *Electron Device Letters*, vol. 1, pp. 211-213, 1980.
[28] J. P. Lavine, W. C. Chang, C. N. Anagnostopoulos, B. C. Burkey, and E. T. Nelson, "Monte-Carlo Simulation of the Photoelectron Crosstalk in Silicon Imaging Devices," *IEEE Transactions on Electron Devices*, vol. 32, pp. 2087-2091, 1985.
[29] C. C. Liebe, "Charged particle-induced noise in camera systems," *IEEE Transactions on Nuclear Science*, vol. 48, pp. 1541-1549, 2001.
[30] M. Kalos and P. A. Whitelock, *Monte Carlo Methods*, vol. I: John Wiley & Sons, 1986.
[31] J. Gentle, *Random Number Generation and Monte Carlo Methods*, 2nd ed: Springer, 2003.
[32] D. Joy, *Monte Carlo Modeling for Electron Microscopy and Microanalysis*: Oxford University Press, 1995.

[33] D. F. Hebbard and P. R. Wilson, "The Effect of Multiple Scattering on Electron energy Loss Distributions," *Australian J. Phys.*, vol. 8, pp. 90-97, 1955.
[34] J. Matthews and R. L. Walker, *Mathematical Methods of Physics*, vol. Second: W.A. Benjamin, Inc., 1970.
[35] A. Leon-Garcia, *Probability and Random Processes for Electrical Engineering*, 2nd ed: Prentice Hall, 1993.
[36] D. Duffy, *Introduction to C++ for Financial Engineers: An Object-Oriented Approach*: Wiley, 2006.
[37] G. Deptuch, "New Generation of Monolithic Active Pixel Sensors for Charged Particle Detection," PhD Dissertation, in *Department of Electronics*: France, 2002, pp. 318.
[38] G. Deptuch, "Tritium Autoradiography with Thinned and Back-side Illuminated Monolithic Active Pixel Sensor Device," *Nuclear Instruments & Methods in Physics Research Section A-Accelerators Spectrometers Detectors and Associated Equipment*, vol. 543, pp. 537-548, 2005.
[39] L. Landau, "On the Energy Loss of Fast Particles by Ionization," *Journal of Physics, USSR*, vol. 8, pp. 201, 1944.
[40] H. Bichsel and R. P. Saxon, "Comparison of Calculational Methods for Straggling in Thin Absorbers," *Physical Review A*, vol. 11, pp. 1286-1296, 1975.
[41] J. P. Perez, J. Sevely, and B. Jouffrey, "Straggling of Fast Electrons in Aluminum Foils Observed in High-Voltage Electron-Microscopy (0.3-1.2 Mv)," *Physical Review A*, vol. 16, pp. 1061-1069, 1977.
[42] H. Holloway, "Random-Walk Treatment of Carrier Diffusion with Surface Recombination," *Journal of Applied Physics*, vol. 62, pp. 3241-3243, 1987.
[43] D. K. Schroder, B. D. Choi, S. G. Kang, W. Ohashi, K. Kitahara, G. Opposits, T. Pavelka, and J. Benton, "Silicon Epitaxial Layer Recombination and Generation Lifetime Characterization," *IEEE Transactions on Electron Devices*, vol. 50, pp. 906-912, 2003.
[44] E. G. Stevens and J. P. Lavine, "An Analytical, Aperture, and 2-Layer Carrier Diffusion Mtf and Quantum Efficiency Model for Solid-State Image Sensors," *IEEE Transactions on Electron Devices*, vol. 41, pp. 1753-1760, 1994.
[45] S. E. Swirhun, Y.-H. Kwark, and R. M. Swanson, "Measurement of Electron Lifetime, Electron Mobility and Band-gap Narrowing in Heavily Doped p-type Silicon," presented at Electron Devices Meeting, 1986 International, 1986.
[46] S. E. Swirhun, J. A. Delalamo, and R. M. Swanson, "Measurement of Hole Mobility in Heavily Doped N-Type Silicon," *IEEE Electron Device Letters*, vol. 7, pp. 168-173, 1986.
[47] J. P. Lavine and E. K. Banghart, "The Effect of Potential Obstacles on Charge Transfer in Image Sensors," *IEEE Transactions on Electron Devices*, vol. 44, pp. 1593-1598, 1997.
[48] N. W. Ashcroft and M. N.D., *Solid State Physics*. New York: Holt, Rinehart and Winston, 1976.
[49] R. Turchetta, J. D. Berst, B. Casadei, G. Claus, C. Colledani, W. Dulinski, Y. Hu, D. Husson, J. P. Le Normand, J. L. Riester, G. Deptuch, U. Goerlach, S. Higueret, and M. Winter, "A Monolithic Active Pixel Sensor for Charged Particle Tracking and Imaging Using Standard VLSI CMOS Technology," *Nuclear Instruments &*

Methods in Physics Research Section A-Accelerators Spectrometers Detectors and Associated Equipment, vol. 458, pp. 677-689, 2001.

[50] S. Kleinfelder, S. D. Li, F. Bieser, R. Gareus, L. Greiner, J. King, J. Levesque, H. S. Matis, M. Oldenburg, H. G. Ritter, F. Retiere, A. Rose, K. Schweda, A. Shabetai, E. Sichtermann, J. H. Thomas, H. H. Wieman, and H. Bichsel, "A Proposed STAR Microvertex Detector Using Active Pixel Sensors (APS) with Some Relevant Studies on APS Performance," *Nuclear Instruments & Methods in Physics Research, A-Accelerators Spectrometers Detectors and Associated Equipment*, vol. 565, pp. 132-138, 2006.

[51] B. Razavi, *Design of Analog CMOS Integrated Circuits*: McGraw-Hill, 2001.

[52] G. W. Fraser, A. F. Abbey, A. Holland, K. McCarthy, A. Owens, and A. Wells, "The X-Ray-Energy Response of Silicon .A. Theory," *Nuclear Instruments & Methods in Physics Research Section a-Accelerators Spectrometers Detectors and Associated Equipment*, vol. 350, pp. 368-378, 1994.

[53] A. Owens, G. W. Fraser, A. F. Abbey, A. Holland, K. McCarthy, A. Keay, and A. Wells, "The X-ray Energy Response of Silicon .B. Measurements," *Nuclear Instruments & Methods in Physics Research Section A-Accelerators Spectrometers Detectors and Associated Equipment*, vol. 382, pp. 503-510, 1996.

[54] I. M. Bronshtein and B. S. Fraiman, "Determination of the Path Lengths of Slow Secondary Electrons," *Sov. Phys. Solid State*, vol. 3, pp. 1188-1197, 1961.

[55] G. Deptuch, J. D. Berst, G. Claus, C. Colledani, W. Dulinski, Y. Gornushkin, D. Husson, J. L. Riester, and M. Winter, "Design and Testing of Monolithic Active Pixel Sensors for Charged Particle Tracking," *IEEE Transactions on Nuclear Science*, vol. 49, pp. 601-610, 2002.

[56] S. Ross, *A First Course in Probability*, 7th ed: Prentice Hall, 2005.

[57] J. C. Pickel, A. H. Kalma, G. R. Hopkinson, and C. J. Marshall, "Radiation Effects on Photonic Imagers - A Historical Perspective," *IEEE Transactions on Nuclear Science*, vol. 50, pp. 671-688, 2003.

[58] J. Bogaerts and B. Dierickx, "Total Dose Effects on CMOS Active Pixel Sensors," presented at SPIE, 2000.

[59] J. R. Srour, C. J. Marshall, and P. W. Marshall, "Review of Displacement Damage Effects in Silicon Devices," *IEEE Transactions on Nuclear Science*, vol. 50, pp. 653-670, 2003.

[60] S. Kleinfelder, S. Lim, X. Q. Liu, and A. El Gamal, "A 10,000 frames/s CMOS Digital Pixel Sensor," *IEEE Journal of Solid-State Circuits*, vol. 36, pp. 2049-2059, 2001.

[61] W. J. Snoeys, T. A. P. Gutierrez, and G. Anelli, "A New NMOS Layout Structure for Radiation Tolerance," *IEEE Transactions on Nuclear Science*, vol. 49, pp. 1829-1833, 2002.

[62] M. Campbell, G. Anelli, M. Burns, E. Cantatore, L. Casagrande, M. Delmastro, R. Dinapoli, F. Faccio, E. Heijne, P. Jarron, M. Luptak, A. Marchioro, P. Martinengo, D. Minervini, M. Morel, E. Pernigotti, I. Ropotar, W. Snoeys, and K. Wyllie, "A Pixel Readout Chip for 10-30 MRad in Standard 0.25 um CMOS," *IEEE Transactions on Nuclear Science*, vol. 46, pp. 156-160, 1999.

[63] G. Anelli, M. Campbell, M. Delmastro, F. Faccio, S. Florian, A. Giraldo, E. Heijne, P. Jarron, K. Kloukinas, A. Marchioro, P. Moreira, and W. Snoeys,

"Radiation tolerant VLSI circuits in standard deep submicron CMOS technologies for the LHC experiments: Practical design aspects," *IEEE Transactions on Nuclear Science*, vol. 46, pp. 1690-1696, 1999.

[64] L. Jin, A. C. Milazzo, S. Kleinfelder, S. D. Li, P. Leblanc, F. Duttweiler, J. C. Bouwer, S. Peltier, M. Ellisman, and N. H. Xuong, "Applications of Direct Detection Device in Transmission Electron Microscopy," in *Journal of Structural Biology*, 2007, submitted.

[65] E. R. Fossum, "CMOS Image Sensors: Electronic Camera-on-a-chip," *IEEE Transactions on Electron Devices*, vol. 44, pp. 1689-1698, 1997.

[66] L. Kozlowski, G. Rossi, L. Blanquart, R. Marchesini, Y. Huang, G. Chow, and J. Richardson, "A Progressive 1920-1080 Imaging System-on-chip for HDTV Cameras," presented at 2005 IEEE International Solid-State Circuits Conference, Digest of Technical Papers, 2005.

[67] S. Kleinfelder, F. Bieser, Y. D. Chen, R. Gareus, H. S. Matis, M. Oldenburg, F. Retiere, H. G. Ritter, H. H. Wieman, and E. Yamamoto, "Novel Integrated CMOS Sensor Circuits," *IEEE Transactions on Nuclear Science*, vol. 51, pp. 2328-2336, 2004.

[68] Y.D. Chen, "Low Noise, High Sensitivity Active Pixel Sensors," PhD Dissertation, in *EECS*. Irvine: UC Irvine, 2004.

[69] B. Razavi, *Principles of Data Conversion System Design*: IEEE Press, 1995.